Identification of the VHE Gamma-ray Source HESS J1303-631 as a Pulsar Wind Nebula Through Multi-Wavelength Observations

DISSERTATION

zur Erlangung des akademischen Grades
doctor rerum naturalium (Dr. rer. nat.)
im Fach Physik

eingereicht an der
Mathematisch-Naturwissenschaflichen Fakultät I
Humboldt-Universität zu Berlin

von
Herrn Matthew Lynn Dalton M.S.
geboren am 29.07.1980 in Brigham City, Utah, USA

Präsident der Humboldt-Universität zu Berlin:
Prof. Dr. Jan-Hendrik Olbertz

Dekan der Mathematisch-Naturwissenschaflichen Fakultät I:
Prof. Dr. Andreas Herrmann

Gutachter:
1. Prof. Dr. rer. nat. habil. Thomas Lohse
2. Prof. Dr. rer. nat. habil. Götz Heinzelmann
3. Prof. Dr. rer. nat. habil. Alexander Kappes

eingereicht am: 14. Februar 2011
Tag der mündlichen Prüfung: 28. März 2011

Abstract

This work represents the identification of the very high energy, $E_\gamma > 100$ GeV (VHE), Gamma-ray source HESS J1303−631 as a pulsar wind nebula (PWN) powered by the pulsar PSR J1301−6305. This is achieved through the detection of energy dependent morphology in the High Energy Stereoscopic System (H.E.S.S.) data, the detection of a new X-ray PWN in archival *XMM-Newton* X-ray observations, as well as multi-wavelength modeling of the source and its energetics. An upper limit on the radio synchrotron flux is obtained from observations made by the Parkes telescope at 4.48 GHz. The combined Gamma-ray, X-ray and radio measurements are used to constrain a leptonic emission model, where strong winds of relativistic electrons and positrons from the pulsar power the acceleration of particles to ultrarelativistic energies at the wind termination shock region, and these shock accelerated leptons then form a nebula which emits in the X-ray and radio bands via synchrotron emission in the ambient magnetic field and Gamma-rays through the inverse Compton mechanism.

One surprising result of this analysis is the anomalously low magnetic field derived for the PWN. Typical values for PWNe are on the order of $10\,\mu$G. For this source, however, the low synchrotron levels predict an average magnetic field of $\sim 0.9\,\mu$G. The low magnetic field is explained in the scenario of an expanded/evolved PWN as predicted by de Jager et al. [2009].

The distance to the pulsar, PSR J1301−6305, is estimated to be ~ 6.6 kpc based on the dispersion measure of the pulsar radio emission. The dispersion measure is, however, notorious for providing unreliable distance estimates. Based on an earlier model of the electron distribution in the Galaxy, the dispersion measure gave a distance to the pulsar of 16 kpc. An alternative estimation of the distance to the source is provided by the presence of a star formation region, IRAS 13010−6254, located in projection on the edge of the TeV emission region opposite the pulsar, but within the 14 σ significance contours of the TeV emission. The direction of the star formation region is indicated by the X-ray PWN trail, which appears to point back in the direction of IRAS 13010−6254. This is the only star formation region known in the vicinity of the TeV source and, in the absence of a detected supernova remnant, provides a compelling and only yet known candidate for the birth place of the pulsar, since star formation regions are known to produce massive stars and supernovae at a high rate. Based on the kinematic velocity of the star formation region, the distance estimate 12.6 kpc is obtained. This distance is also corroborated by other arguments, such as the column density obtained from the X-ray spectral fit and the size of the emission regions.

Zusammenfassung

Diese Arbeit beschreibt die Identifikation der bisher unidentifizierten TeV Gammastrahlungsquelle, HESS J1303−631 als Pulsarwind-Nebel, angetrieben von dem Pulsar PSR J1301−6305. Dieses Ergebnis wird durch den Nachweis von energieabhängiger Morphologie in den vom High Energy Stereoscopic System (H.E.S.S.) genommenen Daten und durch die Detektion eines neuen Röntgen-Pulsarwind-Nebels in XMM-Newton Daten erreicht. Zudem wird eine obere Schranke auf den Fluss von Radiostrahlung aus Beobachtungen mit dem Parkes Radioteleskop bei 4.48 GHz abgeleitet. Diese Ergebnisse können in einem leptonischen Modell des Pulsarwind-Nebels verstanden werden, wo Elektronen und Positronen in der Nähe des Termination Shocks des Pulsarwindes auf ultrarelativistische Energien beschleunigt werden. Diese Leptonen bilden einen ausgedehnten Pulsarwind-Nebel, der auf Grund des inversen Compton-Effekts und Synchrotronstrahlung TeV Gammastrahlung beziehungsweise Röntgen- und Radiostrahlung erzeugt.

Da nur eine obere Grenze auf den Radiofluss abgeleitet wurde, erfolgte die Modellierung im Rahmen eines einfachen “one zone models”, wo angenommen wird, dass die Radio-, Röntgen- und Gammastrahlung alle von derselben Leptonenpopulation erzeugt werden. Das Modell wird aber trotzdem von den Daten schon eingeschränkt und liefert ein schwaches Magnetfeld von $\sim 0.9\,\mu$G. Diese Magnetfeldstärke ist überraschend niedrig, da in ähnlichen Systemen die Magnetfeldstärken eher bei $10\,\mu$G liegen. Andererseits passt das Ergebnis gut zu dem sehr niedrigen Synchrotronstrahlungsfluss. Ein derart schwaches Magnetfeld wird im theoretischen Szenario eines ausgedehnten, beziehungsweise entwickelten Pulsarwind-Nebels erklärt de Jager et al. [2009].

Die Entfernung des Pulsars, PSR J1301−6305, wurde aus Radio-Dispersionsmessungen zu ~ 6.6 kpc abgeschätzt. Die Anwendung dieser Methode zur Abschätzung der Entfernung basiert auf Modellen der Elektronenverteilung in der Milchstraße und es ist bekannt, das einzelne Entfernungen mit großen systematischen Unsicherheiten behaftet sein können. Mit einem etwas älteren Modell der Elektronenverteilung wurde zum Beispiel eine Entfernung von 16 kpc abgeschätzt. Die Sternentstehungsregion IRAS 13010−6254 ermöglicht eine alternative Methode zur Entfernungsbestimmung. Diese Sternentstehungsregion befindet sich in Projektion auf der dem Pulsar gegenüberliegenden Seite der TeV Emissionsregion aber immerhin innerhalb der 14 σ Signifikanzkontur der TeV Emission. Die Morphologie des Röntgen-Pulsarwind-Nebels verweist auf die Sternentstehungsregion. IRAS 13010−6254 ist die einzige bekannte Sternentstehungsregion innerhalb von $\sim 2°$ um die TeV Quelle und stellt, da kein dem Pulsar zuzuordnender Supernovareste bekannt ist, den bisher einzigen plausiblen bekannten Kandidat für den Geburtsort des Pulsars dar. Sternentstehungsregionen sind dafür bekannt, schwere Sterne und daher auch Supernova-Explosionen mit einem Pulsar als Überrest bei einer sehr hohen Rate zu erzeugen.

Auf Grund der kinematischen Geschwindigkeit der Sternentstehungsregion erhält man eine Entfernung von 12.6 kpc. Eine so große Entfernung wird auch von anderen Messungen nahe gelegt zum Beispiel der hohen aus Röntgenspektren abgeleiteten Massenbelegung und der Größe und Morphologie der Emissionsregionen.

Contents

Nomenclature

FOV	field of view
GDR	giant dipole resonance
GRB	Gamma-ray burst
H.E.S.S.	The High Energy Stereoscopic System
IACT	imaging atmospheric Cherenkov telescope
MC	Monte Carlo
NSB	night sky background
PMT	photo-multiplier tube
PSF	point spread function
PSR	pulsar
PWN	pulsar wind nebula
SED	spectral energy distribution
SNR	supernova remnant
VHE	very high energy ($E > 100$ GeV)

1 Introduction

The field of VHE Gamma-ray astronomy has opened up a new window on the Universe. Since Gamma-rays are the highest energy photons in the electromagnetic spectrum, this represents a window on the highest energy phenomena in the Universe, sometimes referred to as the *violent Universe*. The detection of objects such as Active Galactic Nuclei (AGNi), compact regions at the center of some galaxies with very high luminosities and thought to be powered by supermassive black holes, Supernova Remnants (SNRs), massive outflows of plasma after a stellar explosion, and Pulsars, the fast rotating, strongly magnetized neutron stars left over from the core of the Supernova event, has greatly augmented our understanding of some of Nature's most "violent" processes. Moreover, Gamma-ray astronomy has provided essential tests and constraints of fundamental physics which could hardly be obtained otherwise, such as tests of quantum gravity based on energy dependent arrival times of Gamma-rays from AGNi traveling cosmological distances, and the search for dark matter.

As is the case in every new field of study, many unexpected discoveries should be expected, such as the so called "dark sources" [Tibolla et al., 2009], VHE Gamma-ray sources without known counterparts in radio or X-ray. The first of these sources discovered by H.E.S.S. is HESS J1303−631. This source of VHE Gamma-rays was serendipitously discovered during an observation campaign for the pulsar binary system, PSR B1259−63, in 2004. Lying just to the north of the binary system, this mysterious source seemed to have no counterparts in X-ray or radio, and its origin remained a mystery.

H.E.S.S. has shown itself well suited for chance discoveries, due to it large field of view, enabling large scale surveys of the sky, and high sensitivity. The number of unidentified sources now discovered by H.E.S.S. is > 20, so that these sources now tenably represent the largest unsolved mystery of VHE astronomy.

1.1 Very High Energy Gamma-ray Astronomy

Gamma-rays have long been predicted to trace the origins of cosmic-rays. Hadronic cosmic-rays near sources may collide with other "target" particles, either from the interstellar medium or nearby molecular clouds, and thereby produce secondary pions which further decay into Gamma-rays. Cosmic-ray electrons can also produce Gamma-rays through inverse Compton scattering, depositing their energy into the scattered "target" photon which may come from the Cosmic Microwave Background, thermal infrared light from molecular clouds or even starlight. The Gamma-rays produced by these cosmic-rays have several scientific advantages over their parents, the main advantage being that they are not charged and can therefore travel through the chaotic Galactic magnetic fields undeflected and thus without obscuring their direction of origin. Thus, intense local sources of cosmic-rays, given certain conditions (e.g. sufficient cosmic-ray energy/flux, appropriate targets for Gamma-production) should be detectable by Gamma-ray experiments. Furthermore, the detected Gamma-rays, in combination with other multi-wavelength information, can be used to extract information about the parent cosmic-rays near the source, such as their energy spectrum and composition.

1.1.1 Development of the Field

Since Gamma-rays' large energy is absorbed in the Earth's atmosphere, the first searches for extraterrestrial Gamma-rays were carried out by spaceborne telescopes aboard satellites. These experiments were originally sensitive to Gamma-rays in the range of $\sim$MeV, but more modern satellite observatories have increased the range up to $>$GeV energies. The first successful detection of cosmic Gamma-rays was achieved in 1961 by satellite Explorer XI, which detected 22 Gamma-ray events. This was followed by many more satellites, including the Vela satellite, which detected the first Gamma-ray Burst (GRB), the most energetic events known in the Universe consisting of a very short ($\sim$ 1 sec) intense flash of Gamma-rays.

But the detection of these sources at higher energies proved to be more difficult because of the extremely low fluxes of these sources. The Crab pulsar, for example, one of the most powerful stable Gamma-ray emitters in the sky, has a flux $\sim 10^{-11}$ cm^{-2} s^{-1} above 1 TeV, so that even a one hundred square meter detector can only expect to see less than one photon per day, not to mention the difficulty and expense of building and launching into space a 100 m^2 telescope. And so it was clear, in order to extend investigation up to the highest energies now detected, the TeV band, one would needed a new detection method.

Fortunately, a method was found to turn Gamma-rays' weak point - their absorption in the Earth's atmosphere - into their strong point: the absorbed energy of the primary Gamma-ray is converted into a shower of high energy particles, mostly electron and positron pairs, which emit a portion of their energy in the form of a flash of light lasting on the order of ten nanoseconds. By building arrays of telescopes with fast electronics which observe large portions of the atmosphere, these flashes of light can be used to, indirectly, detect the primary Gamma-rays initiating the showers. In this way, the Earth's atmosphere itself is used as a giant calorimeter, enabling large areas to be used for detection.

The most common type of experiment for detecting Gamma-ray showers are the Imaging Atmospheric Cherenkov Telescopes, which focus Cherenkov light produced by the relativistic charged particles from the shower as they pass through the atmosphere onto an imaging camera. When more than one such telescope is used in coordination, the various stereoscopic images can be used to very accurately reconstruct the shower parameters in three dimensions. The IACT technique was pioneered by the Whipple collaboration and led to the discovery of TeV emission from the Crab Nebula in 1989. The Whipple 10 m telescope also discovered the first extra-galactic source of TeV emission with the detection of very high energy Gamma-ray emission from the AGN Markarian 421. The HEGRA telescope array was the first system to use multiple telescopes in stereoscopic mode.

The last decade has seen a stark growth in the field of ground based Cherenkov telescopes. The current generation of detectors includes VERITAS in Arizona, Major Atmospheric Gamma-ray Imaging Cherenkov (MAGIC) in the Canary Islands, CANGAROO in Australia and The High Energy Stereoscopic System (H.E.S.S.) in Namibia. The four H.E.S.S. telescopes have been in full operation since 2003 and are sensitive to Gamma-rays in the range of $\sim$ 100 GeV to 100 TeV, however, since 2007, the H.E.S.S. collaboration has been planning and begun construction of a fifth telescope with a 27 m dish in Namibia which will significantly lower the energy threshold to the range of tens of GeV. The addition is intended to close the gap in spectral coverage between ground based and space based Gamma-ray observatories.

1.1.2 Cosmic Sources of VHE Gamma-rays

The field of Gamma-ray astronomy has progressed at an exceptional rate in the last decade. Since the commissioning of the first H.E.S.S. telescopes in 2003, and the first MAGIC telescope in 2004 [Baixeras et al., 2004] and the commissioning of the VERITAS telescope array in 2006 [Celik, 2007], hundreds of new discoveries and publications have resulted. In this section, some recent results of the main research topics are reviewed.

The types of astrophysical sources which have now been detected in TeV energies is broad and varied. Most of the sources belong to one of the following classes:

I Pulsars and pulsar wind nebulae
II Pulsar binary systems
III Supernova remnants
IV Active Galactic nuclei
V Starburst galaxies

A large number of these sources are of Galactic origin and are concentrated near the center of the Galaxy (see Figure 1.1).

Pulsar Wind Nebulae in TeV Energies

The Crab pulsar wind nebula was the first source detected in VHE Gamma-rays by the Whipple collaboration [Weekes et al., 1989]. Born in a historical supernova observed in 1054 AD, it is the only pulsar with an accurately known age. At a distance of only 2 kpc, and a very high rate of energy loss ($\dot{E} = 4.6 \times 10^{38}$ erg s^{-1}, see Chapter 3), it is

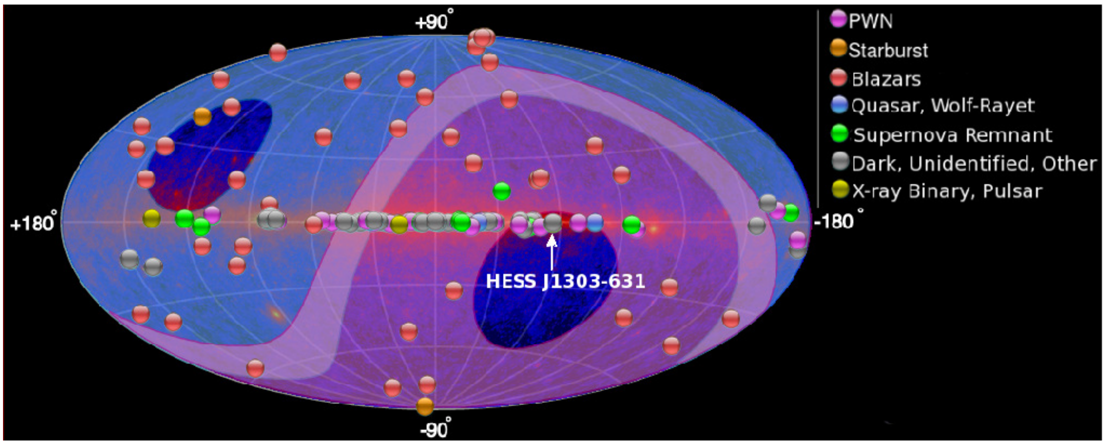

Figure 1.1: Whole-sky map of known TeV Gamma-ray sources. Taken from TeVCat: `http://tevcat.uchicago.edu/`. The center of the plot corresponds to the center of the Milky Way and the horizontal line passing through it is the Galactic plane, where most of the TeV sources are found. The violet region indicates the portion of the sky best visible to the H.E.S.S. experiment (the "southern sky") while the turquoise region shows the portion best visible to norther hemisphere experiments, such as VERITAS and MAGIC (the "northern sky"). The location of HESS J1303−631 is shown with a white arrow.

one of the brightest sources of TeV Gamma-rays in the sky and, due to its stability, it is a very convenient standard candle in TeV astronomy [Meyer et al., 2010] so that the fluxes of other detected sources are often cited in units of the Crab flux (integral flux above 1 TeV $\sim 2.26 \times 10^{-11}\,\mathrm{cm}^{-2}\,\mathrm{s}^{-1}$ [Aharonian et al., 2006a]) and is used for cross-calibration of various experiments. This is despite the fact that the X-ray synchrotron emission from the Crab nebula has recently been found to change at a rate of $\sim 3.5\%$ yr^{-1} [Wilson-Hodge et al., 2010] or a total of about 7% in recent years (see Figure 1.2). The variation was observed at various energies in X-rays from 10 - 100 keV and there is some evidence of spectral variation as well, however, it is still believed that the object can be used as a standard candle when regular observations are used to correct for these variations.

The Crab nebula is detected in TeV Gamma-rays only as a point source, but has been studied extensively in virtually every energy band of the electromagnetic spectrum and is perhaps the best understood of all sources of TeV Gamma-rays (see e.g. Horns and Aharonian [2004], Kennel and Coroniti [1984]. As will be described in Chapter 3, the broad band emission is believed to come from high energy leptons ($e^{+/-}$, often referred to as simply "electrons") accelerated to high energies by the pulsar. These electrons emit in the radio to X-ray band through synchrotron interactions with the ambient magnetic field, and in the VHE Gamma-ray band through the process of inverse Compton up-scattering of ambient photons. The broad band spectral energy distribution of the Crab

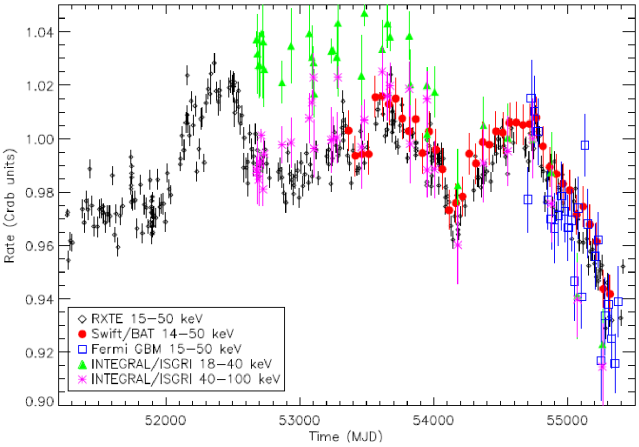

Figure 1.2: Composite Crab light curve for RXTE/PCA (15-50 keV - black diamonds), Swift/BAT (14-50 keV - red filled circles), Fermi/GBM (15-50 keV - open blue squares), INTEGRAL/ISGRI (18-40 and 40-100 keV - green triangles and purple asterisks, respectively.) Each data set has been normalized to its mean rate in the time interval MJD 54690-54790. All error bars include only statistical errors. The flux of the "standard candle" in Gamma-ray astronomy is found to vary in the X-ray synchrotron band at a level of $\sim 3.5\%\ \mathrm{yr}^{-1}$.

nebula (Figure 1.3 bottom), is very well charted and has proven crucial for inferring electron populations in order to test theories for the acceleration processes at work in such environments.

The VHE Gamma-ray source HESS J1825−137 is an elegant example of an extended PWN. This was the first TeV source shown to exhibit an energy dependent morphology [Aharonian et al., 2006f], clearly demonstrating the association of the source with the pulsar PSR B1823−13. In Figure 1.4, the low energy (0.2-0.8 TeV) Gamma-ray extension is shown in red, middle energies (0.8-2.5 TeV) in green and the highest energies (> 2.5 TeV) in blue. The low energy photons are found to have a larger extension than that of the higher energies. This can be understood as the "cooling" (through various radiation processes and adiabatic losses, see Chapter 4) of the electrons responsible for the emission as they slowly diffuse away from the source. The cooling of these electrons results in a spectral steepening of the TeV emission which will manifest itself as an energy dependent morphology.

Supernovae and Supernova Remnants

Supernovae (SNe), originating in thermonuclear explosions or gravitational core collapse of massive stars, release a large amount of energy, on the order of 10^{51} erg. In the case of a thermonuclear explosion, type Ia supernovae, a majority of this energy release, $\sim 99\%$, is carried away invisibly by neutrinos, however, an amount on the order of 10^{49}

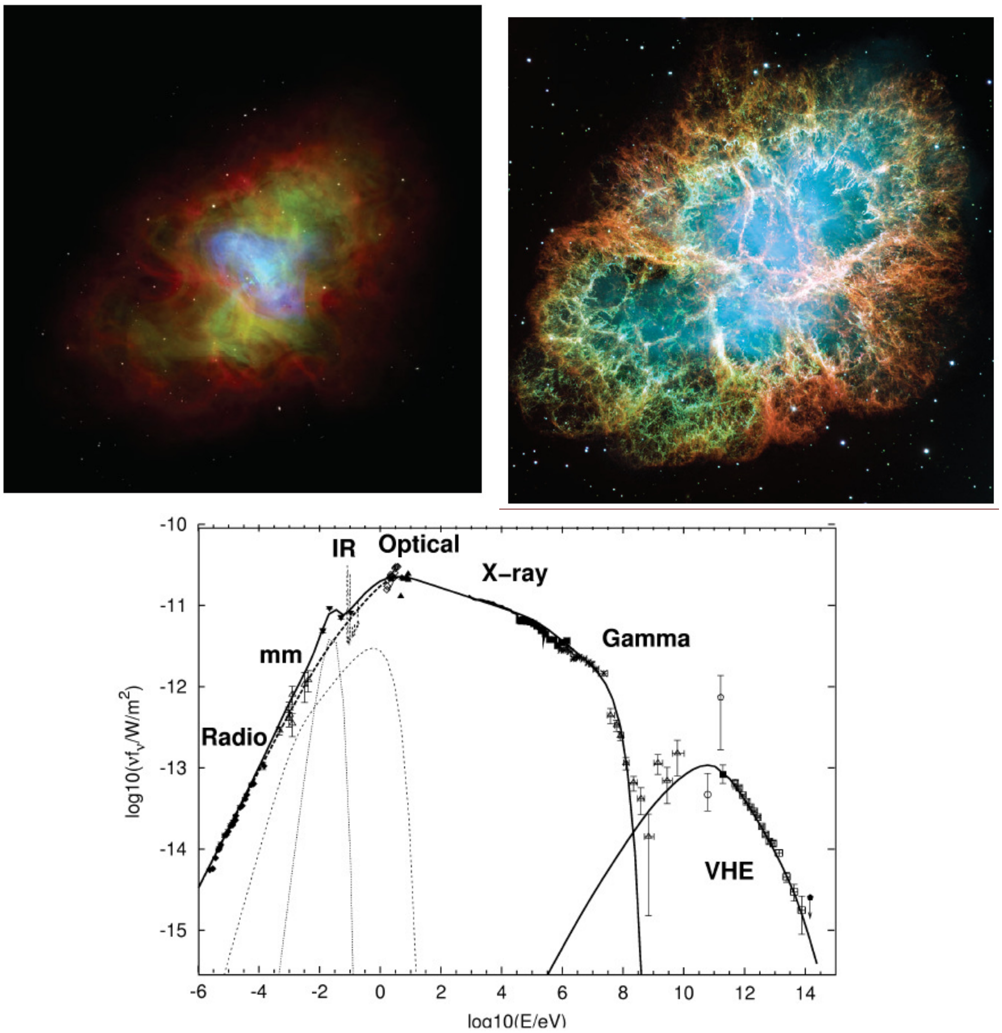

Figure 1.3: Top Left: Color mosaic of the Crab synchrotron nebula showing a *Chandra* X-ray image in blue, visible light from HST in green, and VLA radio image in red. The pulsar is seen as the bright blue point source at the center of the image.
Top Right: A composite Hubble Space Telescope image of the Crab Nebula. Thermal filaments composed of ejecta from the supernova explosion appear around the outer part of the nebula. Both figures taken from [Hester, 2008].
Bottom: the global spectral energy distribution of emission from the Crab nebula, taken from Horns and Aharonian [2004].

erg is carried away as kinetic energy in the stellar ejecta. In the case of gravitational collapse, electron degeneracy pressure prevents the core from collapsing completely to form a black hole and the released gravitational potential energy is directed outwards in

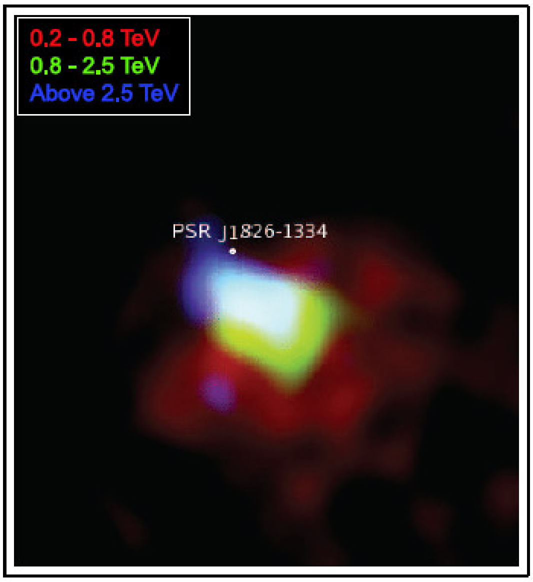

Figure 1.4: Mosaic image of the Gamma-ray emission of HESS J1825−137 in different energy bands (red: 0.2-0.8 TeV, green 0.8-2.5 TeV and blue: above 2.5 TeV). The different gamma-ray energy bands show a shrinking with increasing energy away from the pulsar PSR B1823−13. Figure taken from The H. E. S. S Collaboration: S. Funk et al. [2007]

the form of a shock, ejecting the outer layers of the star.

The ejecta from supernovae, when colliding with material from the interstellar medium, is believed to form a shock region which can accelerate particles to VHE energies. Interest in the VHE Gamma-ray emission from supernova remnants (SNRs) has arisen due to their association as prime candidates as at least one of the sources of Galactic cosmic-ray acceleration.

The source SN 1006 is the remnant of one of the few recorded historical supernovae. It appeared in the southern sky on May 1st, 1006, and was recorded by Chinese and Arab astronomers [Stephenson and Green, 2002]. SN 1006 is one of the best-observed SNRs with a rich data set of astronomical multi-wavelength information in radio, optical and X-rays, and all the important parameters, such as the ejected mass, its distance and age are fairly well-known [Cassam-Chenaï et al., 2008].

Although initial observations by H.E.S.S. of SN 1006 resulted in only an upper limit [Aharonian et al., 2005a], models based on multi-wavelength observations predicted a TeV flux at a factor of ~ 5 below the H.E.S.S. upper limit [Ksenofontov et al., 2005] prompting extended observations which eventually resulted in a H.E.S.S. detection of the source in TeV energies [Acero et al., 2010].

The TeV excess for SN 1006 was found in two locations: the North-East and South-West edges of the remnant (Figure 1.5, top right), similar to the morphology found in X-rays and radio (Figure 1.5, top left). This is believed to be due to the local Galactic magnetic field, which is oriented along that direction. If the Gamma-rays are produced by electrons inverse scattering on ambient photon fields, then this may be interpreted as being due to the hinderance of electron acceleration processes in the direction perpendicular to the magnetic field by synchrotron damping. The broad band spectral energy distribution, including radio spectra obtained from Reynolds [1996] and X-ray spectrum obtained from Bamba et al. [2008], is shown in Figure 1.5, bottom.

The emission was modelled assuming the shell creates a shock region which accelerates either electrons, hadrons or both to ultra-relativistic energies which then produce X-ray and radio emission from synchrotron emission and Gamma-rays from inverse Compton scattering, in the case of electrons, and proton-proton interactions producing π^0's which decay producing Gamma-rays, in the case of hadronic origin (see e.g. Rybicki and Lightman [1979]). While the flux at TeV Gamma-rays can be well described by a purely leptonic model, this does not accurately reproduce the observed spectrum. On the other hand, the assumption of a purely hadronic origin to the TeV flux would require a very high efficiency of 20% in conversion of the supernova explosion energy, $E_{\mathrm{SN}} = 1.4 \times 10^{51}$ erg, to high energy protons, and, considering the polar morphology of the TeV emission, much higher local efficiencies. A combined leptonic and hadronic scenario, as shown in Figure 1.5, also led to a satisfactory description of the multi-wavelength data and none of these models is excluded.

Star Burst Galaxies and Dwarf Galaxies and the Galactic Center

Since cold dark matter is expected to accumulate in the centers of most galaxies, this presents a compelling opportunity for Gamma-ray observatories. Many dark matter particle candidates are expected to self annihilate [Ellis et al., 2002, Profumo and Ullio, 2004] which, in regions of high density, may result in a VHE signal detectable by IACT systems.

Nearby dwarf galaxies neighboring the Milky Way provide an opportunity to detect or place limits on a dark matter annihilation signal. High concentrations of dark matte particles and their proximity to the Earth compared to other extragalactic sources would suggest a high sensitivity. Also, since many dwarf galaxies lie away from the Galactic plane, confusion with other sources is less likely and the lack of Galactic diffuse emission simplifies the analysis. Although to date, no dark matter annihilation searches have resulted in a detection, H.E.S.S. observations of VHE Gamma-ray observations of Dwarf galaxies have placed some upper limits on the annihilation related fluxes [HESS Collaboration et al., 2010].

The center of the Milky Way may theoretically be one of the most ideal places to search for dark matter annihilation signals, due to its relative proximity compared to other galaxies and the high concentrations of dark matter expected within the Milky Way. It is, however, practically complicated by the presence of diffuse emission and the Galactic center source, HESS J1745−290. It has, however, been shown that this point source

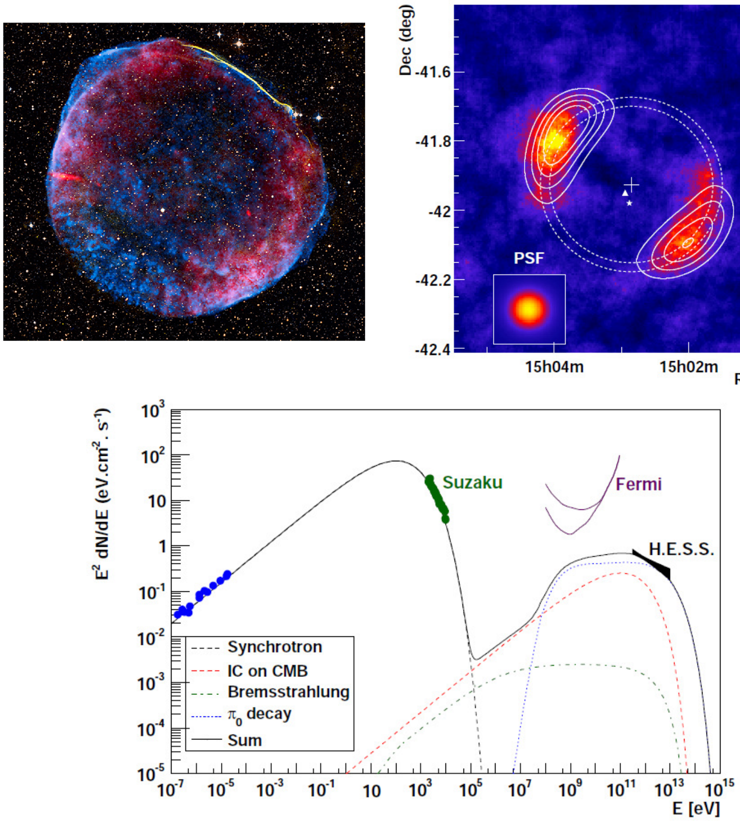

Figure 1.5: SN 1006: Top Left: composite X-ray (blue) and radio (red) image. The radio synchrotron emission is oriented along the Galactic magnetic field lines, from NE to SW, APOD (2008) `http://antwrp.gsfc.nasa.gov/apod/ap080704.html` Image Credit: NASA, ESA, Zolt Levay (STScI). Top Right: H.E.S.S. TeV excess, also found to be oriented along the Galactic magnetic field lines. Bottom: broad band SED of SN 1006, modeled with a combination of leptonic and hadronic components. The last two figures are taken fron Acero et al. [2010].

itself, cannot be well described by dark matter annihilations and the bulk of the emission must be of a non-dark matter nature [Aharonian et al., 2006b]. Advanced data taking techniques, such as the “drift scan” or “On-Off” observation modes (described in Chapter 2) are currently being pursued to overcome some of the difficulties of observing the Galactic center. It has been shown, for example, by Birsin [2011] that 6 hours of observation of the Galactic center in On-Off mode can provide more stringent upper limits on dark matter annihilation signals than 10 hours of observations of dwarf Galaxies.

A Gamma-ray signal has, however, been detected by H.E.S.S. in the starburst galaxy NGC 253 [Acero et al., 2009]. But this signal has been linked to cosmic-rays, where the density of these cosmic-rays, determined by the Gamma-ray observations, has been found to be 3 orders of magnitude larger than in our own Galaxy, mainly due to an increased rate of star formation and, therefore, increased supernova rate.

Active Galactic Nuclei

Although active galactic nuclei (AGNi) vary widely in their emission characteristics, they are now believed to consist of a supermassive black hole ($10^7 - 10^{10}$ solar masses) at the center of some galaxies accompanied by an accretion disk which, in some cases, may also power jet-like outflows in the direction perpendicular to the accretion disk [Urry and Padovani, 1995]. These highly relativistic collimated outflows are known to produce non-thermal emission from radio to Gamma-rays. However, there are still many details of ANG models which are not clear, for example whether the VHE emission is hadronic or leptonic in origin and where precisely the particles are accelerated.

Observations of AGNi are complicated by the fact that AGNi are highly variable, switching between a “high” or “low” state which may differ by orders of magnitude in a period of days to years, meaning that simultaneous observations at various wavelengths are required in order to be able to compare the observations. Furthermore, VHE Gamma-rays suffer extreme losses when traveling the cosmological distances from high redshift galaxies due to interactions with the extra-galactic background light (EBL) resulting in a high energy cut-off in the spectrum and severely reducing visibility in the TeV regime [Heitler, 1954].

However, as noted by Stecker et al. [1992], this hinderance can be taken advantage of: by measuring the cut-off energy of the TeV spectrum from AGNi one can estimate the level of the EBL. They predicted a cut-off in the range of 0.1 to 1 TeV. Precisely this method was employed by Aharonian et al. [2007] using H.E.S.S. observations of 1ES 0229+200 (at red shift $z = 0.14$) which resulted in a surprisingly hard spectrum of $\Gamma = 2.50 \pm 0.19$ with the spectrum extending out to $E \gtrsim 10$ TeV with no evidence detected for a cut-off or spectral break. These results were used to constrain the EBL, which are dependent upon the assumed intrinsic spectral index, but, in general, close to the lower limit placed by galaxy counts.

Additionally, observations of TeV emission from AGNi have allowed tests of fundamental physics. Some theories of quantum gravity, for example, predict Lorentz invariance violating, energy dependent photon dispersion relations near the Plank scale. Observations of fast TeV Gamma-ray flares from the Blazar PKS 2155-304 (at redshift $z = 0.116$) with H.E.S.S. have allowed constraints on the emergence of quantum gravity induced breakdown of Lorentz invariance to an energy scale of several 10^{17} GeV, a few percent of the Planck mass, $\mathrm{M}_{\mathrm{Planck}}$ [Wagner et al., 2008].

1.2 The Imaging Atmospheric Cherenkov Technique

Already in the early 1960’s it was well known that cosmic-ray air showers with primary energies above $\sim 10^{15}$ eV should produce a flash of Cherenkov light and that this light would be detectable above the night sky background by ground detectors using simple photo-muliplier tubes (PMTs) [Hill, 1961].

1.2.1 Cosmic Ray Air Showers

As discovered by Pierre Auger, when a cosmic ray, whether Gamma-ray, leptonic or hadronic, strikes the Earth's atmosphere it interacts with it and produces a large cascade of high energy daughter particles. Some of the energy of the shower is radiated in the form of Cherenkov light, fluorescence light or particle fluxes which can all be observed by detectors on Earth. In this way, the Earth's atmosphere itself is incorporated into the detection system. These showers are crucial to the detection of high energy cosmic-rays, regardless of type, and without this atmospheric detector we would know virtually nothing about the highest energy cosmic rays. However, in order to extract any useful information out of these showers it is important to have a good understanding of this gaseous detector.

As particles travel through the atmosphere they have a certain probability of interacting within a given distance. This probability depends on the cross section of interaction of the particles (which in turn depends on the particle types and their center of mass energy) and on the density of the gas (or other medium) that is being traversed. As a measure of the amount of material through which a particle has passed we define the slant depth, X, (similar to the concept of optical depth in optics), in units of $\mathrm{g/cm}^2$, as the mass in a centimeter square column of air along the path of the particle. Many experiments report their height as a minimum slant depth required for a particle to reach their detector (the slant depth at sea level for a vertical shower, for example, is about $1030\ \mathrm{g/cm}^2$). Obviously a shower coming at a steep angle will traverse more atmosphere and thus be at a higher slant depth when it reaches the detector and be more "aged" or attenuated than a vertical shower.

The cosmic ray shower begins with one very high energy particle, the *primary particle*. Through successive interactions with nuclei in the atmosphere, the number of particles in the shower, $N(X)$, grows until the average energy of the particles falls to the point that they are no longer able to produce new particles. At this point the number of particles has reached a maximum, N_{max}. The particles continue to loose energy through interactions with the atmosphere and the number of particles in the shower then begins to decline. The atmospheric depth, or slant depth, where the shower reaches maximum size is referred to as X_{max}.

1.2.2 A Simple Electromagnetic Cosmic Ray Shower Model

Many useful and interesting features of cosmic ray air showers can be derived from a simple model originating from W. Heitler [Heitler, 1954, Gaisser, 1991]. This model is constructed as such: assume that the particles in a gamma ray induced cosmic ray shower interact after a fixed distance λ. In that interaction they each produce two particles and give each particle half of their energy. This process continues, doubling the number of particles at each step until the particles fall below the critical energy, E_c for particle production at which point they begin to loose energy by other means until all energy is dissipated or the shower strikes the ground (Figure 1.6).

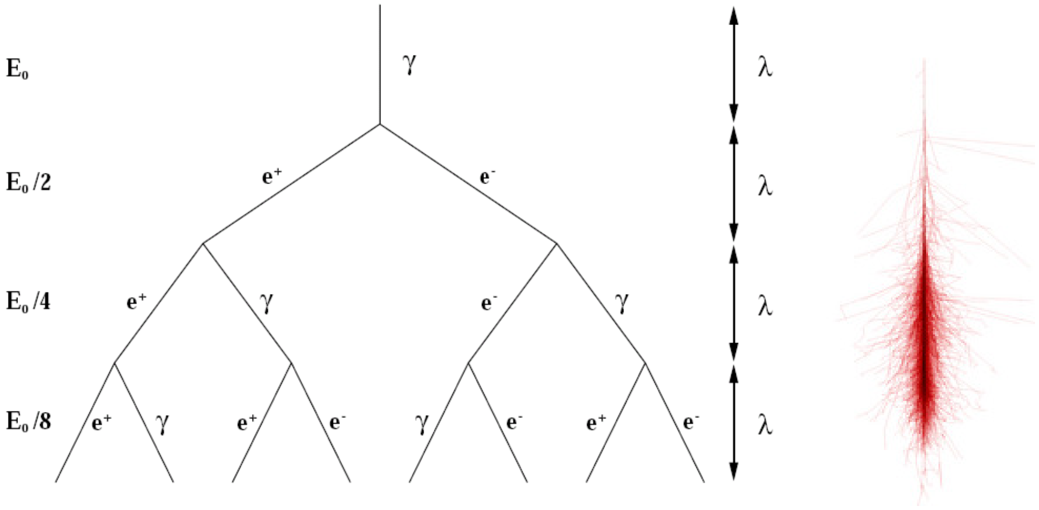

Figure 1.6: Left: a simple model of an electro-magnetic air shower. A γ with initial energy E_0 decays through pair production after a fixed interaction length λ. The e^+ and e^- created this way then each produce photons through bremsstrahlung from interaction with the air after another interaction length. Right: Monte Carlo simulated shower using CORSIKA for a 100 GeV photon [Schmidt, 2005].

If X is the depth traversed then the number of interactions is $n = X/\lambda$ and the number of particles in the shower at this stage is

$$N(X) = 2^{X/\lambda} \tag{1.1}$$

and since the energy is evenly distributed each constituent particle in the shower would have an energy of

$$E(X) = \frac{E_0}{2^{X/\lambda}} \tag{1.2}$$

at the slant depth X. The number of particles in the shower will thus grow until the average particle energy falls below E_c so that the maximum will be

$$N_{max} = \frac{E_0}{E_c} \tag{1.3}$$

Then combining equations (1.2) and (1.3) we find the location of shower maximum:

$$X_{max} = \lambda \frac{\ln(E_0/E_c)}{\ln 2} \tag{1.4}$$

From this simple model we can find two very important aspects of air showers. First that the number of particles at shower maximum is proportional to the primary energy,

$$N_{max} \propto E_0 \tag{1.5}$$

and the atmospheric depth of shower maximum is proportional to the logarithm of the energy of the primary particle,

$$X_{max} \propto \ln E_0 \tag{1.6}$$

These results hold exactly for electromagnetic cascades and approximately for hadronic ones (Gaisser [1991]). The value of X_{max} is dependent on the type of particle, and therefore of great interest for cosmic ray composition studies. But because of statistical fluctuations in shower development and the location of X_{max} it is, unfortunately, not possible to tell the composition of the primary of an individual shower. However by comparing with slant depths from simulations one can find the average composition and see compositional changes.

Hadronic showers, initiated by single protons or heavier nuclei are slightly different, producing muons and pions and other particles. These showers are much more complicated and not as well understood, primarily because of a lack of understanding of the hadronic interactions at these energies. Fortunately, the total light yield is still roughly proportional to the number of particles calculated for an electromagnetic shower in the preceding equations.

1.2.3 Cherenkov Radiation

Cherenkov radiation [Landau, 1984] is a form of radiation produced by charged particles when they travel through a dielectric medium with a speed greater than that at which light would otherwise propagate in the same medium. As the charged particle travels through the medium, it disrupts the local electromagnetic field. Electrons in the atoms of the medium will be displaced, and the atoms become polarized by the passing electromagnetic field of the charged particle. Photons are emitted as dielectric's electrons restore themselves to equilibrium after the charged particle has passed.

If v_p is the particle's velocity and v_{em} is the velocity of light in the material and we define $\beta = v_p/c$, then the distance traveled by the particle in time t is

$$x_p = \beta c t \tag{1.7}$$

and the distance traveled by the emitted photons is

$$x_{em} = \frac{c}{n}t \tag{1.8}$$

where n is the refractive index of the material (see Figure 1.7). Then the angle at which the electromagnetic wavefront is emitted is

$$\cos\theta = \frac{1}{n\beta} = \frac{c}{nv_p} = \frac{v_{em}}{v_p} \tag{1.9}$$

Note that if $v_p < v_{em}$ then $\cos\theta > 1$ which is non-physical. This is because if the velocity of the particle is less than the velocity of light in the material then the photons interfere destructively and no radiation is emitted.

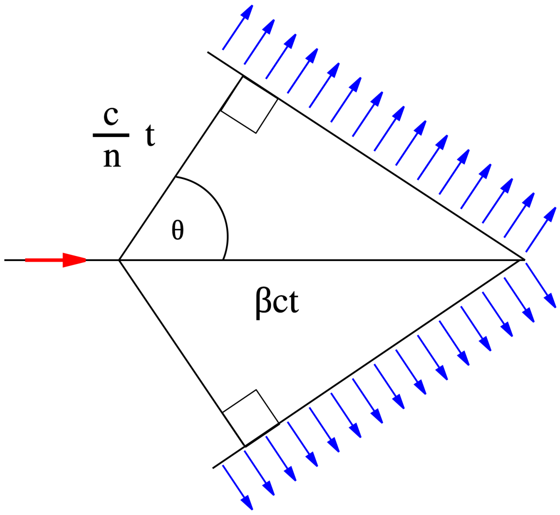

Figure 1.7: Cherenkov radiation: a relativistic charged particle traveling with velocity βc in a medium with refractive index n will emit Cherenkov radiation at an angle of θ as given in the text. Figure taken from Horvath [2006].

Since cosmic-ray air showers consist of large numbers of charged particles with relativistic speeds, the Cherenkov radiation emitted by these particles is an ideal candidate for imaging and studying these showers.

1.2.4 Other Types of Gamma-ray Experiments

It may be worth noting that imaging Atmoshperic Cherenkov telescopes were not the only method of Gamma detection tried in the early days of VHE Gamma-ray astronomy. For example, the CELESTE experiment (Figure 1.8) converted an abandoned solar power farm into a Cherenkov wavefront sampler to be used for Gamma-ray astronomy [CELESTE Collaboration, 2005]. This type of experiment has the advantage of enormous light collection area, reducing the Gamma-ray detection threshold to less than 100 GeV, but the method suffers at energies $\gtrsim$ 1 TeV. It is, however, possible with imaging telescopes to reduce the energy threshold to $\sim$ 100 GeV by using somewhat larger telescopes, and this method has now become the dominant style.

On the other hand, the main competitor to the imaging technique is a method pioneered by the Milagro experiment [Atkins et al., 2004], using water Cherenkov detectors on the ground which measure the charged particles from the shower instead of imaging them high in the atmosphere. Because the charged particles must have enough energy to reach ground level and still have enough energy to emit significant Cherenkov radiation in the water tanks, this method has very limited sensitivity at low energies. It has, however, much higher sensitivity at $\sim$ 10 TeV due to very large FOV (nearly the entire overhead sky) and a very large duty cycle since observations can be performed during moon periods and even daylight hours. The successor to the Milagro experiment is the HAWC experiment, currently under construction in Mexico, which will have unprecedented sensitivity at the highest Gamma-ray energies yet detected.

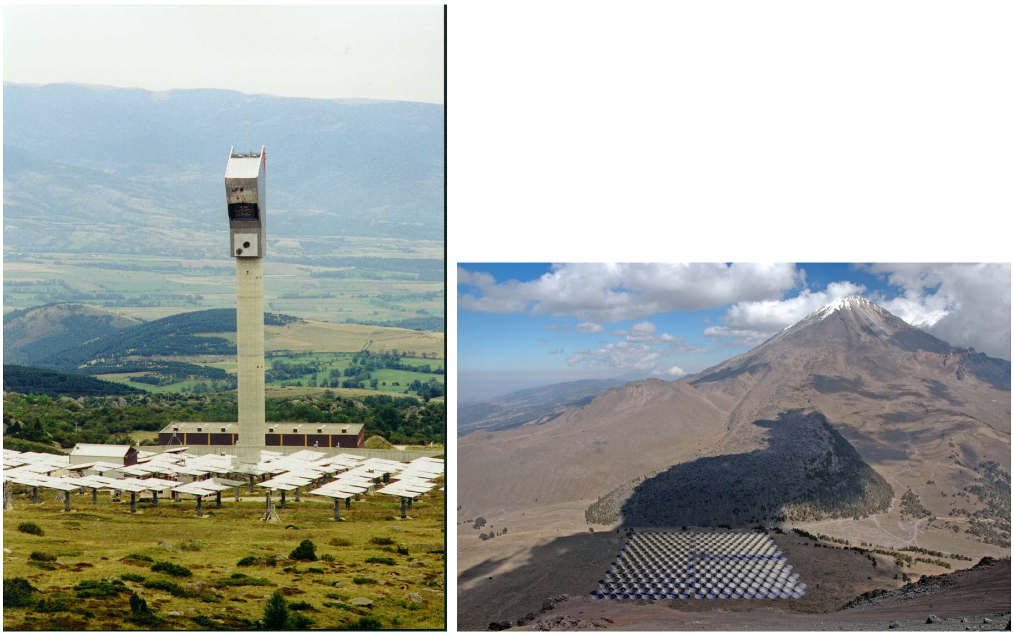

Figure 1.8: Left: the CELESTE solar farm in France was converted into a Gamma-ray Cherenkov wavefront sampler. Right: HAWC, a Gamma-ray observatory currently under construction in Mexico, will use water Cherenkov tanks to detect charged particles from air showers as they reach ground level.

1.2.5 Imaging Atmospheric Cherenkov Telescopes

Electromagnetic showers are typically initiated by Gamma-rays at an altitude of ∼10-20 km. The resulting cascade of charged particles then produces a flash of Cherenkov radiation lasting between 5 and 20 ns. The total area on the ground illuminated by this flash corresponds to many hundreds or thousands of square meters, which is why the effective area of IACT telescopes is so large (Figure 1.9).

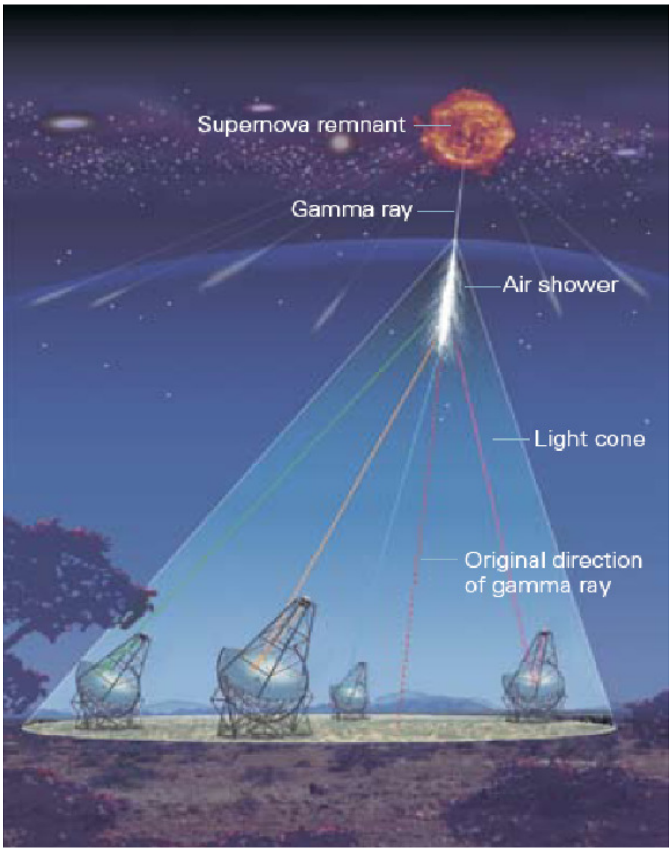

Figure 1.9: The Imaging Atmospheric Cherenkov Technique. VHE Gamma-rays from cosmic sources produce air showers in the Earth's atmosphere. These showers produce Cherenkov radiation as they pass through the atmosphere which can be imaged by an array of ground based telescopes.

As will be discussed in later chapters, one of the key advantages of the imaging method is its ability to better distinguish between showers of hadronic or Gamma-ray origin. This is done based on differences in the shapes and sizes of the shower images from the two sources, although, hadronic shower fluctuations can be large and there will, therefore, always be some contamination from hadronic showers, on the order of 1% of the cosmic-ray background, masquerading as electromagnetic showers. This residual background is then modeled and subtracted.

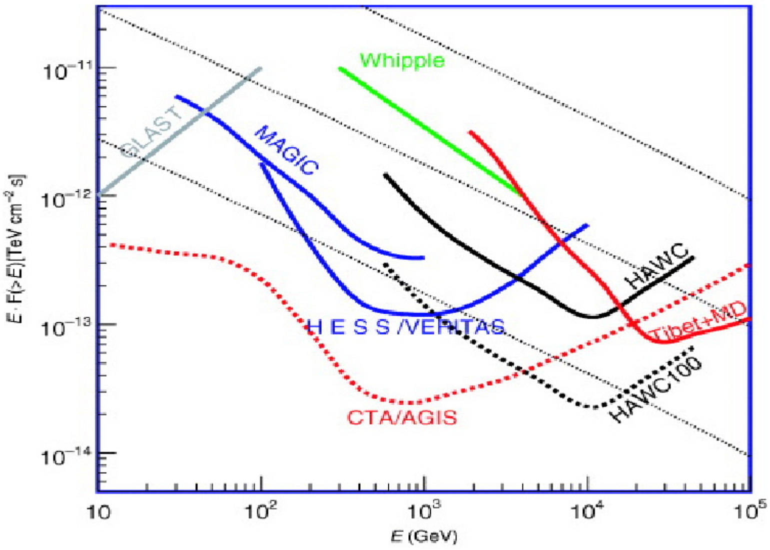

Figure 1.10: Sensitivity of various Gamma-ray observatories. The space telescope GLAST (now known as Fermi) covers the lowest energies (MeV to GeV), with H.E.S.S. and VERITAS having currently the highest sensitivity in the range $\sim 0.5 - 10$ TeV, and MAGIC filling the gap between the two ranges. The HAWC experiment (currently under construction) will extend sensitivity to nearly 100 TeV. The future planned CTA observatory (recently joined by the AGIS collaboration) will be capable of observing all currently covered energy bands at an unprecedented sensitivity.

In 1971, the Smithsonian group published the first detection of an astrophysical source of Gamma-rays by an IACT [Fazio et al., 1972] at a 3 σ level after three years of observations. Since then, the sensitivity of IACTs has grown immensely (Figure 1.10). The H.E.S.S. telescopes, for example, are capable of detecting a source with a flux of 1% of the Crab flux at a 5 σ level after 25 hours of observation at zenith [Acero et al., 2011]. This vastly improved sensitivity has lead to a rapid rise in the number of known Gamma-ray sources (see Figure 1.11).

The leading competitors in the field are currently VERITAS, in Arizona, MAGIC, in the Canary Islands, both of which are in the northern hemisphere and, therefore, view the norther sky, and H.E.S.S. in Namibia which observes the southern sky making the Galactic Center, with its large concentrations of matter and VHE sources, visible (see Figure 1.1). The next generation of imaging Cherenkov telescopes is represented by the planned Cherenkov Telescope Array (CTA) which will have up to 100 telescopes and be operated as an observatory, instead of the experiment model, allowing outside observation proposals and public data.

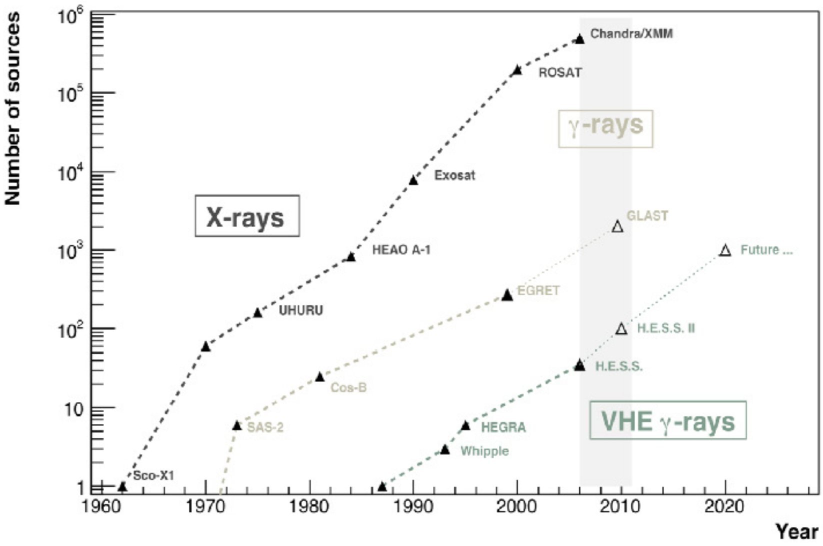

Figure 1.11: Number of Gamma-ray sources vs. time. The Crab nebula was the first TeV Gamma-ray source detected in 1989. Since then, the number of known TeV emitters has grown to over 100 and future experiments (such as CTA) are expected to be able to detect on the order of ~ 1000. Figure taken from S. Funk et. al., KIPAC Tea Talks 2010.

2 H.E.S.S. - The High Energy Stereoscopic System

Figure 2.1: The H.E.S.S. array of four IACTs in Namibia.

H.E.S.S. is an array of four IACTs (Figure 2.1) situated in the Khomas Highland of Namibia (23°16′18″ South, 16°30′00″ East), at an elevation of 1800 m above sea level. The total field of view of each detector is 5° in diameter which makes H.E.S.S. well suited to carrying out surveys of the souther sky, including the Galactic plane [Aharonian et al., 2006e]. H.E.S.S. is sensitive to Gamma-rays in the energy band $\sim$ 100 GeV to $\sim$ 100 TeV, although the true energy threshold will depend on many factors including the zenith angle at which the observations are taken. Requiring showers to be imaged by more than one telescope (stereo mode) improves background rejection [Berge et al., 2007] and energy and direction of origin reconstruction, resulting in a point spread function (PSF) of better than 0.08° per event, enabling many extended galactic TeV sources to be resolved [Aharonian et al., 2006e].

2.1 The Telescope System

The four H.E.S.S. telescopes are arranged in a square formation with a side length of 120 metres. This distance was optimised for maximum sensitivity at the planned energy threshold of 100 GeV. Cameras mounted at the focal point of each telescope image the showers. This data is then sent to the central trigger and, if enough telescopes trigger, the data from the individual cameras is then sent to the central computer farm for storage and online analysis and monitoring. Also, weather monitors record atmospheric conditions which may effect data quality and shower reconstruction.

2.1.1 H.E.S.S. Telescopes

The H.E.S.S. telescopes are of steel construction, with altitude/azimuth mounts capable of precisely tracking any source from 0.0° to 89.9° in elevation, with a slew rate of 100° per minute [Aharonian et al., 2004].

Each telescope has a spherical dish, 13 m in diameter, consisting of 380 individual mirrors giving an overall reflective area of 107 m^2. Cherenkov radiation, produced in extensive air showers, is collected by the mirrors and focused onto a camera. The mirrors are remotely adjustable under computer control, and a fully automated procedure is used, in conjunction with a CCD camera mounted in each dish, for optimal alignment onto the focal plane of each telescope camera, 15 m from the mirrors. Details of the mirror alignment system and the optical point spread function are discussed by Cornils et al. [2003b].

2.1.2 H.E.S.S. Cameras

Figure 2.2: H.E.S.S. Camera consisting of 60 drawers each with 16 PMTs

The H.E.S.S. cameras (Figure 2.2) each consist of a hexagonal array of 960 Photonis XP2960 PMTs. Each tube corresponds to an area of 0.16° in diameter on the sky, and is equipped with Winston cones to capture the light which would fall in between the PMTs, and also to limit the field of view of each PMT in order to minimise background light. The camera is of modular design, with the PMTs grouped in 60 interchangeable modules, or “drawers”, of 16 tubes each [Vincent et al., 2003], which contain the trigger and readout electronics for the tubes, as well as the high voltage supply, control and monitoring electronics. Further details of the optical structure are given by Bernlöhr et al. [2003] and Cornils et al. [2003a].

2.1.3 Data Aquisition

The trigger system of the H.E.S.S. array consists of three levels. First, a single pixel trigger threshold is required, equivalent to about 4 photo-electrons (p.e.) at the PMT cathode within an interval of 1.5 nanoseconds. Second, a coincidence of 3 triggered pixels is required within a sector - a square group of 64 pixels - in order to trigger a camera. Each camera has 38 overlapping sectors. Third, when the detector is operating in stereo mode, a coincidence of two telescopes triggering within a window of (normally) 80 nanoseconds is required. Only cameras which have individually triggered are read out in a stereo event. The stereo trigger system and the trigger behavior of the HESS array is described by Funk et al. [2004]. During the first and second level trigger formation, the individual signals from each pixel are stored in two analogue ring sampler (ARS) circuits. A high gain and a low gain channel are used to give optimal signal dynamic range. The signals captured by each tube are digitised in the drawer, before being collected by a central CPU in the camera and sent to the central data acquisition system (DAQ, Figure 2.3) by optical ethernet connection [Borgmeier et al., 2003]

2.2 Data Collection and Analysis

The telescopes are operated every night during *dark period*, i.e. when the moon and sun are below horizon for at least ~ 1 hour, weather permitting. Members of the collaboration take shifts of length one moon cycle and operate the telescopes from the control room as seen in Figure 2.5. The shifters are responsible to queue observations and calibration runs and monitor telescope performance and weather conditions. Online data analysis is performed producing real-time shower images and reconstructed sky histograms (see Figure 2.4).

2.2.1 Data Collection

The telescopes are normally operated in coincidence mode where only showers which are imaged in two or more telescopes are recorded. Observations with H.E.S.S. are typically made in "wobble mode" whereby the source is offset by a small distance (typically $\sim 0.5°$ for point-like sources) from the camera center, within the field of view, alternating between 28 min runs in the positive and negative declination or right ascension directions. This method of observation was pioneered by the HEGRA collaboration [Daum et al., 1997] and allows for efficient use of the large field of view (FOV) of modern IACTs: i.e., there is no need to take aditional background observations since the large FOV typically

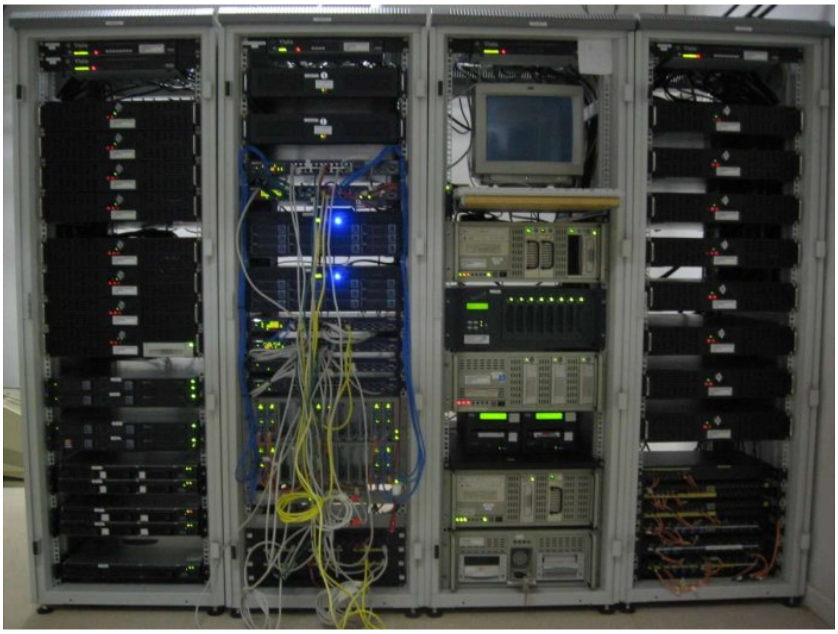

Figure 2.3: The H.E.S.S. data acquisition farm, where data is collected from the four telescopes, telescope triggers are evaluated and on-line shower reconstruction and analysis takes place. Photo provided by Matthew Dalton (2007) from the H.E.S.S. farm room.

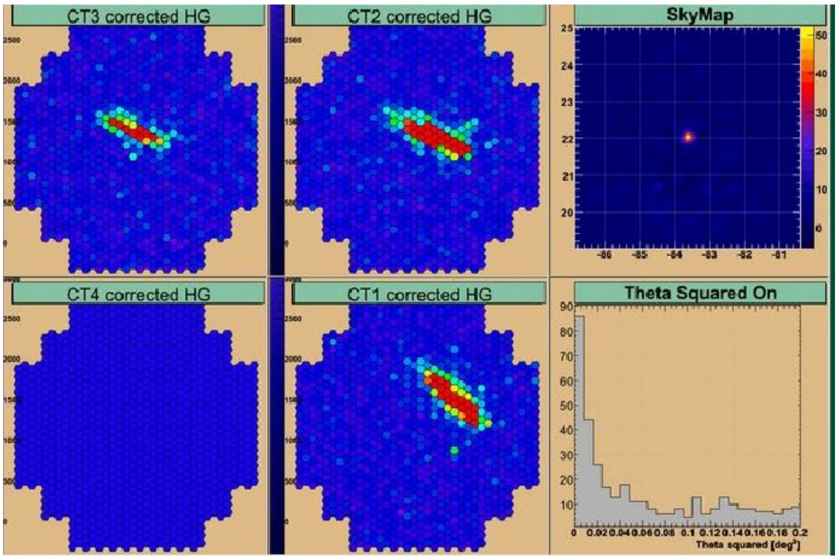

Figure 2.4: Shower images as seen by the H.E.S.S. cameras and displayed via the online analysis. Screen shot provided by Matthew Dalton (2007) from the H.E.S.S. control room.

Figure 2.5: The H.E.S.S. control room, where operators schedule observations and monitor telescope performance and weather conditions. Photo provided by Matthew Dalton (2007) from the H.E.S.S. control room.

includes regions far from the source position to allow the background to be determined from the same observation. This results in more efficient use of limited dark time.

Light collected by the telescopes is focused on the PMTs in the cameras. A single incident photon may produce a photo electron (p.e., with the probability of coversion given by the quantum efficiency) which is amplified through strong voltage. The resulting current is then quantized by a linear map to digital "counts", determining signal strength, using an analog to digital converter (ADC).

2.2.2 Detector Calibration

The quantum efficiency of the PMTs can change with temperature, voltage and age of the PMTs. Mirror reflectivity may become degraded through sand abrasions in wind storms in the Namibian desert. Also, noise in the camera electrons, background light from scattered star light and thermal photo electrons in the PMTs add to the background of the signals. Because of these, it is necessary to take calibration data frequently.

In an "electronic pedestal run" the PMT signals are read out randomly in order to estimate the noise in the single pixels with the lids closed and the high voltage turned on. "Single p.e. runs" use a pulsed LED into the camera with an intensity such that on average there is ~ 1 p.e. per PMT per event, giving conversion coefficients from single p.e. to ADC counts, with camera lid open and HV on but inside the camera hut in order to avoid contamination with NSB. In order to correct for differences in the single PMT efficiencies, "flatfielding runs" use LEDs at the center of the cameras to illuminate the telescope mirrors which is then reflected uniformly back to the camera, highlighting the relative differences in individual pixel efficiencies.

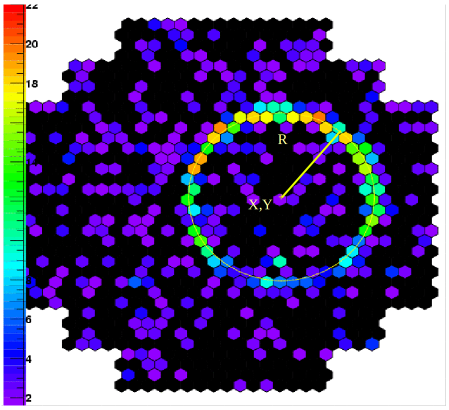

Figure 2.6: The Cherenkov ring produced by a single muon as recorded by the H.E.S.S. telescopes. These images are compared with Monte Carlo expectations and used to determine optical efficiency of the detectors. Figure taken from talk by Leroy Nicalas at the 28th IRCR, 2003

The optical efficiency of the telescopes (i.e. the efficiency of conversion of optical photons into ADC counts in the detectors) changes with time, the biggest contributing factor being the degradation of the mirror reflectivity due to the harsh conditions of the desert environment and weather. These changes happen over periods of months to years and have the effect of reducing image intensity and therefore reducing the reconstructed energy of the events.

This effect is corrected for by scaling the image intensities by the ratio of the measured optical efficiency of the telescopes to the optical efficiency derived from Monte Carlo simulations (E_m/E_{mc}). To measure the optical efficiency, observations known as "muon runs" are performed where the camera triggers are set to record Cherenkov "rings" from single muons (Figure 2.6). Conversely, such muon rings can also be obtained from the images of normal background events, removing the need for dedicated muon runs. The light produced by the muons can be well modelled and this can then serve as a check on the total optical efficiency including mirror reflectivity and PMT response.

Also, *pointing runs* are taken periodically to assure accurate knowledge of the telescope tracking system. With the camera lids closed, CCD cameras are used to image stars focused by the mirrors. Effects such as bending of the telescope frame due to the weight of the cameras, settling of the telescope foundation and even hysteresis of the tracking system can be corrected for using the data collected in this way.

2.2.3 Data Quality Selection

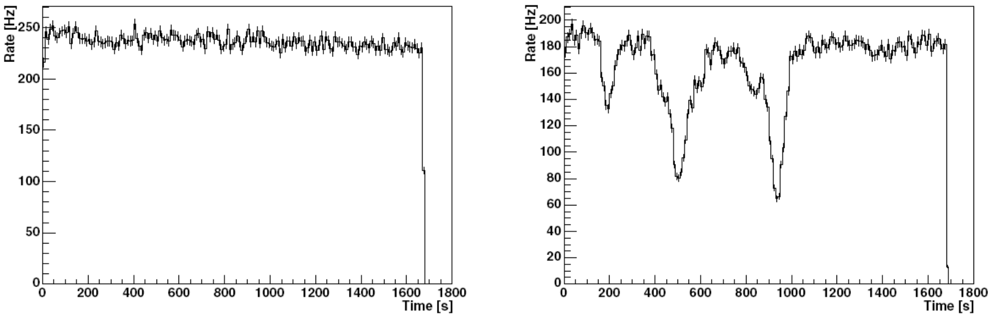

(a)

(b)

Figure 2.7: The system rate vs. time within a run for a) a 4 telescope run passing the run selection, b) a 3 telescope run failing the run selection. The run is removed from further analysis due to the instability in the rate caused by clouds passing through the field of view. Differing zenith angles of the observations as well as a different number of telescopes taking part in the observations leads to a difference in the absolute event rates. Figure taken from Berge et al. [2007].

Systematic uncertainties on the measured flux and energy spectrum may be minimized by rejecting data recorded under non-optimal conditions. In the case of HESS J1303−631, for example, although a total of 158 h of observations were made, only 108 h are included in the analysis presented in Chapter 5. The remaining observations have been rejected as not meeting the run quality criteria. Some observations were made with complicated sky conditions, such as the presence of clouds or excessive dust in the atmosphere, which can lead to the absorption of Cherenkov light and thus fluctuations in the system trigger efficiency, causing systematic uncertainties in the reconstructed energy and thus the derived Gamma-ray flux, and also effecting the threshold energy for detection and the resulting trigger rate. Figure 2.7 shows the trigger rate as a function of time for two observations, one with a stable system trigger rate close to the predicted level for this zenith angle, the other exhibiting variability due to the presence of clouds. Observations for which the mean trigger rate is less than 70% of the predicted value (as discussed by Funk et al. [2004]), or for which the rms variation in the trigger rate is above 10%, are removed from the analysis.

2.2.4 Shower Reconstruction and Background Rejection

In order to analyse the data, images of air showers must first be cleaned and then parameterized to reconstruct the air showers and remove background on a statistical basis. The images are cleaned by removing noisy pixels (which may indicate broken PMTs)

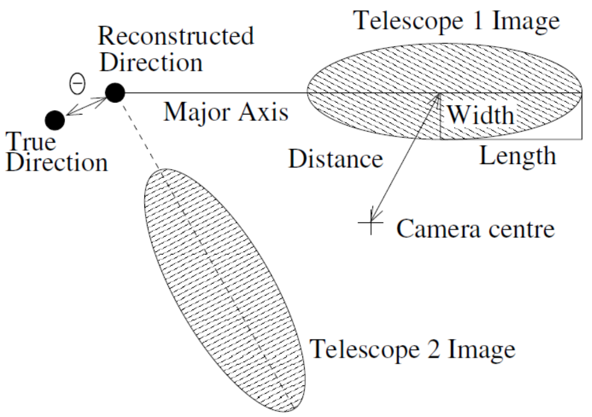

Figure 2.8: Definition of simple Hillas parameters, calculated for a Gamma-ray image, which may be approximated as a narrow ellipse. Important parameters for this analysis are the width, length, distance and orientation. An image from a second telescope is superimposed to demonstrate the geometrical technique for source position reconstruction. The parameter θ, which is the magnitude of the angular offset in shower direction reconstruction, is also shown.

and pixels with very low current, mostly due to noise from the night sky background (NSB).

Image Parameters

Hillas [1985] made a series of Monte Carlo simulations of the images of Gamma-ray and cosmic-ray showers in IACT cameras. There, it was shown that the shower images of hadronic and electromagnetic showers differ significantly enough to enable the rejection of the majority of hadronic showers. Thus, by approximating the shower as an ellipse and applying cuts on the parameters describing the shower ellipses, the background can be significantly reduced.

The image parameters used for the H.E.S.S. analysis are as follows:

I Length l: the ellipse semi-major axis

II Width ω: the semi-minor axis

III center of gravity c_g

IV distance d between camera center and c_g

V image size s: the integrated sum of pixel intensities

VI pixel number n_p: total number of pixels in image

VII θ, the angluar distance between true and reconstructed shower direction

These parameters are shown in Figure 2.8.

The shower directions of origin are reconstructed by intersecting the major axis of the various shower images using one of the algorithms described in Hofmann et al. [1999] (the simplest method is also shown in Figure 2.8).

Gamma/Hadron Separation

The *mean scaled parameter* method, similar to that used by the HEGRA collaboration [Daum et al., 1997], is used to classify images as either Gamma-ray like or hadron like, in order to reject non Gamma-ray background events. The scaled parameter is defined as

$$p_{sc} = (p - \langle p \rangle)/\sigma_p \tag{2.1}$$

where the parameter p can be either the width, ω, or the length, l, as described above. When analysing real data, the reconstructed impact parameter is used along with the image amplitude for each telescope image to find $\langle p \rangle$ and σ_p in the lookup table filled from simulated MC Gamma-ray showers. Linear interpolation (in $\cos(Z)$) between the two nearest simulated values is then done to find the correct value for a particular observation zenith angle. The mean reduced scaled width (MRSW) and the mean reduced scaled length (MRSL) are then calculated by averaging over the telescope images passing the image amplitude selection cut for each event: MRSW $= \Sigma_{tel} p_{sc}/N_{tel}$

Then Gamma selection cuts are applied to the recorded images to remove background. The cuts on the mean scaled parameters, image intensity and θ^2 are simultaneously optimized to maximise the detection significance (σ, as defined by Li and Ma [1983]) for point-like sources with typical fluxes and energy spectra. The optimisation population consists of a mixture of Gamma-ray simulations (selected to give the desired flux and spectrum for optimisation) and real background data. In the presence of background, the significance achieved for a given source increases with the square root of the observation time, t_{h}. The optimised cuts yield the maximum $\sigma/\sqrt{t_{\mathrm{h}}}$ for a source of a given type.

The standard set of shower selection cuts has been optimised to give the maximum significance for a flux 10% of the Crab (“standard” cuts), with a similar photon index (i.e. 2.59). The “hard” cuts are optimised for a source with a flux 1% of the Crab flux, and a photon index of 2.0. These cuts give a higher significance for weak, hard spectrum sources, at the expense of energy threshold and cut efficiency. The hard cuts are also useful as they reduce the systematic uncertainties in sky-map reconstruction by reducing the numbers of background events, relative to the signal. They also give a narrower PSF than the standard cuts, as the higher intensity cut (a cut on “image size”) selects better reconstructed events. A set of “loose” cuts have been also optimised to give the maximum significance for a strong source, similar to the Crab, and a photon index of 3.0. The reduced intensity cut for loose cuts reduces the energy threshold of the analysis relative to the standard cut, and the fraction of events passing the cuts is higher. When conducting source searches, the standard cuts are always used unless there is an a priori reason to expect a very hard or very soft spectrum from the source.

Figure 2.9 shows a comparison between the MRSW from Monte Carlo simulations of protons and Gamma-rays and from real data at a zenith angle of 50°. It can be seen that the data (before selection cuts) correspond well to Monte Carlo simulated protons, as expected, while there is good separation between the data and Monte Carlo simulated Gamma-rays, which are chosen to have a photon index of 2.59, similar to the Crab energy spectrum. The results of the selection cut optimisations are shown in Table 2.1.

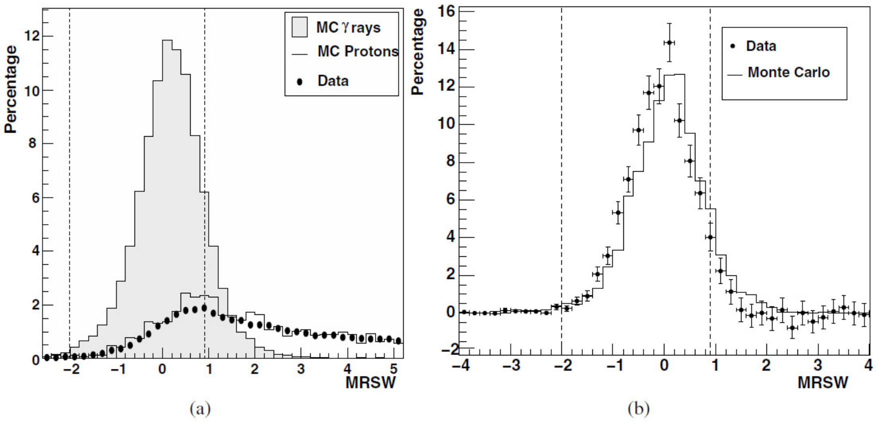

(a) (b)

Figure 2.9: The distributions of mean reduced scaled width (MRSW) for Monte Carlo Gamma-ray events a) with Monte Carlo proton simulations and actual off data before selection cuts, b) with real events from the direction of the Crab nebula (data set II) after selection cuts and background subtraction. The vertical lines denote the standard cuts described in Table 2.1. Figure taken from Aharonian et al. [2006a].

2.2.5 Backgroud Modelling

Despite the drastic reduction in cosmic-ray background after application of Gamma-like event selection cuts, as described above, there still remains some background in the data. The distribution of background events is usually assumed to be azimuthally symmetric within the camera field of view, although this may not always be true.

In order to estimate the background, an integration region, referred to here as the *off region*, is taken, typically larger than the signal integration region, which is likewise referred to as the *on region*. Several models have been developed for choosing an off region, each with its relative advantages and disadvantages.

When estimating the background, first the reconstructed shower direction for each Gamma-like event (i.e. an event that passed the selection cuts) is filled in a two dimensional histogram (so-called *sky-map*). The *on* signal for a given point in the sky is determined by selecting events within a circle around that point with radial θ cut, in other words, this cut defines the integration radius. Several techniques have been developed to derive estimates of the background level within this region of the field of view. The two most common are the “ring” and “reflected region” background models discussed below.

Ring background model

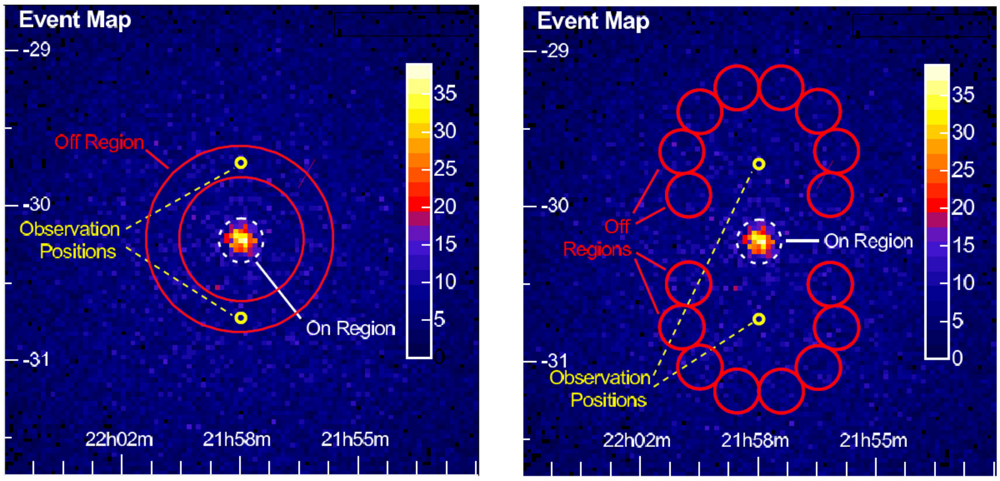

Figure 2.10: Count map of Gamma-ray-like events from 5 hours of H.E.S.S. observations of the active galaxy PKS 2155−304 [Aharonian et al., 2005d]. The data were taken in wobble mode around the target position with alternating offsets of ±0.5° in declination shown by the yellow circles. The ring- (left) and reflected-region- (right) background models are illustrated schematically. Image taken from Berge et al. [2007].

The ring-background technique determines the background for each position in the field of view using the background rate contained in a ring around that position as shown in Figure 2.10 left, similar to the method used by HEGRA (see Puehlhofer and HEGRA Collaboration [2003]). The internal and external radii of the ring are typically chosen such that the ratio of the areas of the off to on regions is close to 7, which makes for a compromise between area within the ring and distance from the on region. The inner ring radius is chosen to be significantly larger than the on region, in order to avoid signal leakage into the off region. The normalisation (α) is given by the area ratio modified by a weight factor to account for the radial background acceptance in the camera. When estimating the background for a test position close to a known source like the Crab nebula, the source position is cut out of the background ring in order to avoid signal pollution in the off region for the test position. This method has the advantage of allowing background estimation for all positions in the field of view. This method is prefered for the production of sky maps because, unlike the reflected region background method, it can be applied at every point in the field of view, including at the center.

Reflected region background model

The reflected region background model is well suited for observations taken in the standard wobble-offset mode. It uses a number of background regions equidistant from the observation position (see Figure 2.10, right). The combined events from these positions are used to estimate the background at the on position, scaled by the relative area of the on and off regions. In the case of a larger integration region the number of background regions is reduced to eliminate overlapping. The normalisation, α, is the ratio of the solid angles of the on and off regions. As the off positions are the same distance from the center of the field of view as the on position, correction for the relative radial background acceptance of the detector is not required. However, this method cannot be used for positions closer to the center of the field of view than the radius of the on region, as the background positions would overlap with the source position, so observations where the region of interest lies within 0.5° of the center of the camera are ignored. This method is preferred when generating spectra because of its ability to correct for gradients in the field of view.

Configuration	MRSL Min.	MRSL Max.	MRSW Min.	MRSW Max.	θ^2 Max ($\deg^2$)	Image Amp. Min. (p.e.)	Distance Max.(°)
Standard	-2.0	2.0	-2.0	0.9	0.0125	80	2.0
Hard	-2.0	2.0	-2.0	0.7	0.01	200	2.0
Loose	-2.0	2.0	-2.0	1.2	0.04	40	2.0
Extended	-2.0	2.0	-2.0	0.9	0.16	80	2.0

Table 2.1: Selection cuts optimised for various purposes, as described in the text. Cuts are applied on MRSW and MRSL, as well as on the distance (θ) from the reconstructed shower position to the source. A minimum of two telescopes passing the per-telescope cuts, on image amplitude and distance from the center of the field of view, are also required. Standard cuts, as well as hard, loose and extended cuts are listed.

3 Pulsars and Pulsar Wind Nebulae

Pulsars (from "pulsating stars") were first observed in 1967 by Jocelyn Bell Burnell through the detection of periodic radio pulsations. Originally of unknown origin, it quickly became obvious that these sources represented a new kind of star. The very short periods associated to these pulsations (~ seconds to miliseconds) implied that the objects must be quite small. The year after their discovery, Thomas Gold and Franco Pacini independently suggested that pulsars were rotating magnetized neutron stars, and this was soon proven beyond reasonable doubt by the discovery of a pulsar with a very short (33-millisecond) pulse period in the Crab nebula.

3.1 Properties of Pulsar

Pulsars are now known to be created in Supernova events, where the dense stellar core created in thermonuclear reactions is left over after the nova event. Depending on its mass, the remaining solar core may form a neutron star or a black hole. The determining criterion is the Chandrasekhar limit (M_{Ch}) given by:

$$M_{Ch} \approx \left(\frac{\hbar c}{G}\right)^{\frac{2}{3}} \frac{1}{m_p^2} = 1.44 M_\odot \tag{3.1}$$

where $\hbar$ is the reduced Planck constant, c is the speed of light, G is the gravitational constant, m_p is the mass of a proton and $M_\odot = 2 \times 10^{30}\,\mathrm{kg}$ is the mass of the sun. For masses exceeding M_{Ch}, the gravitational pressure exceeds the electron degeneracy pressure inside the core, such that the atoms are compressed. Electron capture by the nuclei is the consequence which leads to the formation of neutrons by inverse β decay ($p^+ + e^- \rightarrow n + \nu_e$), resulting in an extremely compact state of matter - a neutron superfluid.

Pulsars have been observed in the range ~ 1 - 2 solar masses and have a radius of about 12 km, according to the Akmal-Pandharipande-Ravenhall equation of state, with densities comparable to an atomic nucleus. However, an upper mass limit for a neutron star is reached at $\sim 2.5\,\mathrm{M}_\odot$, where gravitation compresses the neutron star below its Schwarzschild radius, converting it in a black hole. Between these two extremes, it is possible that a third type of compact star exists, namely the quark star, where gravitational pressure is so great as to reduce the matter in the star to a quark/gluon plasma. It is not yet clear, however, if these stars are realized in Nature [Klähn et al., 2007].

Three types of pulsars are known, categorized by their primary power source:

I Rotation-powered pulsars, where the loss of rotational energy of the star provides the power.

II Accretion-powered pulsars (accounting for most but not all X-ray pulsars), where the gravitational potential energy of accreted matter, typically from a binary companion star, is the power source.

III Magnetars, where the decay of an extremely strong magnetic field provides the electromagnetic power.

3.1.1 Pulsar Energy Loss

The rotational kinetic energy in a pulsar, $E_{rot} = \frac{1}{2}I\Omega^2$, where $\Omega = 2\pi/P$, is the main source of energy powering a pulsar wind nebula. Pulsars are found to have a characteristic spin period, P, and a period derivative, $\dot{P}$, which is negative in non-accreating pulsars. This slow down of the period implies a loss of rotational kinetic energy, known as the pulsar's "spin-down luminosity", $\dot{E} = -dE_{rot}/dt$, given by

$$\dot{E} = 4\pi^2 I \frac{\dot{P}}{P^3} \tag{3.2}$$

where I is the neutron star's moment of inertia and is usually assumed to have the value 10^{45} g cm^2. The value of the spin-down luminosity can be measured empirically simply by measuring the spin period over long time intervals.

The pulsar's rotational energy is believed to be carried away by a wind consisting of relativistic electrons and positrons, accelerated in the pulsar's powerful magnetic field, and by an electromagnetic dipole radiation generated by the rotating magnet.

3.1.2 Characteristic Age and Braking Index

For a magnetic field with component $B_\perp$ perpendicular to the axis of rotation, the electromagnetic dipole radiation is $\frac{2}{3}B_\perp^2 c^{-3}\Omega^4$. If the pulsar spin-down luminosity was due entirely to electromagnetic dipole radiation we would then have

$$\left(\frac{dE}{dt}\right)_{em} = -I\Omega\dot{\Omega} = \frac{2}{3}\frac{B_\perp^2}{c^3}\Omega^4 \Leftrightarrow \dot{\Omega} = -\frac{2}{3}\frac{B_\perp^2}{Ic^3}\Omega^3 \tag{3.3}$$

Careful observations of pulsar timing over periods of many years have shown that this does not in general hold. The more general form describing the frequency derivative is given as such:

$$\dot{\Omega} = -K\Omega^n \tag{3.4}$$

where K is a constant and n is known as the "braking index". The braking index can be solved for by taking the derivative and then plugging back in to Equation (3.4), yielding

$$n = \frac{\Omega\ddot{\Omega}}{\dot{\Omega}^2} \tag{3.5}$$

The braking index has only been reliably measured in 6 pulsars (mostly because of difficulties caused by timing noise). However, in all cases it has been found to be less than 3 [Livingstone et al., 2007], the value expected from magnetic dipole radiation, as above.

Integrating the spin-down model from Equation 3.4 we get

$$t = -\frac{\Omega}{(n-1)\dot{\Omega}}\left(1 - \frac{\Omega^{n-1}}{\Omega_0^{n-1}}\right) \tag{3.6}$$

where the initial angular velocity, Ω_0, has decayed to the current value, Ω, in the time t. This, with the assumption that the birth angular velocity was much larger than the current angular velocity $\Omega_0 \gg \Omega$, reduces to

$$t = -\frac{1}{(n-1)}\frac{\Omega}{\dot{\Omega}} \tag{3.7}$$

This could be used to determine the age of a given pulsar, but since the braking index is in general not known, one can assume the braking index for pure electromagnetic dipole radiation, $n = 3$, and define this as the "charactaristic age", τ:

$$\tau \equiv \frac{1}{2}\frac{\Omega}{\dot{\Omega}} = \frac{P}{2\dot{P}} \tag{3.8}$$

There are currently more than 1,800 pulsars in the ATNF on-line catalog [Manchester et al., 2005], with rotation periods in the rage $0.0016 - 12$ seconds (Figure 3.1) and derived spin down luminosities in the range $3.2 \times 10^{28} - 4.9 \times 10^{38}$ erg/s.

3.1.3 Pulsar Magnetosphere

The first theoretical model solving the magneto-hydrodynamic (MHD) equations for a pulsar was provided by Goldreich and Julian [1969]. Since the pulsar is taken to be a superconductor, the magnetic field inside the pulsar must be zero, requiring a layer of charges at the surface of the star to cancel out the magnetic field. The rotating magnetic dipole, however, also produces a quadrupole electric field whose component is parallel to the open magnetic field lines at the poles. Assuming that the pulsar is surrounded by a vacuum, it was found that the electrical force on an electron or proton in the surface charge layer of the pulsar in the direction of the magnetic field would be many orders of magnitude greater than the gravitational force in the same direction and the system would thus not be in dynamical equilibrium and the electric field extracts particles very effectively from the neutron star surface and accelerates them to highly relativistic energies.

The pulsar must, therefore, be surrounded by a dense co-rotating magnetosphere consisting of a charged plasma. The plasma density is given by the Goldreich-Julian charge

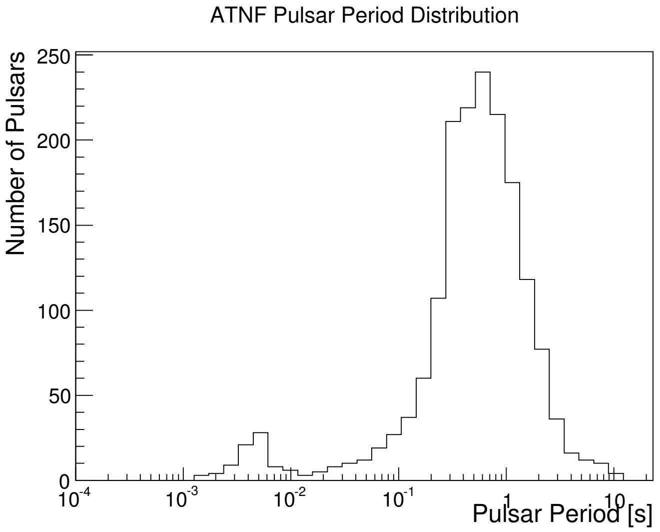

Figure 3.1: The distribution of measured pulsar periods from the ATNF pulsar catalog [Manchester et al., 2005]. The smaller peak to the left represents the "milisecond pulsars" which are believed to be a separate population of pulsars which have been "spun-up" by infalling material from a companion star.

density:

$$\rho_{\mathrm{GJ}} = \frac{\nabla \cdot E}{4\pi} = -\frac{\Omega \cdot B}{2\pi c}\left[1 - \left(\frac{\Omega r}{c}\right)^2 \sin^2\theta\right] \tag{3.9}$$

This plasma filled region should lie inside the "light cylinder", defined as the distance from the pulsar at which a co-rotating object would travel at the speed of light, i.e. $R_L = c/\Omega \approx 5 \times 10^9 P\,\mathrm{cm}$, where P is the rotation period in seconds, see Figure 3.2. Due to the intense magnetic field of the pulsar, charges are confined to move along the magnetic field lines and must, therefore, be co-rotating. This co-rotating charged plasma within the light cylinder is referred to as the "magnetosphere".

A high energy electron traveling along the magnetic field lines will produce curvature radiation, which, in the intense magnetic field, will pair produce and the resulting electrons and positrons will be accelerated by the electromagnetic field, again producing curvature radiation. This cascading effect is referred to as a "pair-production avalanche" and is a process which may be responsible for populating the magnetosphere with the required charge density and replacing any charges which may leave the system along open field lines.

It is clear from observations, as shown earlier, that there must be a wind of cold relativistic charged particles, likely leptons, flowing from the region around the pulsar out toward the standing shock region. The observed polarized coherent synchrotron radiation from the magnetosphere over many orders of magnitude in energy is believed to be produced by the electrons which are accelerated in the magnetosphere. Exactly how and where

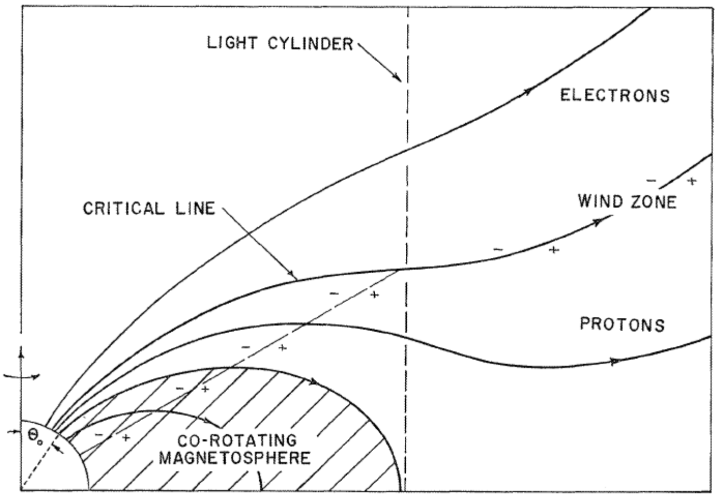

Figure 3.2: Schematic diagram showing the co-rotating pulsar magnetosphere and wind zone. The pulsar is located in the lower left and the rotation axis is shown. (Figure taken from Goldreich and Julian [1969].)

within the pulsar magnetosphere these particles are accelerated remains somewhat a mystery.

There are, however, currently several competing models to explain this acceleration process. Details of the competing theories of particle acceleration will not be presented here, however, the two most commonly accepted sites for this acceleration are the “Polar Cap”, near the stellar surface [Daugherty and Harding, 1996], and “Outer Gap”, near the light cylinder [Romani, 1996].

These are theories about the acceleration of particles in the magnetosphere, but they also make testable predictions about the pulsed emission of the pulsar. As the particles are accelerated, they are confined to move along the magnetic field lines, so that escaping particles must move along open field lines originating near the magnetic poles. Thus, when the magnetic poles sweep past our field of view, the accelerated particles emit synchrotron and curvature radiation which is beamed toward us and detected on Earth as a pulse. Observations of pulsed emission, therefore, are often used to search for signals to distinguish between the various theories, for example whether the Gamma-ray spectrum in GeV energies will have either an exponential cutoff, as predicted by outer gap models, or a superexponential cutoff, as predicted by polar cap models due to extinction of high energy photons in the pulsar’s magnetic field. Such searches are currently being performed, e.g., with the Fermi Gamma-ray space telescope [Abdo et al., 2010]. It is possible that one or more of these processes is responsible for the acceleration of the electrons and those which escape carry away the pulsar’s rotational energy producing the pulsar wind.

3.2 Pulsar Wind Nebulae

As the wind from a pulsar flows out from the pulsar's light cylinder, it is initially "cold", meaning that the momenta of the particles are not isotropically distributed. Therefore, the particles in the "wind zone" do not radiate except possibly in Gamma-rays through inverse Compton scattering. Eventually, however, the wind reaches the interstellar medium. Interaction of this wind with the surrounding medium causes a standing termination shock wave [Rees and Gunn, 1974] which is believed to be the location of acceleration of particles to very high energies (see Figure 3.3).

3.2.1 The Wind Zone

The energy contained in the wind consists of two parts, the Poynting flux, $F_{E\times B}$, and the particle energy flux, F_{particle}. Based on these fluxes one can determine the so called magnetization parameter, σ, defined as

$$\sigma = \frac{F_{E\times B}}{F_{\text{particle}}} = \frac{B^2}{4\pi\rho\gamma c^2},$$

where B, ρ and γ are the magnetic field, mass density of particles, and Lorentz factor, in the wind, respectively. Evidence suggests that as the wind flows from the pulsar light cylinder to the pulsar wind shock region, at some point this parameter undergoes a drastic change. Typical values of $\sigma > 10^4$, implying Poynting flux dominated wind, are observed near the light cylinder, while values less than 1, implying particle energy dominated wind, are observed just behind the shock region. One of the best studied examples of this phenomenon is the Crab Nebula.

Kennel and Coroniti [1984] assumed that the entire spin-down luminosity of the pulsar was carried away by relativistic MHD wind with a pure electron-positron plasma. By matching the velocity and pressure of the post shock flow at the boundary of the outer Nebula, they found that $\sigma_\infty \approx 3 \times 10^{-3}$. However, models of pair-production in polar cap gaps indicate that only 10^{-4}-10^{-5} of the polar cap potential is converted into particle kinetic luminosity which would imply $\sigma_L \approx 10^4 - 10^5$ inside the light cone (i.e. $r_L = c/\Omega \approx 1.5 \times 10^8$ cm for the Crab [Ruderman and Sutherland, 1975]). Coroniti [1990] found that this discrepancy could be explained if the Poynting flux, in the form of a magnetically striped wind (see Figure 3.4), is converted into particle kinetic energy through a process of "magnetic reconnection" in the region between the light cone and the standing termination shock of the Nebula.

3.2.2 The Termination Shock

As the cold (i.e. strongly anisotropic) relativistic wind flows out from the light cylinder, it evenutally reaches a pressure equilibrium with the interstellar medium (ISM) where the bulk flow of the wind must stop creating a standing termination shock at a radius r_{ts}

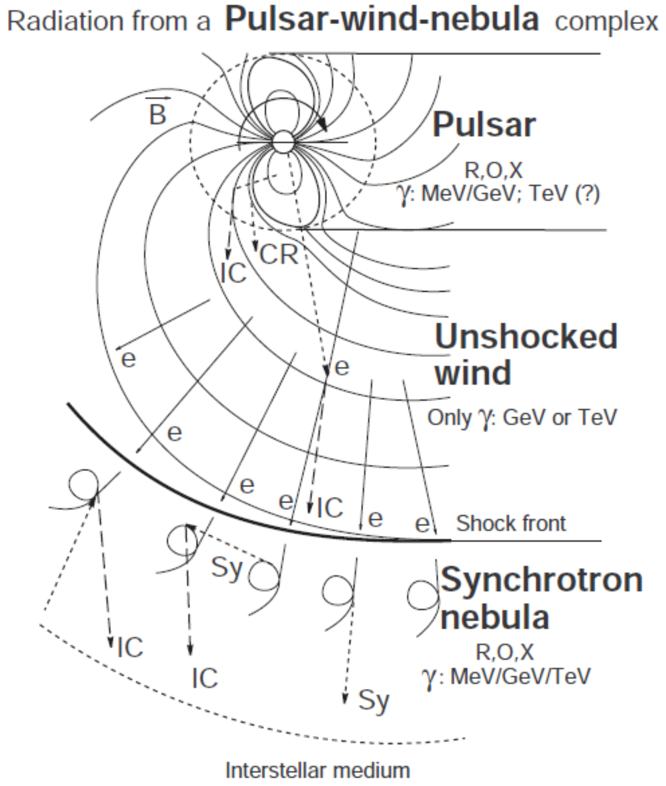

Figure 3.3: The locations and radiation mechanisms of non-thermal emission from a leptonic pulsar wind. Top: within the light cylinder where the magnetospheric pulsed radiation from radio to Gamma-rays is produced. Middle: the wind of cold relativistic plasma between the light cylinder and the shock region with radiation production through the IC mechanism. Bottom: the surrounding synchrotron nebula (plerion) which emits broad-band electromagnetic radiation from radio to multi-TeV Gamma-rays through the synchrotron and IC channels. R, O, X and γ stand for radio, optical, X-ray and Gamma-ray emission, respectively. CR, IC and Sy stand for curvature, inverse Compton and synchrotron radiation, respectively. The orientation of the magnetic field lines (B) is also indicated. (Figure taken from Aharonian and Bogovalov [2003].)

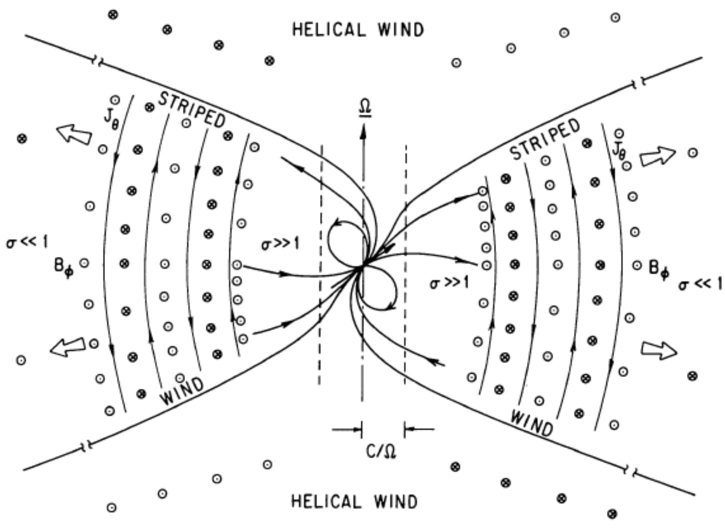

Figure 3.4: Sketch of magnetic topology in a MHD wind. The light cylinder, defined as the distance from the pulsar where a co-rotating observer would be traveling at the speed of light, i.e. $r_{\rm lc} = c/\Omega$, is shown by the dashed vertical lines. Beyond that radius, the field lines are open and expand outward in a helical structure at the speed of light. Figure taken from Coroniti [1990].

from the pulsar. For a pulsar with spindown luminosity $\dot{E}$ this radius can be calculated as follows. If the particles are assumed to be moving radially symmetrically at the speed of light, c, then the total amount of energy within the termination shock is given by $\dot{E}\frac{r_{ts}}{c}$ and the pressure is thus $\dot{E}\frac{r_{ts}}{c}/(4/3\pi r_{ts}^3)$, and setting that equal to the ISM pressure gives

$$\frac{\dot{E}}{4/3\pi r_{ts}^2 c} = P_{\rm ISM} \tag{3.10}$$

and solving for r_{ts} gives

$$r_{ts} = \sqrt{\frac{\dot{E}}{4/3\pi P_{\rm ISM} c}} \tag{3.11}$$

For example, for a moderately powerful pulsar of $\dot{E} = 10^{36}$ erg/s and, since typical values of the pressure of the ISM range from 10^3 to 10^4 K cm^{-3} [Jenkins, 2004], such a pulsar would have a termination shock radius of ~ 0.8 to 2.5 pc.

Further acceleration of the electrons at the termination shock may be due to a Fermi-type process [Achterberg et al., 2001], where randomization of the particle momenta within the shock region produces a population of electron energies up to $\gtrsim 100$ TeV, capable of producing the inverse Compton radiation observed on Earth.

3.2.3 Pulsars with Supersonic Motion

Many pulsars have been found to be moving at great speeds, from 100 to 2,000 km/s from their place of birth. This is believed to be due to a pulsar "kick", which may be caused by an asymmetric supernova explosion This kick velocity acquired at birth is believed to be on average 450 ± 90 km/s, exceeding the escape velocity of binary systems, globular clusters and the Galaxy [Lyne and Lorimer, 1994]. If the pulsar is moving at very high velocity through the ISM, this will result in a ram pressure which may deform the termination shock, crushing it in the forward direction and forming a bow shock ahead of the termination shock. This scenario is shown in Figure 3.5 according to simulations carried out by Bucciantini [2002]. It is possible to calculate the velocity of the pulsar if the relative radii of the forward (r_{ts}^F) and backward (r_{ts}^B) shocks are known as

$$\frac{r_{ts}^F}{r_{ts}^B} = \gamma^{1/2} M$$

[van der Swaluw et al., 2003, Bucciantini, 2002] where M is the Mach number, defined as $v_{psr} = Mc_s$. c_s, the speed of sound, is given by $c_s^2 = \gamma p/\rho$, with p the pressure, ρ the density and γ the adiabatic constant of a monoatomic gas.

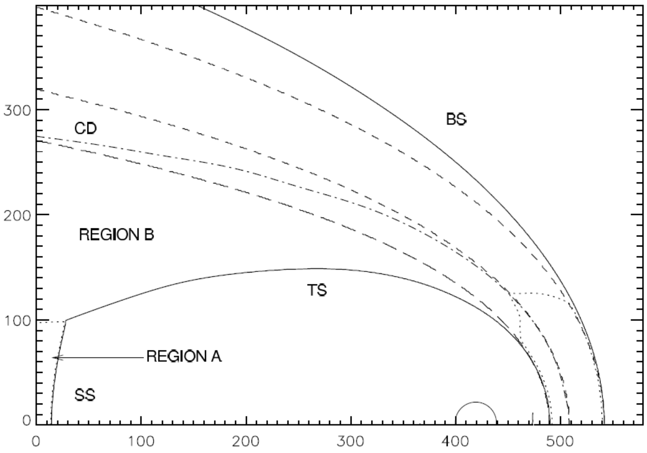

Figure 3.5: A simulation of the structure of the shock region of a a supersonic pulsar. TS is the termination shock, SS is the spherical shock, CD is the contact discontinuity (dotdashed line), BS is the bow shock. The short-dashed lines represent two analytic solutions, the long-dashed line is the analytic solution for the correct wind/environment ram pressure ratio, the dotted lines indicates the sonic surfaces (the subsonic region is in the head). The circle corresponds to the region in which the stellar wind values are fixed. Figure taken from Bucciantini [2002]

4 Unidentified H.E.S.S. Sources as Evolved PWNe

In 2004 H.E.S.S. discovered its first unidentified, or “dark” source, HESS J1303−631. i.e., a VHE Gamma-ray source without known counterparts at other wavelengths. Since then, over 20 unidentified sources have been discovered by H.E.S.S., nearly all of them extended and lying in the Galactic plane [Aharonian et al., 2008]. One possible explanation for such sources is that they represent *evolved* pulsar wind nebulae. As the nebula expands the magnetic field density is expected to drop causing a drop in synchrotron brightness. On the other hand, the Gamma-rays produced by inverse Compton scattering are independent of the ambient magnetic field and may continue emitting VHE Gamma-rays for thousands of years, until adiabatic losses and IC cooling take over. This process can produce “dark” pulsar wind nebulae.

4.1 Evolution of Pulsar Wind Nebulae

To better understand the dark sources discovered by H.E.S.S., a magneto-hydrodynamic model was constructed by de Jager et al. [2009] to simulate the time evolution of the synchrotron and inverse Compton brightness of a pulsar wind nebula (PWN). The model presented there is based on previous simulations of PWNe (e.g. van der Swaluw et al. [2001]) and provides (approximate) analytical solutions for PWN expansion using the Versatile Advection Code (VAC; `http://www.phys.uu.nl/~toth/`). The model and results of these simulations are summarized in this section.

Such evolution from high synchrotron toward synchrotron underluminous sources is confirmed experimentally by comparing the ratio of Gamma-ray to X-ray luminosity, L_γ/L_X, as a function of the characteristic age of the pulsars. The majority of the dark sources discovered by H.E.S.S. in recent years have energetic pulsars near the edge of the emission region and, as will be shown in the following section, more than chance coincidence would predict.

4.1.1 The Model

The simulations solve the Euler continuity equations for a non-relativistic, zero-viscosity fluid . The magnetic field is calculated by solving

$$\frac{\partial B}{\partial t} + \nabla \times (v \times B) = 0$$

Note that this is not a full MHD solution because the field is calculated kinematically from the flow and no backreaction of the fluid is considered. More detailed MHD calculations were done by e.g. van der Swaluw [2003]. The spin down luminosity of the pulsar as a function of time is assumed to be given by

$$L(t) = \frac{L_0}{(1+\frac{t}{\tau})^{n-1}}$$

where L_0 is the initial spin down power and τ is the spin down timescale, which, for a birth period of P_0 and present period P, is given by

$$\tau = \frac{2\pi^2 I}{P_0^2 L_0} = \frac{2\pi^2 I P_0^2}{P^4 L}$$

4.1.2 Electron Injection

Defining $N(E,t)$ as the time dependent differential particle spectrum for electrons ($e^{+/-}$) of energy $E = \gamma m_e c^2$, then the transport equation is given by

$$\frac{dN}{dt} + \frac{N}{\tau_{\mathrm{syn}}} + \frac{N}{\tau_{\mathrm{ad}}} = Q(t)$$

where τ_{syn} and τ_{ad} are the time scales corresponding to synchrotron and adiabatic losses respectively. τ_{syn} is, naturally, dependent on the time dependent magnetic field strength $B(t)$.

It has been seen in many cases (e.g. Gelfand et al. [2009]) that a two component electron spectrum is required to describe the synchrotron component of typical PWNe. These are sometimes interpreted as an older *colder* component and a younger *hotter* component. This model assumes a two component electron spectrum from the point of injection at the pulsar wind termination shock of the form

$$Q(E,t) = \begin{cases} Q_0(t)(E/E_b)^{-p_1} & \text{for } E < E_b \\ Q_0(t)(E/E_b)^{-p_2} & \text{for } E_b < E < E_{\max} \end{cases}$$

where E_b is the energy of the break point between the two spectra and $E_{\max}$ is the cut-off energy. A value of $p_1 \approx 1.0$ reproduces the typical flat radio spectra, while $p_2 \approx 2.0$ would reproduce the un-cooled spectral indices seen in X-rays.

4.1.3 Evolution Towards an Unidentified Gamma-ray Source

To illustrate this model, de Jager et al. [2009] took SNR G21.5−0.9 as an example and the time evolution of the leptonic spectrum and hence multi-wavelength intensity was followed over time. The central pulsar PSR J1833−1034 has a period of 61.8 ms and an age near 1 kyr as determined from the expansion of the SNR [Bietenholz and Bartel, 2008].

To reproduce the ratio of energy fluxes between X-rays and TeV, the average field strength was normalised to 25 μG at the present age near 1 kyr. ISO observations [Gallant and Tuffs, 1998] of the PWN show that the radio spectrum should break around 10^{12} Hz. This break is either intrinsic or due to radiation losses. It was found, however, that this break cannot be due to radiation losses since this would imply a too large Crab-like field strength, which cannot be reconciled with the observed ratio of TeV to X-ray flux. An intrinsic break at energy E_b to $p_2 = 2.6$ was found to best reproduce the post spectral break data.

The B field obtained from the simulations, as a function of time, is shown in Figure 4.1. It is found that, as the PWN expands, the magnetic field will decrease as $t^{-1.3}$. This falling magnetic field, then, explains the fall in synchrotron luminosity as depicted in Figure 4.2, whereas the inverse Compton component is found to be steady for much longer times, until cooling effects eventually extinguish the Gamma-ray emission as well. This model is currently the best description of the formation of "dark" or underluminous TeV sources.

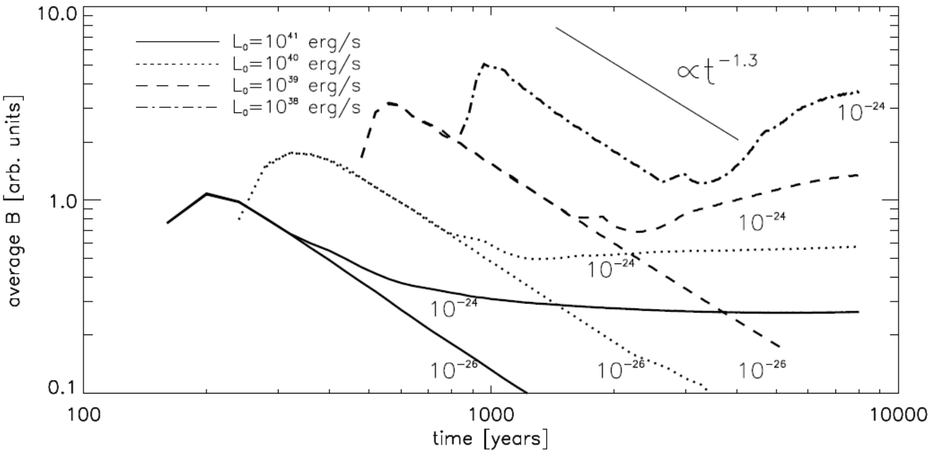

Figure 4.1: The evolution of the magnetic field in a PWN as it undergoes expansion. The simulations were performed using four starting spin-down luminosities ranging from $L_0 = 10^{38}$ to 10^{41} erg/s. The average magnetic field across the nebula is scaled to arbitrary units. After an initial rise, the magnetic field is found to fall as $\sim t^{-1.3}$. Figure taken from de Jager et al. [2009].

4.2 Evolution of Gamma-ray/X-ray Luminosities of PWNe

A search for a correlation between the ratio of the Gamma-ray luminosity, L_γ, and the X-ray luminosity, L_X, and the pulsar's spin down luminosity (or conversely, the pulsar's characteristic age) was carried out by Mattana et al. [2009]. As the pulsar wind nebula

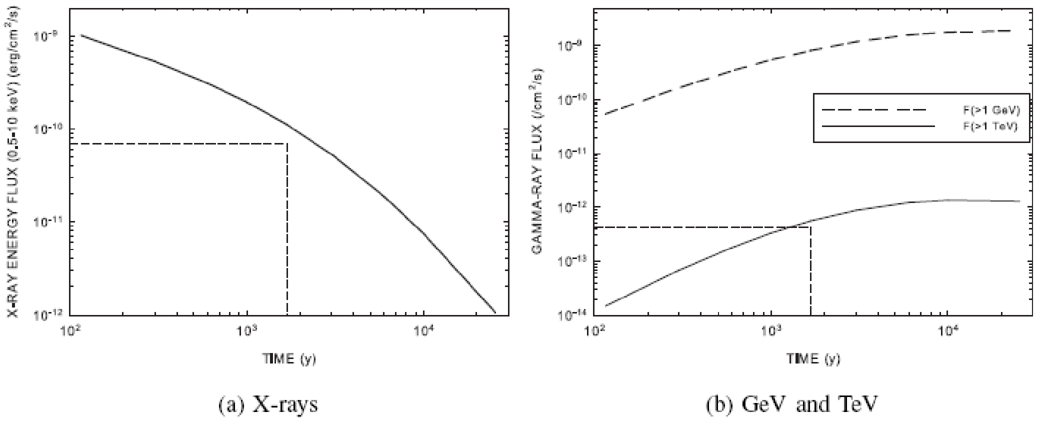

(a) X-rays (b) GeV and TeV

Figure 4.2: The evolution of the synchrotron (left) and inverse Compton emission (right) of a PWN over time. As the PWN undergoes expansion the magnetic field is expected to decrease resulting in a decrease of synchrotron brightness over time. The inverse Compton emission, however, does not depend on the magnetic field and may represent electrons accelerated over the life-time of the pulsar for pulsar ages less than some 10's of thousands of years (i.e. younger than the IC cooling timescale, $\gg 10^4$ yr). Figure taken from de Jager et al. [2009].

expands, the magnetic field is predicted to decay producing, over time, a dark TeV Gamma-ray source.

This study made use of eight Gamma-ray sources observed with H.E.S.S. known to be associated with pulsar wind nebulae, as well as six H.E.S.S. candidate pulsar wind nebulae with pulsars with $\tau_c < 100$ kyr and $\dot{E} > 10^{35}$ erg/s. As can be seen in Figure 4.3, a strong correlation (anti-correlation) was found between the L_γ/L_X ratio and the pulsars' spin down luminosity (characteristic age). This correlation is mainly due to the X-ray correlation, since, also shown in the figure, the Gamma-ray luminosity alone does not strongly correlate.

The Gamma-ray fluxes, F_γ, are integrated in the $1-30$ TeV energy band, while the X-ray fluxes, F_X, are integrated over the $2-10$ keV band. Fitting the entire data set yielded the following relations for the X-ray luminosity:

$$\log_{10} L_X = (33.8 \pm 0.04) + (1.87 \pm 0.04)\log_{10}\dot{E}_{37} \tag{4.1}$$

$$\log_{10} L_X = (33.7 \pm 0.04) - (2.49 \pm 0.06)\log_{10}\tau_c \tag{4.2}$$

where $\dot{E}_{37} = \dot{E}/10^{37}$ erg/s and τ_c is in years.

The best fit for the L_γ/L_X ratio resulted in:

$$\log_{10}F_\gamma/F_X = (0.57 \pm 0.04) - (1.88 \pm 0.05)\log_{10}\dot{E}_{37} \tag{4.3}$$
$$\log_{10}F_\gamma/F_X = (0.89 \pm 0.04) + (2.14 \pm 0.07)\log_{10}\tau_c \tag{4.4}$$

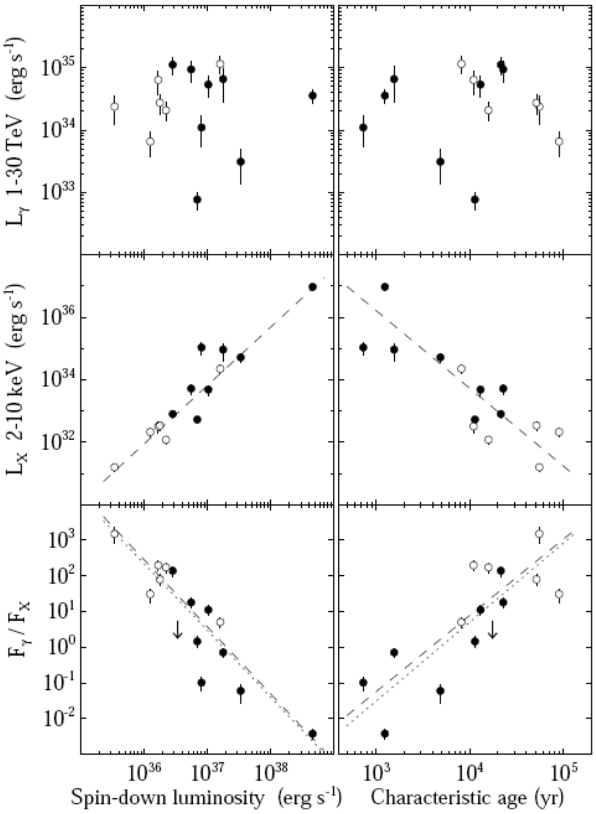

Figure 4.3: Gamma-ray luminosity, X-ray luminosity, and Gamma-ray to X-ray flux ratio versus pulsar spin-down luminosity, $\dot{E}$ (left column), and characteristic age, τ_c, (right column). Filled and open circles stand for identified and candidate PWNe, respectively. The upper-limit for the flux ratio of PSR B1706-44 (Aharonian et al. 2005a; Romani et al. 2005) is reported with an arrow. Also shown are the best-fit curves for identified PWNe (dotted lines), and for the whole sample (dashed lines). While there is no clear correlation found for the Gamma-ray luminosities, the X-ray luminosities do show a clear correlation with the spin-down luminosity and anti-correlation to the characteristic age. Figure taken from Mattana et al. [2009].

4.3 Population Studies

As mentioned before, a large number of H.E.S.S. unidentified sources have been found to lie adjacent to a high power pulsar ($E > 10^{34}$ erg/s). Yet, with nearly 2,000 pulsars now known in the sky, the possibility for a chance coincidence cannot excluded a priori.

In order to explore this possibility, Carrigan et al. [2008] considered the distribution of pulsars from the Parkes Multibeam Pulsar Survey (PMPS, Hobbs et al. [2004]) relative to H.E.S.S. TeV Gamma-ray sources having a detection significance of at least 5σ. The search was performed using data from the H.E.S.S. Galactic plane survey, including an extension of the survey to Galactic longitudes $-60° < l < -30°$, dedicated observations of Galactic targets and re-observations of H.E.S.S. survey sources.

To be detectable by H.E.S.S., a source at distance d must exhibit a Gamma-ray luminosity in the 1 TeV to 10 TeV range of $L \gtrsim 10^{32}/d^2$ erg s^{-1} kpc^{-2}. Assuming a conversion efficiency of 1% of pulsar spin-down energy loss, $\dot{E}$, into TeV Gamma-rays, PWNe powered by pulsars with $\dot{E}$ around $10^{34}/d^2$ erg s^{-1} kpc^{-2} can be expected to be detectable.

Pulsars from PMPS meeting the above criteria, and within the H.E.S.S. survey region were considered, making a total of 435 pulsars. Of the 435 pulsars, 30 were found to be coincident with significant Gamma-ray emission at or near the pulsar location (Figure 4.4, top left panel). The lower left panel of Figure 4.4 shows the fraction of pulsars with coincident Gamma-ray emission for different values of the ratio $\dot{E}/d^2$. The fraction was found to be about 5% for pulsars with spin down flux below 10^{33} erg s^{-1} kpc^{-2} and increases to about 7% for pulsars with $\dot{E}/d^2$ above 10^{35} erg s^{-1} kpc^{-2} (see Figure 4.4).

Some of these associations could, of course, be coincidental. The rate of chance coincidences was estimated by simulating 10^6 samples of random independent pulsar distributions (each consisting on average of 435 "pulsars") following the distribution in longitude and latitude of the PMPS pulsars and taking into account the narrowing of the distribution in latitude with increasing spin-down flux. The expected fraction of chance coincidences is shown as dark shaded areas in Figure 4.4 and ranges from 4% to 12%. All associations with pulsars with $\dot{E}/d^2 < 10^{33}$ erg s^{-1} kpc^{-2} are, within statistical errors, consistent with chance coincidences. Indeed for plausible values of the ratio between the Gamma-ray luminosity and the pulsar spin down energy loss, $L_\gamma/\dot{E}$, no detectable emission would be expected from such pulsars.

On the other hand, the detection of emission from high spin-down pulsars was found to be statistically significant. The probability that the detection of VHE sources coincident with 9 or more of the total of 23 pulsars above $\dot{E}/d^2 > 10^{34}$ erg s^{-1} kpc^{-2} results from a statistical fluctuation was found to be $\sim 3.4 \times 10^{-4}$. For detection of 5 or more of the total of 7 pulsars above 10^{35} erg s^{-1} kpc^{-2}, the chance probability is $\sim 4.2 \times 10^{-4}$.

The results of these studies, shown in Figure 4.4, demonstrate that a large fraction of high luminosity pulsars correlate with sources of VHE Gamma-rays, emitting with a Gamma-ray luminosity of order 1% of the pulsar spin down power. This correlation does not necessarily imply that the pulsar or PWN itself is responsible for the Gamma-ray flux. Such a correlation could also result from some other process related to the pulsar or its creation, such as a supernova shock wave. The correlation found between Gamma-ray detectability and spin down flux $\dot{E}/d^2$ argues in favour of a pulsar related origin of the Gamma-ray signal.

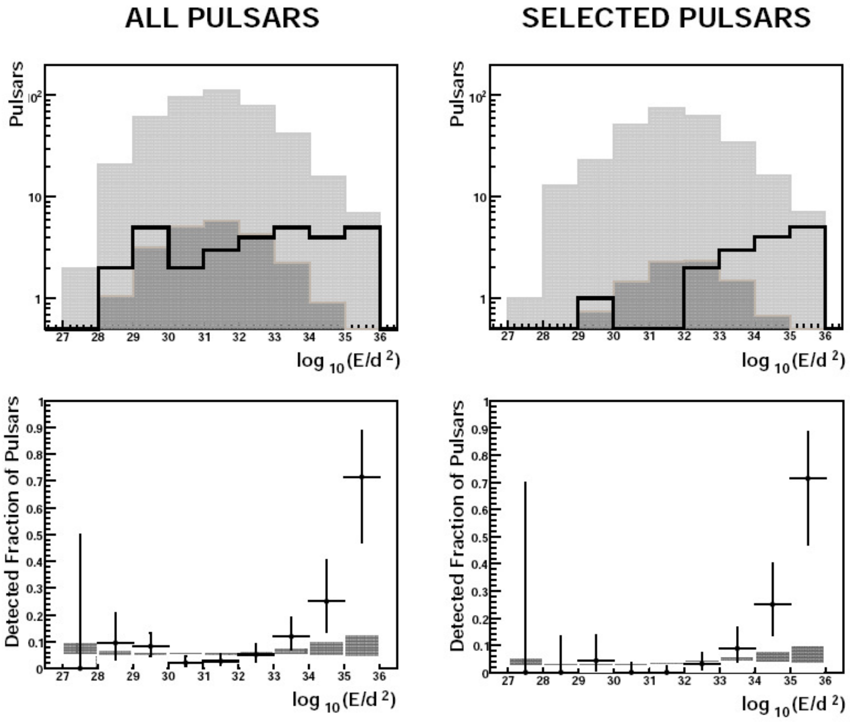
ALL PULSARS

SELECTED PULSARS

Figure 4.4: Top row: Distribution in $\log_{10}(\dot{E}/d^2)$ of all PMPS pulsars in the H.E.S.S. scan range (shaded in light grey), of chance coincidences (shaded in dark grey) and of detected pulsars (black line). Here, $\dot{E}/d^2$ is measured in erg s^{-1} kpc^{-2}. Bottom row: The points show the fraction of pulsars coincident with significant Gamma-ray excess, as a function of $\log_{10}(\dot{E}/d^2)$. The shaded band represents the probability for a chance coincidence. The width of the band accounts for the uncertainty in the width of the latitude distribution of pulsars. Left: all pulsars; right: double occurrences of Gamma-ray sources removed by omitting pulsars which overlap with stronger pulsars or known non-pulsar sources. Figure taken from Carrigan et al. [2008].

5 The Unidentified VHE Gamma-ray Source, HESS J1303−631

In recent years, nearly a hundred new VHE Gamma-ray sources of various types have been discovered by IACTs. The most abundant type of Galactic VHE Gamma-ray sources appears to be PWNe associated to energetic pulsars. These are thought to be powered by a relativistic particle outflow of electrons and positrons from the pulsar.

Most of the TeV Gamma-ray sources discovered to date also exhibit radio and X-ray radiation. The discovery of TeV 2032+4131 by the HEGRA collaboration in 2002 [Aharonian et al., 2002] lead to a new class of extended VHE Gamma-ray sources lying in the Galactic Plane and without obvious counterparts at other wavelengths. Dozens more of these so called “dark sources” were discovered by the H.E.S.S. collaboration in the following years [Tibolla et al., 2009]. Identifying and understanding this new class of sources has become an important task for modern Gamma-ray astronomy.

A growing number of extended very high-energy (VHE, $E_\gamma > 100$ GeV) Gamma-ray sources, either without extended X-ray/radio counterparts or with significantly less extended counterparts, appear to be associated with energetic pulsars in the Galactic Plane. Some recent examples of this class of object include HESS J1809-193, HESS J1912+101, HESS J1356-645 [Renaud et al., 2008], MSH-15-52 [Aharonian et al., 2005b], Vela X [Aharonian et al., 2006c], the two sources in the Kookaburra region, HESS J1420-607 and HESS J1418-609 [Aharonian et al., 2006g], and HESS J1825-137 [Aharonian et al., 2006f].

These associations are believed to represent pulsar wind nebulae (PWNe), which are thought to be powered by a relativistic particle outflow of electrons (and positrons) from a central rapidly rotating neutron star (pulsar) left behind after a Supernova event. Many of these PWN associations form what are known as *Offset PWN* where the pulsar is located at or near the edge of the Gamma-ray and X-ray emission region(s). These configurations may form in two ways: 1) a high spatial velocity pulsar, (possibly supersonic in which case a bow shock nebula may form), leaves behind a “trail” of high energy electrons in the Inter Stellar Medium (ISM), or 2) due to inhomogeneous ISM densities, expansion of the SNR proceeds asymmetrically or 3) the expanding PWN may be disrupted by the reverse shock of the SNR, a scenario known as a *Crushed PWN* [van der Swaluw et al., 2001].

5.1 Serendipitous Discovery of the Unidentified HESS J1303-631

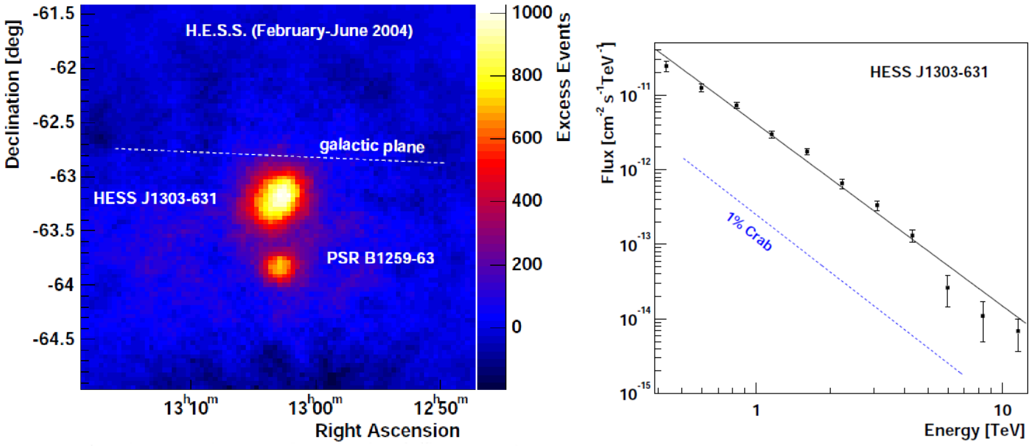

Figure 5.1: The serendipitous discovery of HESS J1303−631.
Left: the excess map showing two sources, the southern point-like source associated to PSR B1259−63, and ∼ 0.6° to the North, the unidentified HESS J1303−631.
Right: the spectrum extracted for the source, HESS J1303−631.
Both figures taken from Aharonian et al. [2005c].

The VHE Gamma-ray source HESS J1303−631 was serendipitously discovered in 2004 [Aharonian et al., 2005c] with the H.E.S.S. array during observations of the pulsar PSR B1259−63 [Aharonian et al., 2009]. Figure 5.1, left, shows the smoothed excess Gamma-ray like events with the extended HESS J1303−631 lying ∼ 0.6° to the North of the point-like source PSR B1259−63. On the right is the obtained spectrum of the source fitted with a power-law function. HESS J1303−631 was the first “dark” source discovered by H.E.S.S., having a large Gaussian source extension of ∼ 0.18° and a flux of ∼ 15% of the Crab flux, but originally no known extended counterparts in other wavelengths. A search in the field of view yielded only one pulsar with a high enough spin-down luminosity to account for the Gamma-ray emission, PSR J1301−6305, located at the North-Western edge of the emission region of the H.E.S.S. source (see Table 5.1 for a list of known pulsars in the direction of HESS J1303−631). The VHE Gamma-ray source was found to represent 1.8% of the pulsar’s current spin-down luminosity, assuming a pulsar distance of 6.6 kpc (based on NE2001 Cordes and Lazio [2002]), well within standard values for PWNe. Also, Beilicke [2005] found evidence at the $2\,\sigma$ level for a shift in the center of the emission region roughly in the direction of the pulsar as a function of energy by looking at the excess distributions in the energy bands $E < 900\,$GeV, $900\,\text{GeV} < E < 3\,$TeV and $E > 3\,$TeV.

5.1.1 Initial Searchs for Counterparts in other Wavelengths

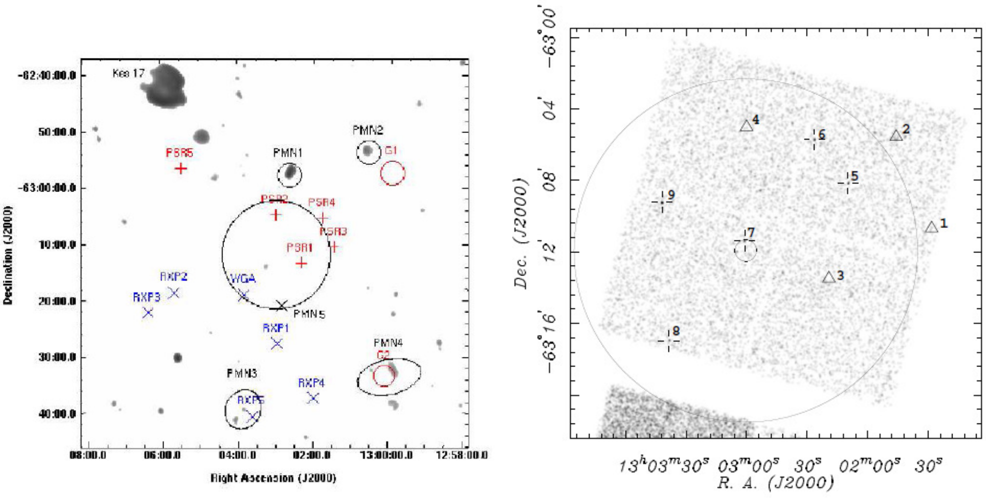

Figure 5.2: Left: 843 MHz SUMSS radio map of the region around HESS J1303−631 (marked as the large circle of radius 0.16°). Also marked are the positions of the X-ray sources (WGA and RXP1-5) as well as the radio sources (PMN1-5, G1 and G2 for H II regions and PSR1-5 for pulsars). Circles or ellipses surrounding individual sources indicate the catalogued source extension (convolved with the relevant radio beam size, taken from Aharonian et al. [2005c]).
Right: Chandra ACIS-I image of the field of view of HESS J1303−631. The numbered triangles mark the locations of radio pulsars from the Parkes Multibeam Survey. The small circle corresponds to the $1\,\sigma$ uncertainty of the centroid of HESS J1303−631, and includes both statistical errors and pointing (systematic) errors. The large circle is the estimated Gaussian $1\,\sigma$ extent of the TeV emission. The plus signs mark the significant Chandra point sources.

A Chandra X-ray observation (Figure 5.2, right), partially covering the VHE peak emission region [Mukherjee and Halpern, 2005], revealed several point sources within the field of view, but no extended emission corresponding to the Gamma-ray emission region was found, and none of the radio pulsars in the region were detected. Additionally, a radio survey, Sydney University Molonglo Sky Survey (SUMSS), at 843 MHz which covered the region of HESS J1303−631 also revealed no obvious extended radio counterparts (Figure 5.2, left). There are, however, 5 radio pulsars located near the TeV Gamma-ray emission region (Table 5.1), the most energetic of which, PSR J1301−6305, provides the best candidate for an association to the H.E.S.S. source. This pulsar and its energetics will be discussed in further sections.

5.1.2 Proposed Explanations of the VHE Gamma-ray Source

The initial discovery of such a large, intense source of VHE Gamma-rays, but without known counterparts at other wavelengths was quite surprising. This discovery prompted the development of several theoretical attempts to provide a framework for understanding such "dark" sources, ranging from dark matter annihilations to Gamma-ray burst remnants. An overview of the proposed explanations is presented here, as well as results of attempts to confirm or refudiate them when possible.

Clump of Annihilating Dark Matter

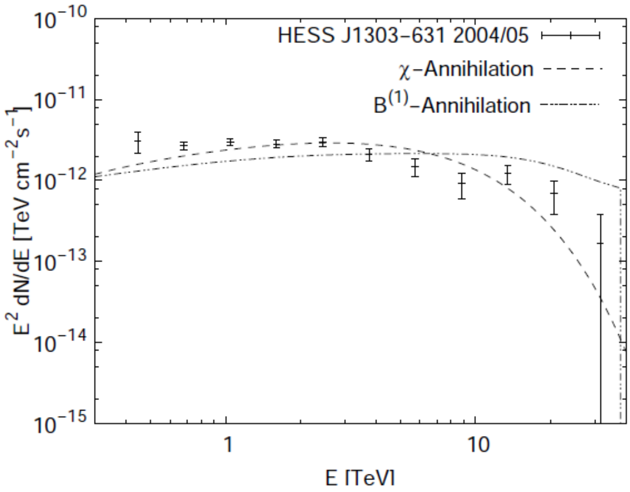

Figure 5.3: The spectral energy distribution $E^2 dN/dE$ of HESS J1303−631 fitted to spectral predictions for Neutralino (χ) as well as Kaluza-Klein particle ($\mathrm{B}^{(1)}$) annihilations. A large particle mass of $\sim$ 40 TeV would be required for both types of particles. Figure taken from Ripken et al. [2008].

If the Dark Matter in the Galactic halo is sufficiently cold, it is expected to form small scale structures known as clumps. If the dark matter particles can self annihilate, as predicted for many dark matter particle candidates, then these clumps may be expected to produce a Gamma-ray signal detectable in the GeV or TeV bands. Furthermore, the signature of such an annihilation process is expected to be X-ray and radio quiet, consistent with the original discovery of HESS J1303−631. To investigate this scenario, Ripken et al. [2008] compared the spectral energy distribution of HESS J1303−631 with dark matter annihilation expected for the Neutralino (χ) [Bertone et al., 2005] and the Kaluza-Klein particle ($\mathrm{B}^{(1)}$) [Servant and Tait, 2003]. It was found that the annihilation models described the spectrum very poorly, see Figure 5.3, and required an unreasonably high particle mass, $\sim$ 40 TeV. This explanation was therefore deemed unlikely to be able to account for HESS J1303−631.

Photodisintegration

Anchordoqui et al. [2007a] suggested that at least some of the unidentified TeV Gamma-ray sources could be explained by a process known as photodisintegration, after Aharonian et al. [2006e] noted that at least two unidentified sources lie in the direction of OB stellar associations, namely HESS J1303−631 and TeV J2032+4130, discovered in the directions of the OB associations Centaurus OB1 (18 B stars, 1 O star) and Cygnus OB2 (several thousand stars) respectively. The process of Gamma-ray production through photodisintegration was described by Anchordoqui et al. [2007b] and was shown to be capable of producing a dark source under certain ideal conditions.

The photodisintegration hypothesis of Gamma-ray production posits that Gamma-rays may be produced from high energy nuclei, or heavy hadronic cosmic-rays, such as iron nuclei, through interaction with background photons, which may stem either from the cosmic microwave background (CMB) or photons from star light, through the nuclear giant dipole resonance (GDR). Since OB associations provide not only abundant starlight, but may also provide strong winds which could accelerate cosmic-rays at a shock region, they present the most likely candidate for observing this process.

The nuclear giant dipole resonance occurs at an energy of $\epsilon_\gamma^{GDR} \sim 10 - 30$ MeV in the nuclear rest frame. Thus, for a nucleus of atomic mass number, A, with an energy $E_A^{LAB} = \Gamma_A A m_N$, where m_N is the mass of a nucleon, and Γ_A the Lorentz factor, the energy of the required ambient photon for nuclear excitation would then be $\epsilon = \epsilon_\gamma^{GDR}/\Gamma_A$ in the lab frame. The GDR decays by the statistical emission of a single nucleon, leaving an excited daughter nucleus $(A-1)^*$ which in turn de-excites through emission of one or more photons of energy $\epsilon_\gamma^{dxn} \sim 1{-}5$ MeV in the rest frame of the nucleus. The probability for emission of two (or more) nucleons by the GDR excited nucleus is smaller by an order of magnitude and left out of further consideration.

The energy of the Gamma-ray emitted by the daughter particle in the lab frame is then $\epsilon_\gamma^{LAB} = \Gamma_A \epsilon_\gamma^{dxn}$, which, for a boost factor of $\Gamma > 10^6$ will produce a Gamma-ray in the TeV band, capable of being detected by modern IACTs if the flux is sufficiently high. Conversely, the energy of the ambient photon which excites the nuclear resonance for $\Gamma_A \sim 10^6$ is $\epsilon = \epsilon_\gamma^{\mathrm{GDR}}/\Gamma_A \sim 1$ eV, an energy which can easily be provided by starlight. As has been shown, the boost factor of the original cosmic-ray plays two roles: first, it brings the starlight up to an energy capable of exciting the GDR, and secondly, it boosts the emitted photon from daughter de-excitation up to TeV energies, the reason this process may also be referred to as *double boost Gamma-ray production.*

For the particular case of HESS J1303−631, lying in the OB association Centarus OB1, the local stars are well known, so it is possible to calculate the amount and distribution of ambient light, and therefore, the flux in cosmic-rays required to explain the observed Gamma-ray flux. A simulation of the ambient photon density was then carried out, taking the known star positions but assuming all stars lie in a plane at the nominal distance to the association of 2.2 kpc, an idealization which should increase the resulting photon density. The calculated photon distribution is shown in Figure 5.4 for the star distribution relative to the position of HESS J1303−631. It is clearly seen that the H.E.S.S.

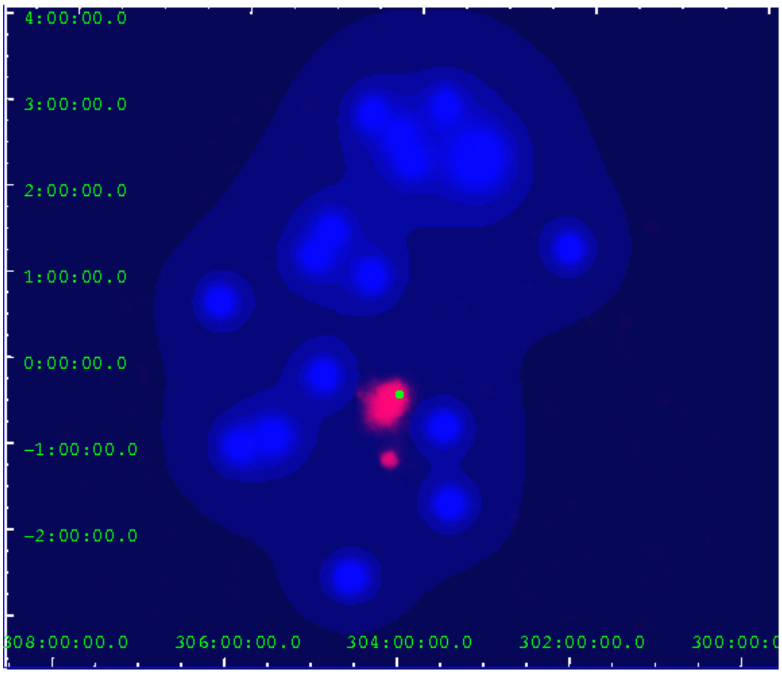

Figure 5.4: The location of HESS J1303−631 within the Centarus OB1 star cluster in Galactic coordinates. The blue scale indicates the photon intensity from the stars assuming a 2 dimensional distribution at the nominal distance to the association of 2.2 kpc. The red scale shows the H.E.S.S. significance, the larger feature being HESS J1303−631 and the smaller feature being PSR B1259−63. The green dot indicates the position of the pulsar PSR J1301−6305.

source does not coincide with the location of highest photon intensity. Furthermore, the star nearest to the H.E.S.S. source is a B star (far less intense than O stars) and is at a distance of $\sim$ 38 pc from the H.E.S.S. excess. This, together with the displayed light intensity and the very low number of stars in the association, may be enough to conclude that photodisintegration cannot explain the source. However, some simple calculations may make it more clear.

The B stars in the association were assumed to have a temperature of 20,000 K and the O stars to have a temperature of 45,000 K. The blackbody spectra of the stars are then found to peak at $\sim$ 5 eV and $\sim$ 12 eV respectively. For simplicity, the conservative assumption that all of the energy emitted by the stars is at the energy of 5 eV can be made. The intensity of light at the position of HESS J1303−631 is then found to be $\phi \sim 4.1 \times 10^{45}$ eV/s/pc^{-2} or a photon density of $n_{\gamma 5\mathrm{eV}} = 5.3 \times 10^{52}/\mathrm{pc}^3$.

Consider then a source of iron nuclei, $A = 56$, cosmic-rays. Following the results of Anchordoqui et al. [2007a] and Anchordoqui et al. [2007b], the mean free path of a cosmic-ray is given by

$$\frac{1}{\lambda_A} = \frac{\pi \sigma^{GDR} \epsilon_\gamma^{GDR} \Gamma^{GDR} n_\gamma}{4\Gamma_A^2 (5\text{eV})^2} \tag{5.1}$$

with $\Gamma^{GDR} = 8$ MeV, $\epsilon_\gamma^{GDR} = 42.65A^{-0.21}$ and the GDR cross-section, $\sigma^{GDR} = 1.45A \times 10^{-27}$ cm^{-2}. For the case of HESS J1303−631, this gives a mean free path of $\lambda_A \sim 7.7 \times 10^9$ pc, which is comparable to the size of the observable universe ($\sim 2.85 \times 10^{10}$ pc), or, conversely, this would require a flux of cosmic-ray iron nuclei of $\Phi_{\text{Fe}}(E > 8.7 \times 10^{16}\text{eV}) = 5.8 \times 10^3$ cm^{-2} s^{-1}. This is more than ten orders of magnitude larger than the flux of cosmic-rays at Earth and shows that the process of photodisintegration is not able to explain the observed TeV flux, at least for the case of HESS J1303−631.

Gamma-ray Burst Remnant

Atoyan et al. [2006] performed detailed calculations of particle diffusion, interaction, and radiation processes, and concluded that there was strong evidence for the identification of HESS J1303−631 as a Gamma-ray Burst (GRB) remnant within our Galaxy. It is believed that GRBs are caused by highly relativistic outflows with bulk Lorentz factors $\Gamma \gtrsim 100$, possibly from neutron star mergers. So far, GRBs have only been identified at cosmological distances. However, it was found there that the estimated rate of GRBs in the Galaxy would imply a likelihood of one to several GRBs in the Galaxy in recent ($\lesssim 10^4$ yr) times.

The model presented there predicts spectral and spatial signatures that would distinguish GRB remnants from ordinary supernova remnants, including: (1) large energy budgets inferred from their TeV emission, but at the same time (2) suppressed fluxes in the radio through GeV wavebands; (3) extended center-filled emission with an energy-dependent spatial profile; and (4) a possible elongation in the direction of the past pair of GRB jets.

While these predictions are in general consistent with what was already known about HESS J1303−631 at the time of discovery, it will be shown later that there is now good evidence to reject this hypothesis based on the determination of morphological properties as well as identification of an X-ray counterpart.

"Dark" Pulsar Wind Nebula

As shown in previous sections, nearly all attempts to explain the H.E.S.S. source, HESS J1303−631, have proven unsatisfactory. The spectrum and radial distribution of events show that the interpretation as a clump of annihilating dark matter is very unlikely, photodisintegration in the sparsely populated stellar association, Centaurus OB1, is not enough to account for the observed excess. The only two remaining plausible theories are then the interpretation as a Gamma-ray Burst Remnant or as "dark" or underluminous pulsar wind nebula. The key to discerning between these two possibilities would be either the detection of energy dependent morpholgy, which may indicate the origin of the high energy emission, or the detection of associated emission at other wavelengths. The following section reports on follow-up observations performed by H.E.S.S. in VHE Gamma-rays, as well as a deep observation by XMM-Newton in the X-ray regime in an attempt to identify this intriguing source and understand its emission mechanisms.

5.2 Follow-up Observations by H.E.S.S.

HESS J1303−631 was originally discovered during observations of PSR B1259−63 [Aharonian et al., 2005c]. Some of these early observations were made with telescope pointings coincident with the HESS J1303−631 emission region, rendering them unsuitable for spectral analysis for HESS J1303−631. Follow-up observations of the two sources between 2004 and 2008 led to a total data set of of 108.3 hours of live time, using only observations which passed standard H.E.S.S. data quality selection which rejects observations taken during periods of bad weather or with instrumental irregularities.

The data was taken in wobble offset mode at an average zenith angle of 61°, with an RMS of about 1.4°. The high zenith angle distribution of the observations raises the low energy threshold but also provides for slightly increased sensitivity at high energies due to the larger volume of atmosphere in the direction of observation used as a de facto calorimeter.

5.2.1 Data Analysis

The data was analyzed using the H.E.S.S. standard Hillas reconstruction [Aharonian et al., 2006d], in which each shower is characterized using Hillas parameters [Hillas, 1985] to determine shower energy and direction, and cuts are applied to the shower image parameters to minimize background, primarily due to cosmic ray protons. For the morphology studies, hard cuts were applied to reduce background contamination and improve image reconstruction (and hence the Point Spread Function of the instrument), with the Ring Background method to account for possible gradients in the background in the FOV, while standard cuts were used with the Reflected-Region Background method [Berge et al., 2007] for spectral and lightcurve extraction to lower the detection energy threshold. Cross-checks were performed using the TMVA multi-variant analysis [Ohm et al., 2009] leading to compatible results.

5.2.2 VHE Gamma-ray Excess

The source excess map (Figure 5.5) was fitted with a two dimensional asymmetric Gaussian function. This resulted in a fit position of $\alpha = 13^{\mathrm{h}}02^{\mathrm{m}}48^{\mathrm{s}} \pm 3^{\mathrm{s}}$, $\delta = -63°10'39'' \pm 24''$ and minor axis Gaussian width $\sigma_y = 0.145° \pm 0.006°$, major axis Gaussian width $\sigma_x = 0.194° \pm 0.008°$, and position angle, measured from North to East, of $\phi = 147° \pm 6°$. The fit χ^2/NDF was (389.8 / 391) The fitted position is consistent with the original discovery paper within 2 σ. The slight relative shift of the peak in the direction of the

Pulsar	$\dot{E}/10^{30}$ erg/s	$\delta_{10\mathrm{TeV}}$ [arc min]
PSR J1301−6305	1,700,000	3.1
PSR J1301−6310	6,800	6.6
PSR J1305−6256	760	24.2
PSR J1302−6313	270	7.2
PSR J1303−6305	6.8	5.6

Table 5.1: The known pulsars in the field of view of HESS J1303−631. $\delta_{10\mathrm{TeV}}$ is the distance from the given pulsar to the $E > 10$ TeV peak position.

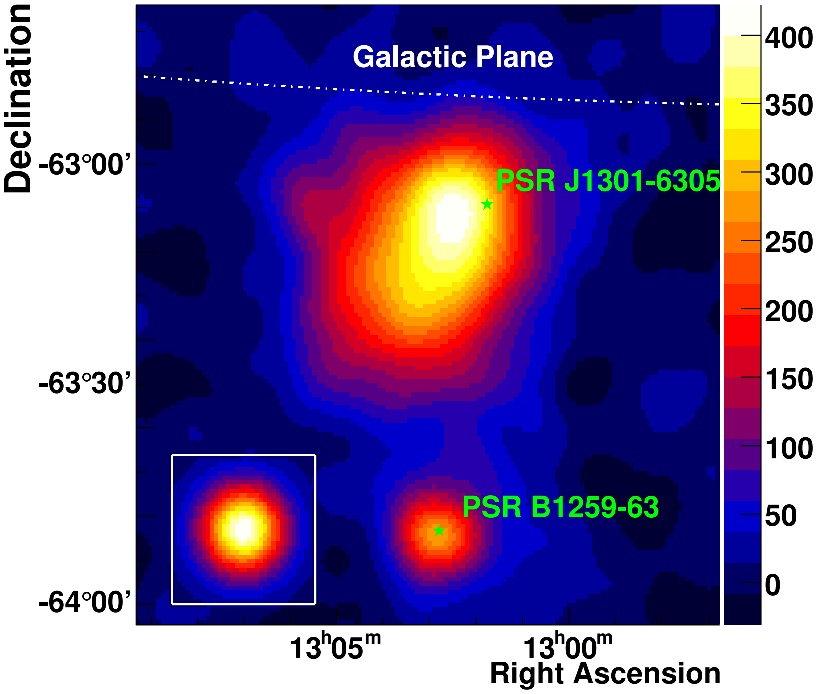

Figure 5.5: HESS J1303−631 field of view. The excess map was smoothed with a Gaussian of width $\sigma = 0.05°$. The variable point source, associated to the pulsar PSR B1259−63, is shown in the South. The high spin-down power pulsar PSR J1301−6305 is indicated with a green star on the North-West edge of the HESS J1303−631 emission region ($\sim 0.18°$ Gaussian width). The cut out in the bottom left shows the size of the PSF. The color transition between blue and red is set to occur at $\sim 5\sigma$.

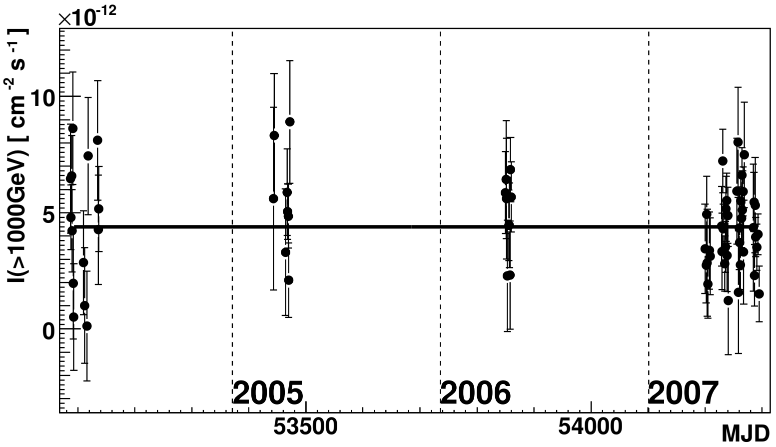

Figure 5.6: HESS J1303−631 nightly flux from observations taken from 2004 to 2007. The black line shows a fit of a constant to the data points, which is consistent with constant emission with χ^2 / ndf = 77 / 69, or 25% probability. The vertical dashed lines indicate the January 1st epoch of the indicated years.

pulsar for this work is due to the use of hard cuts (which increases the low energy threshold) and in the case of energy dependent morphology, to be demonstrated later, this will shift the fitted source position. The use of standard cuts yielded a source position which agreed with the discovery paper within $1\,\sigma$ errors.

Figure 5.6 shows the nightly flux measurements for the period of data taking, 2004 - 2007. An extraction region of 0.6° was used, to ensure inclusion of the whole source, centered on the fit position given above. The nightly flux was then fitted to a constant. No significant change in flux was observed over the entire observation period and the flux is consistent with constant emission, with a constant fit probability of 25%, consistent with expectations for large extended sources.

5.2.3 Energy Dependent Morphology

To test for the presence of energy-dependent morphology in the VHE source, slices on the uncorrelated excess maps in the following energy bands were compared: $E_1 = (0.84$ - $2)$ TeV, $E_2 = (2$ - $10)$ TeV and $E_3 > 10$ TeV. (Figure 5.7, left). The slices have dimensions $1.0° \times 0.1°$ and are centered at the best fit position of the TeV excess and the orientation is chosen along the fitted position angle (see Section 5.2.2). A Gaussian function was then fitted to each slice as shown in Figure 5.7 (right). The excess maps were also overlaid for a three-color image (Figure 5.23).

The parameters of the resulting Gaussian fits for each energy band (Table 5.2) were then plotted as a function of energy (Figure 5.8). A fit of a constant to these parameters yielded very bad quality fits (Table 5.3), which establishes the existence of strong energy-

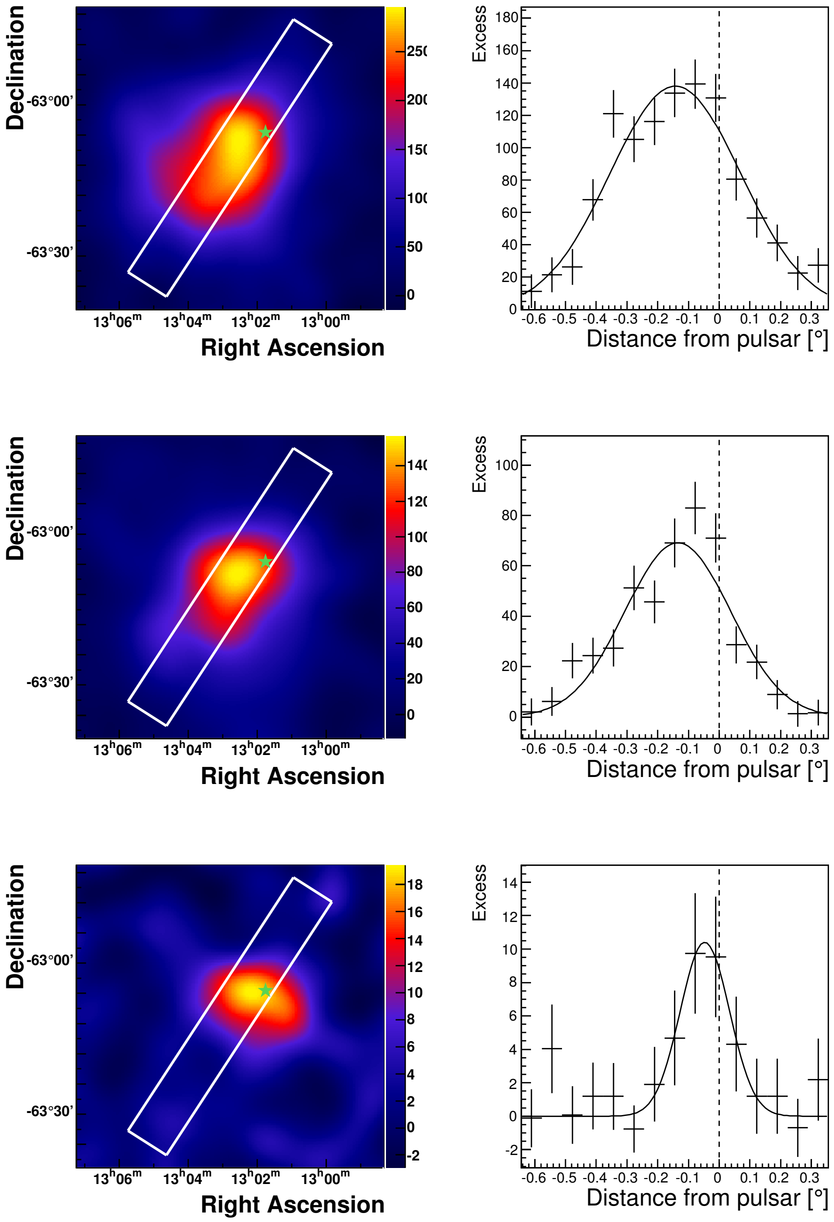

Figure 5.7: Left: energy-dependent excess maps of the HESS J1303−631 region in the energy bands $E_1 = (0.84 - 2)$ TeV, $E_2 = (2 - 10)$ TeV and $E_3 > 10$ TeV. Slices are indicated by the rectangles, taken in the direction of the semi-major axis of the fitted asymmetric Gaussian function. Right: the slices are then fitted with a Gaussian function. The pulsar position is marked by a green star in the sky maps and a dashed line in the profiles.

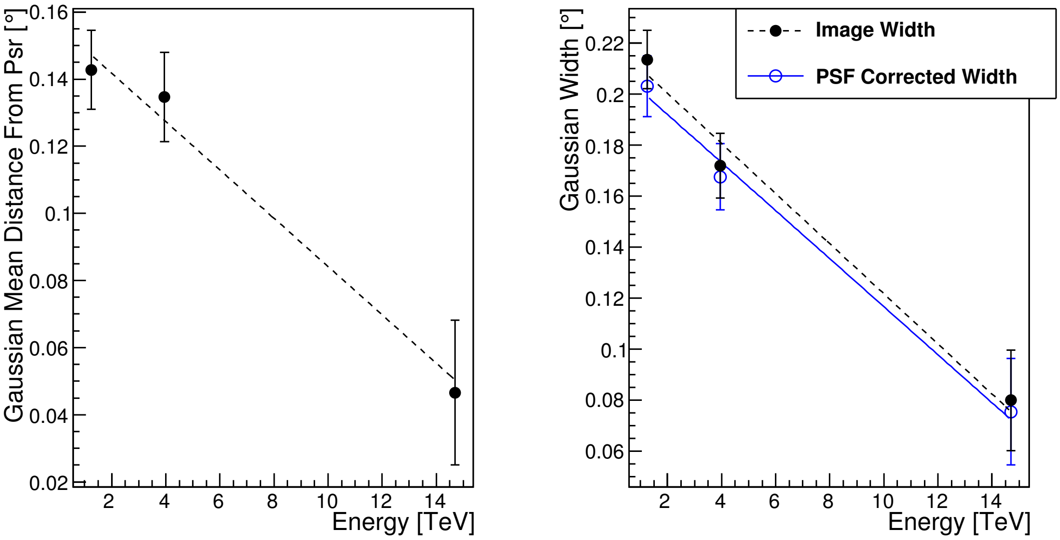

Figure 5.8: Left: HESS J1303−631 fitted Gaussian mean, $c(E)$, measured from the pulsar position, as a function of energy. Right: the PSF corrected intrinsic Gaussian extension ($w_{\text{int}}(E)$, blue) is overlaid with the image Gaussian extension ($w_{\text{img}}(E)$, black dashed) as a function of energy. The points are chosen to correspond to the average energy in the respective energy bins.

dependent morphology. Fitting a linear function yielded much better quality fits and a model of the morphology parameterized by a projected center of emission, $c(E)$ and the PSF corrected Gaussian intrinsic width, $w_{\text{int}}(E)$:

$$c = (0.157 \pm 0.012)^\circ - (0.006 \pm 0.002)^\circ \times E_{\text{TeV}}$$
$$w_{\text{int}} = (0.215 \pm 0.012)^\circ - (0.009 \pm 0.002)^\circ \times E_{\text{TeV}}$$

This model is presumed valid for $E < 24$ TeV, beyond which point the intrinsic width becomes negative and the model takes the form of a point source thereafter. Also, the position of the Gamma-ray peak in the model is constrained not to move beyond the pulsar position.

5.2.4 Gamma-ray Spectrum

The spectrum (Fig 5.9) was derived using the Region Background Method [Berge et al., 2007] with an integration region of radius 0.6°, more than three times the intrinsic Gaussian extension to avoid effects of energy dependent morphology, centered at the nominal source position of $\alpha = 13^{\text{h}}03^{\text{m}}0^{\text{s}}.4$ and $\delta = -63^\circ 11' 55''$. Standard cuts were applied to decrease the energy threshold. The derived spectrum for the entire data set, excluding

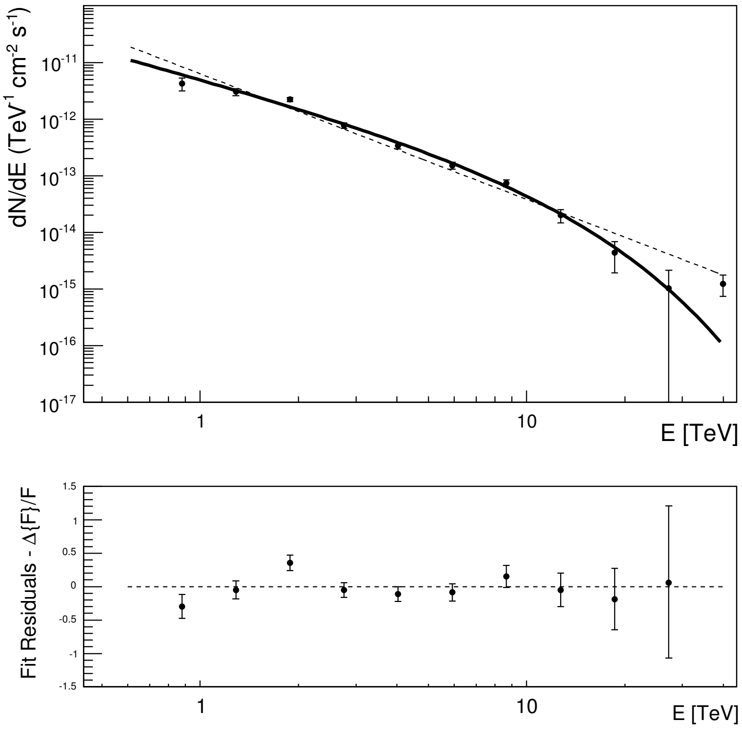

Figure 5.9: HESS J1303−631 spectrum produced using a 0.6° integration region. The spectrum is fit with a power-law function with spectral index 1.5 ± 0.2 with a fitted cutoff energy of $E_{\mathrm{cut}} = (7.7 \pm 2.2)$ TeV. The fit resulted in a χ^2/NDF of (20 / 8) or 1% probability. The dashed line shows the power-law spectrum which describes the data poorly.

observations with offset less than 0.5°, is shown in Figure 5.9. The spectrum was fitted with a power-law function $dN/dE = N_0(E/1\mathrm{TeV})^{-\Gamma}$ with a resulting photon index of $\Gamma = 2.44 \pm 0.03$ and normalization constant $N_0 = (5.9 \pm 0.25) \times 10^{-12}\ \ \mathrm{TeV}^{-1}\mathrm{cm}^{-2}\mathrm{s}^{-1}$, which is consistent with the original discovery, however, with the inclusion of the additional data taken since the source discovery, the fit probability was unsatisfactory. A fit to a power-law with a cutoff at the energy E_{cut},

$$\frac{dN}{dE} = N_0 E^{-\Gamma} e^{-E/E_{\mathrm{cut}}},$$

yielded a better fit probability of 1%, with fitted parameters

$$\begin{aligned} N_0 &= (5.6 \pm 0.5) \times 10^{-12}\ \mathrm{TeV}^{-1}\mathrm{cm}^{-2}\mathrm{s}^{-1} \\ \Gamma &= 1.5 \pm 0.2 \\ E_{\mathrm{cut}} &= 7.7 \pm 2.2\ \mathrm{TeV} \end{aligned}$$

The large size of this integration region allows the placement of only two reflected *off-regions* for the background determination. In a cross-check analysis to search for systematic effects of the size of the integration region, a similar analysis with integration region of 0.22° radius was performed. Because of the large intrinsic Gaussian extension of this source, a large number of events fall outside of this integration region. In order to correct for this effect, estimates of the flux corrections were made based on the model of the morphology of the source image developed in the previous section. This model was applied to make an energy dependent effective area correction to the measured spectrum, accounting for events falling outside of the integration region on a spectral energy bin-by-bin basis.

The spectrum derived in this way was found to be consistent with the spectrum obtained with the larger integration region of 0.6° radius. The spectrum obtained from the larger integration region is presumed to be more reliable, since it is independent of the energy dependent morphology, which cannot be determined directly without extrapolation for the highest energy bins in the spectrum. Monte-Carlo studies were preformed to test for influences from the position and size of the exclusion region for the source PSR B1259−63. Effects from this source are estimated to be about 2% on the integrated flux, smaller than statistical and systematic errors.

5.3 XMM-Newton X-ray Observations

The XMM-Newton (X-ray Multi-Mirror Mission - Newton) is an orbiting X-ray observatory, launched by the European Space Agency on 10 December, 1999. It is the successor to the previous Rosat X-ray observatory and is sensitive over the energy range 0.2 keV to 12 keV with a field of view of $\sim 30'$ and a spatial resolution of $\sim 4''$. The observatory consists of three telescopes which use grazing incidence mirrors (see Figure 5.10) to focus X-rays onto the three European Photon Imaging Cameras (EPIC). The cameras consist of several imaging CCD chips.

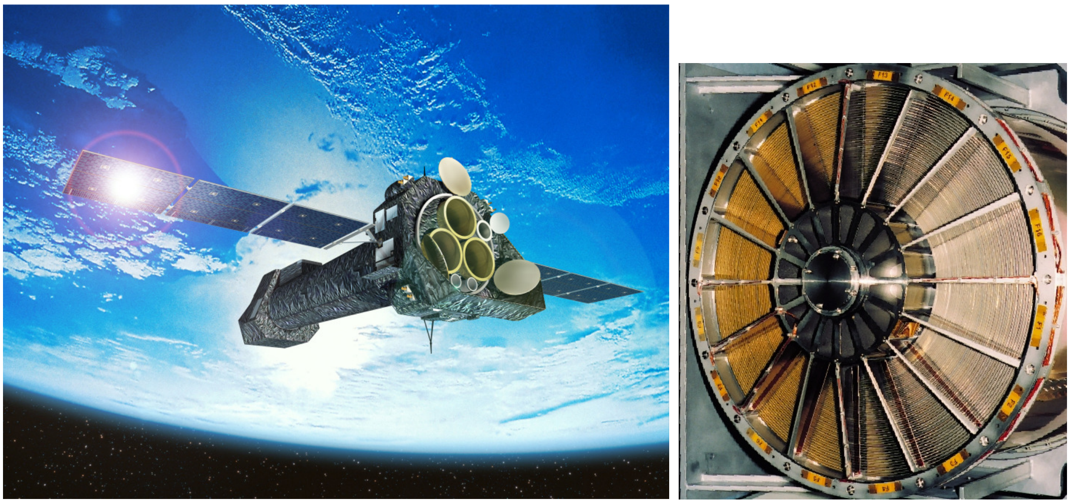

Figure 5.10: Left: The XMM-Newton X-ray Satellite. Right: XMM-Newton X-ray grazing incidence mirrors. Images taken from `http://xmm.esa.int`

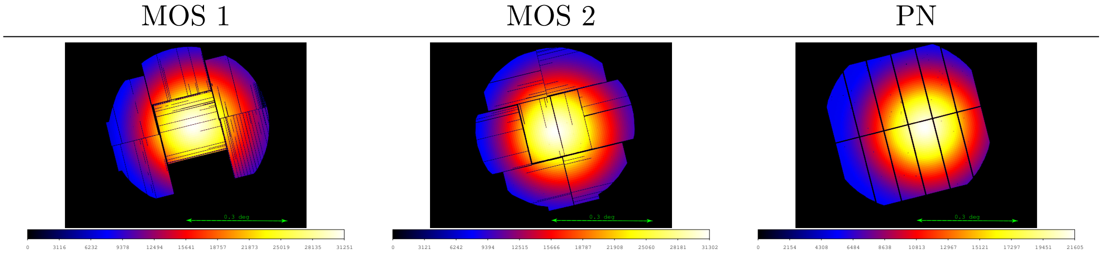

Figure 5.11: The XMM-Newton cameras, MOS 1, MOS2 and PN. The color scale shows the sensitivity where the roughly rectangular regions indicate the CCD chips of the cameras. The rounded edges of the images is due to vignetting. Some pixels and rows of pixels are broken and are blacked out, as well as one of the CCD chips in MOS 1 which was likely hit by a micro meteorite in 2005 shortly before the observations of HESS J1303−631 were taken. The green arrows show the scale 0.3°.

5.3.1 XMM Newton X-ray Observations

In a search for counterparts to the TeV source in the keV energy band, two XMM Newton observations, each about 30 ksec, were carried out on July 12th and 14th, 2005, in satellite revolution number 1024 (ObsID 0303440101, “Observation 1”) and revolution

1025 (ObsID 0302340101, "Observation 2") respectively. All three X-ray imaging CCD cameras (EPIC MOS1, MOS2, and PN, shown in Figure 5.11) were operated in full-frame mode (maximum aperature), with a medium filter (80 nm Al + 160 nm polyimide) to screen out optical and UV light, with the exception of the PN camera which, during the first observation, was operated instead in Large Window mode, which reduces the field of view and thus the data rate (useful when high fluxes are expected or to block out high flux sources which are not of interest) with the Thin1 filter (40 nm Al + 160 nm polyimide).

Data Quality

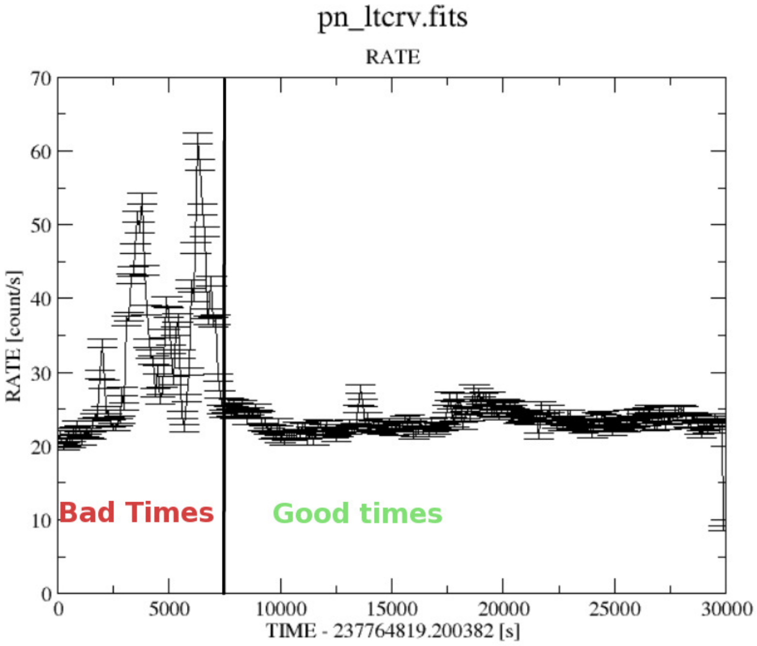

Figure 5.12: Event rate for the PN camera, XMM-Newton Observation 1 of the HESS J1303−631 emission region. High event rates from a solar flare can be easily seen in the beginning of the observation. These periods of high background are removed from the data and only "good time intervals" are used for the analysis.

XMM-Newton X-ray data often suffers from solar proton flares. Particles from the solar wind show up as very large background in the data, which can obscure the observation. The effects are frequently overwhelming and cannot simply be subtracted from the data. Instead, a plot of the event rate is made and periods of high and unstable event rates are either determined by eye or algorithmically. These periods are then removed from the data before further analysis. As can be clearly seen in the event rate for Observation 1

(Figure 5.12), there was a proton flare near the beginning of the observation which has been removed for this analysis.

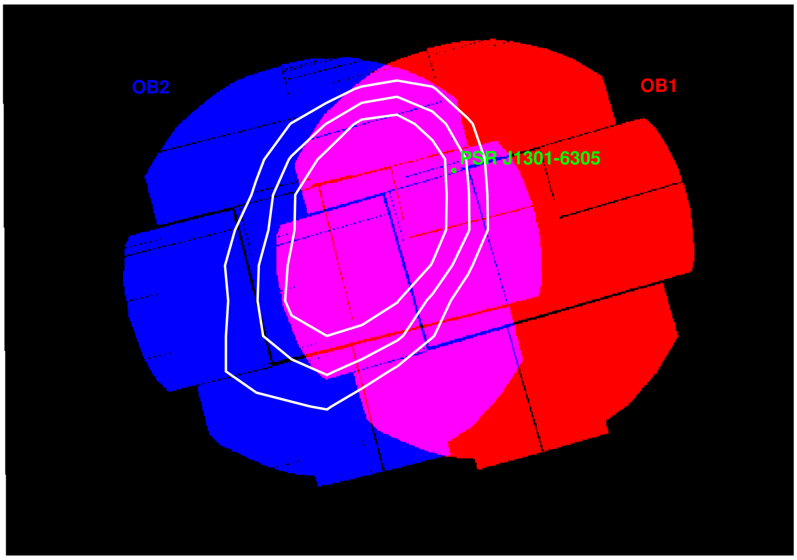

Figure 5.13: The two XMM-Newton observations of HESS J1303−631. This shows the FOVs of the observations relative to the H.E.S.S. 16, 18 and 20 σ significance contours (shown in white), and the pulsar position (green dot).

Observation 1 has the pulsar position closer to the center of the field of view than Observation 2, as shown in Figure 5.13, and it would be, therefore, expected to be more sensitive in the pulsar region. However, as can be seen in Figure 5.14 Observation 2 was found to show signs of diffuse X-ray emission extending from the pulsar in the East direction. Observation 1 is, unfortunately, not suited for studying the extended X-ray source since the extended region found in Observation 2 lies directly on/between the edges of the CCD chips in all three telescopes in Observation 1, thereby obscuring the view of this source, as shown in Figure 5.15.

Data Analysis

For the data analysis of these observations, the XMM-Newton Science Analysis Software (SAS), version 9.0, was used [Snowden et al., 2004]. Cleaning the data and removing periods of high background due to soft proton flares resulted in a combined data set of about 52 ksec exposure. The SAS task emosaicproc was used to combine the observations and perform source detection, taking into account the changing PSF over the FOVs of the individual observations, resulting in the detection of 73 point sources within the combined field of view above the maximum likelihood threshold of 10. The pulsar, PSR J1301−6305, was also detected as a point source in this way, however, there appears to be an extended asymmetric X-ray source associated to the pulsar which requires separate analysis as presented in the following section.

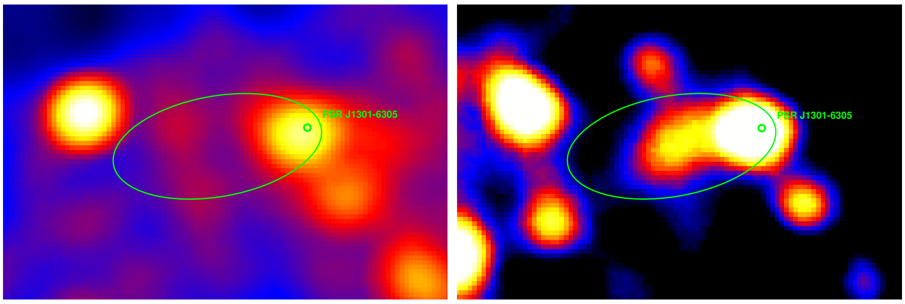

Figure 5.14: XMM-Newton smoothed count map in the region of PSR J1301−6305. Left: observation 1, Right: observation 2. The pulsar, PSR J1301−6305, is shown as a green dot. Whereas observation 2 seemed to show an extended region next to the pulsar, observation 1 seemed to contradict that.

5.3.2 Extended X-ray PWN

For this analysis, the band 2 - 8 keV was used to optimize the signal to noise ratio, since no events are expected at lower energies due to high absorption. The pulsar PSR J1301−6305 was detected in this band as a point source with a flux of $(3.7 \pm 0.6) \times 10^{-14}$ erg cm^{-2}s^{-1} using emosaicproc. This point source corresponds to the 2XMMi catalog source 2XMM J130145.7−630536 [Watson et al., 2009].

As can be seen in Figure 5.16, there is a region of extended emission stretching from the pulsar toward the East, roughly in the direction of the HESS peak, but also roughly in the direction of a star formation region, IRAS 13010−6254. In order to determine the precise direction of the extension, an azimuthal profile was taken around the pulsar position (Figure 5.17) with inner radius of 48″ and outer radius of 120″. The projected on-counts were then fitted with a Gaussian plus background giving a position angle of the extension of $101.5° \pm 5.3°$ and a Gaussian width of $33.4° \pm 5.0°$.

The fitted position angle is consistent to within $1\,\sigma$ with the direction of the star formation region, IRAS 13010−6254, located at a position angle of 106.3°, at the opposite side of the H.E.S.S. VHE peak, but within the $14\,\sigma$ significance contour. This star formation region is the only star formation region within $\sim 2°$ of the HESS source and, in the absence of a detected supernova remnant, presents the only identified plausible birth place for the pulsar.

In order to determine the extension of the asymmetric X-ray PWN, a slice on the count map containing the pulsar was taken (Figure 5.18) in the direction determined by the azimuthal projection, with a slice width of 88″ and a length of 238″. A background slice was chosen in a source free region at roughly equal offset to the center of the FOV as the on slice to ensure equal exposure. The slices are completely contained within a single chip in the MOS1 and MOS2 cameras and extend $\sim 40''$ over the edges of neighboring chips in the PN camera.

The unrelated point source in the projection, was fitted with the *XMM-Newton* PSF,

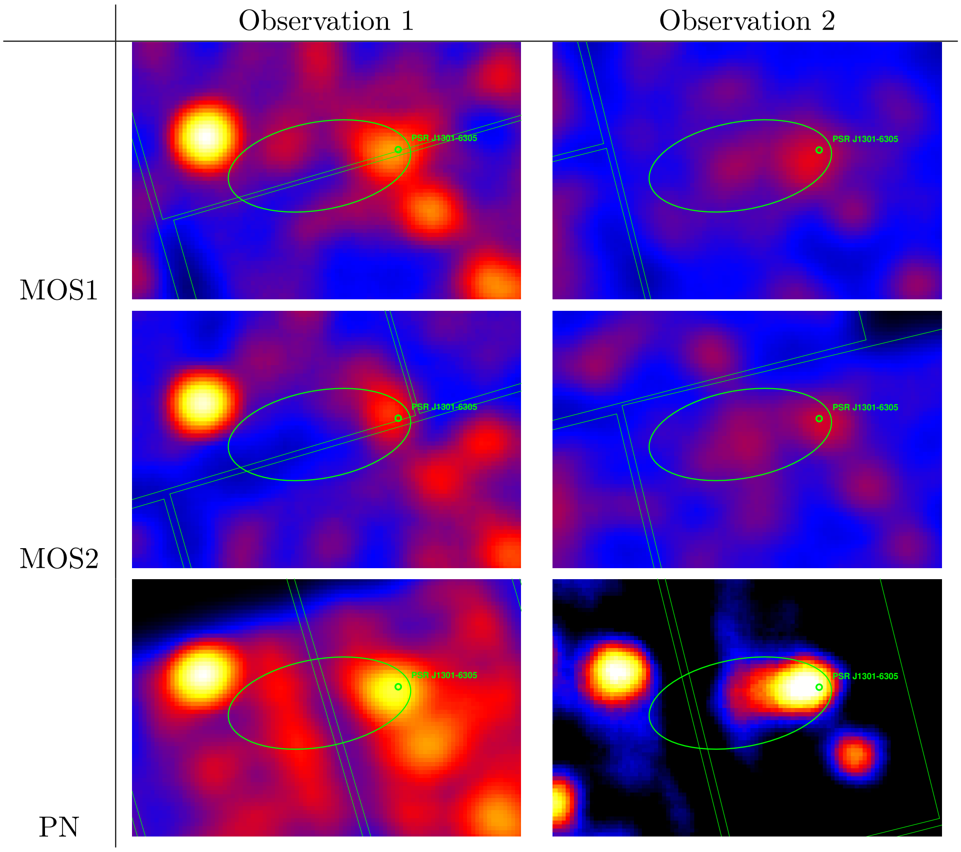

Figure 5.15: The fluxes in the 3 individual XMM-Newton cameras for the two observations. The green lines show the edges of the CCD chips for each of the three cameras. Observation 1 has, unfortunately, the X-ray extension located directly between the camera chip edges in all three cameras and is therefore not appropriate for studying the X-ray extension.

i.e. a King profile,

$$f(x) = \frac{C}{\left(1 + (\frac{x - x_0}{R_0})^2\right)^{\alpha}}, \tag{5.2}$$

with $R_0 = 4.3''$ and $\alpha = 1.5$, corresponding to the PSF for the PN camera at 1.5 keV and at $\sim 10'$ offset from the center of the field of view. For the other cameras, the PSF is slightly narrower than this. The point source in the slice was fitted simultaneously with a compact Gaussian near the pulsar position and a larger Gaussian to the extended region (Figure 5.19).

The point source and the extended region were then subtracted leaving just the "compact" emission region near the pulsar position as shown in Figure 5.20. This was then fitted with a Gaussian function in the region $-70''$ to $+40''$ around the pulsar position. This region was fitted with a Gaussian, center -11.9 ± 4.2, Gaussian width 14.7 ± 3.2,

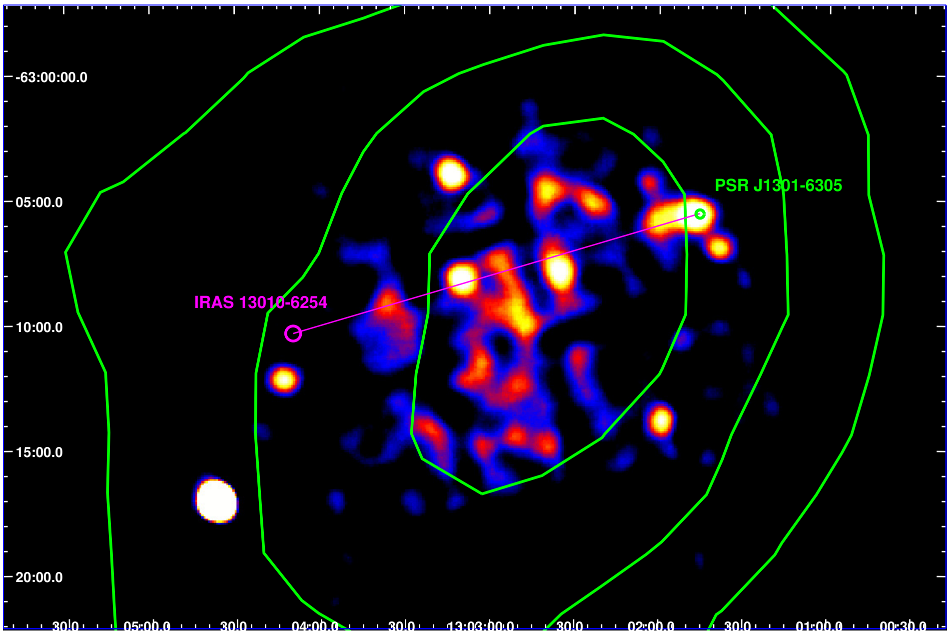

Figure 5.16: Smoothed flux map of XMM X-ray observation 2 of HESS J1303−631 in the 2 to 8 keV energy band, overlaid with H.E.S.S. Gamma-ray significance contours in green. The green dot shows the position of the pulsar PSR J1301−6305. An X-ray extension appears to the left of the pulsar position. Nealy 100 X-ray point sources, most of them unidentified, have been detected by XMM in this FOV and appear in the 2XMMi catalog [Watson et al., 2009].

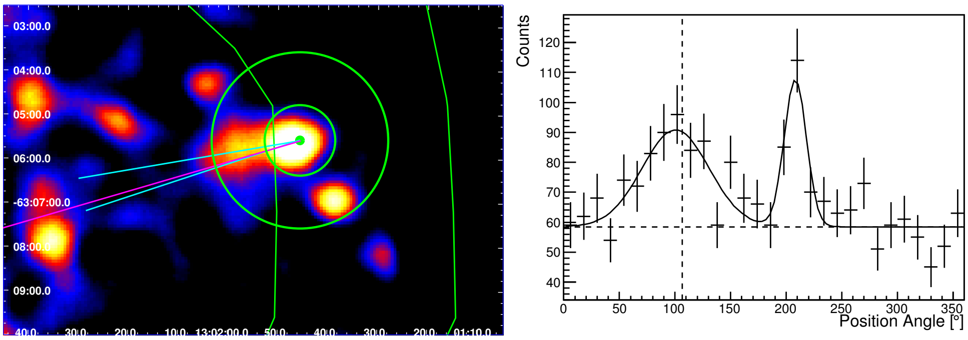

Figure 5.17: Left: The projection annulus used to determine the direction of the X-ray extension, shown in green with inner radius of 48″ and outer radius of 120″. Right: The X-ray azimuthal projection in position angle from the pulsar position, where 0° corresponds to North and positive position angles measured counter-clockwise. The projected on-counts were fitted with the sum of a Gaussian and a flat background giving a position angle of 101.5° ± 5.3° and a Gaussian width of 30° ± 7°. The direction of the extension is found to be within $1\,\sigma$ from the direction of the star formation region, IRAS 13010−6254, located at a position angle of 106.3°, indicated by a magenta line in the sky map and a dashed line in the projection. The cyan lines in the sky map show the $1\,\sigma$ errors in the fitted direction of the extension.

which yielded an equally good fit as a fit to two point sources with fit qualities χ^2/NDF of 13.42/10 and 10.16/9 respectively (see Figure 5.20).

Taking an integration region from the edge of the PN chip to the pulsar position gives total on-counts of 950, and total background counts 689 with the on/off area ratio $\alpha = 1$ for an excess of 261 corresponding to a significance of $6.5\,\sigma$.

5.3.3 X-ray Spectrum

For the spectrum a small elliptical region covering the extension was taken as shown in Figure 5.21.. The on-region for spectral extraction was centered at $\alpha = 13^{\mathrm{h}}02^{\mathrm{m}}00^{\mathrm{s}}$, $\delta = -63°05'54''$ (where α is the right ascension coordinate and δ is the declination), with radii $1.'9$ and $0'.9$ with the major axis oriented along the position angle 101.5°. The background region was taken with the same dimensions but centered on $\alpha = 13^{\mathrm{h}}01^{\mathrm{m}}52^{\mathrm{s}}$, $\delta = -63°08'55''$. The obtained spectrum was fitted using the spectral fitting software XSPEC.

The spectrum was fitted to an absorbed power-law model which yielded the following parameters: $N_H = (3.6 \pm 1.4) \times 10^{22}$ cm^{-2}, $\Gamma = 2.7 \pm 0.6$, norm $= (1.4 \pm 2.4) \times 10^{-4}$ keV^{-1}cm^{-2}s^{-1}, N_H is the fitted column density which manifests itself as absorption

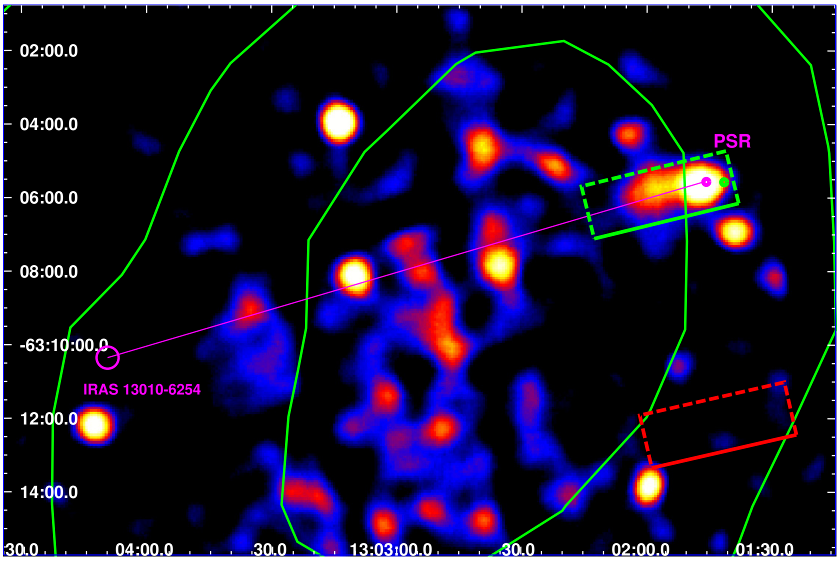

Figure 5.18: Smoothed XMM-Newton X-ray flux map. An extended X-ray source appears from the position of the pulsar, PSR J1301−6305 (magenta dot), and extends roughly in the direction of the H.E.S.S. peak (green contours show 8, 14 and 20 σ Gamma-ray significance) and in the direction of the star formation region, IRAS 13010−6254 (magenta circle). The green box shows the slice on excess events in the 2 − 8 keV energy band. A presumably unrelated soft point source, 2XMM J130141.3-630535, is shown as a green dot.

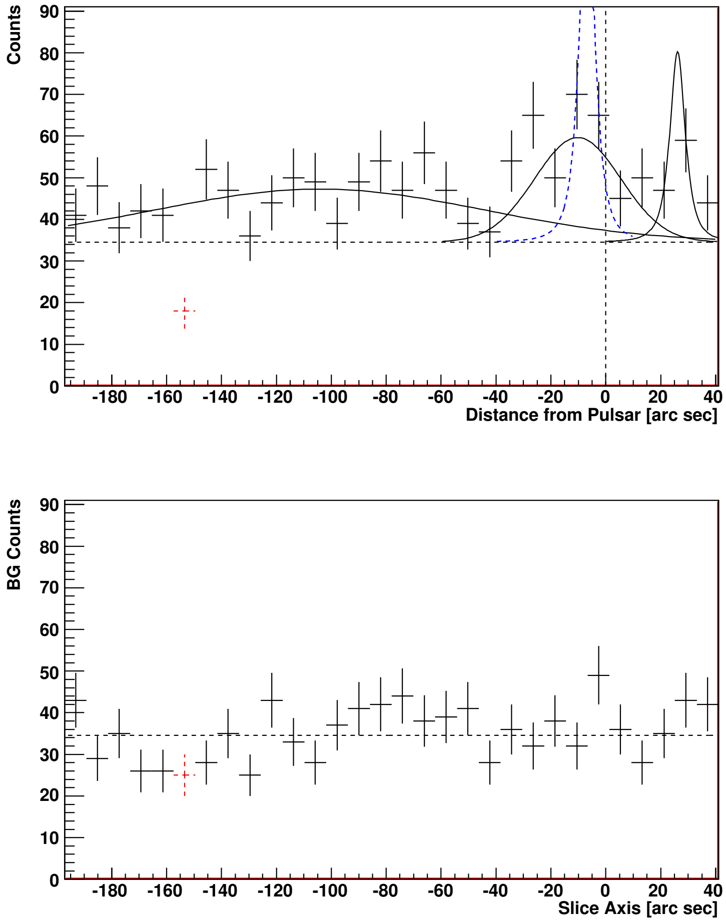

Figure 5.19: Top: the slice used for determination of X-ray extension. The presumably unrelated soft source, 2XMM J130141.3-630535, is fit with a King profile on the right. The compact region near the pulsar is fit with a Gaussian and a King profile is shown for comparison as a blue dashed line. The extended emission is fit with a Gaussian on the left.
Bottom: the slice used for background determination. The red dotted bin lies directly on a chip edge in the PN camera and is excluded from the analysis. The black horizontal dashed line indicates the fitted background level from a simultaneous fit of the sources and background slices. The vertical dashed line indicates the pulsar position.

Band	Mean	Width	Int. Width	P
E_1	$0.001° \pm 0.012°$	$0.214° \pm 0.011°$	$0.203° \pm 0.012°$	0.43
E_2	$0.010° \pm 0.013°$	$0.172° \pm 0.013°$	$0.168° \pm 0.013°$	0.15
E_3	$0.098° \pm 0.022°$	$0.080° \pm 0.020°$	$0.075° \pm 0.021°$	0.97

Table 5.2: Results of the Gaussian fit to the slices on the excess maps in the energy bands E_1 = (0.84 - 2) TeV, E_2 =(2 - 10) TeV and $E_3 > 10$ TeV. "Mean" is the mean of the Gaussian, "Width" is the Gaussian width and "Int. Width" is the intrinsic Gaussian width of the source after correcting for the PSF, P is the p-value of the fit.

Constant Fit	χ^2/NDF	p-value
Intrinsic Width	44.9 / 2	1.8×10^{-10}
Gaussian Mean	18.3 / 2	1.1×10^{-4}
Linear fit		
Intrinsic Width	0.4 / 1	0.55
Gaussian Mean	2.4 / 1	0.12

Table 5.3: Quality of fit of a constant to the source intrinsic Gaussian extension and mean, measured from pulsar position, as a function of energy. The bad p-values indicate the presence of significant energy-dependent morphology.

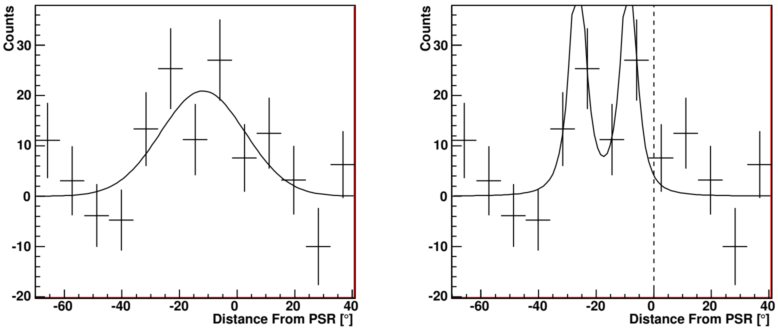

Figure 5.20: Zoom in of the slice on the X-ray extension near the pulsar after subtracting the fitted background, unrelated point source and extended emission region. A fit to a Gaussian (left), center -11.9 ± 4.2, Gaussian width 14.7 ± 3.2, yielded an equally good fit as a fit to two point source (right) with fit qualities χ^2/NDF of 13.42/10 and 10.16/9 respectively.

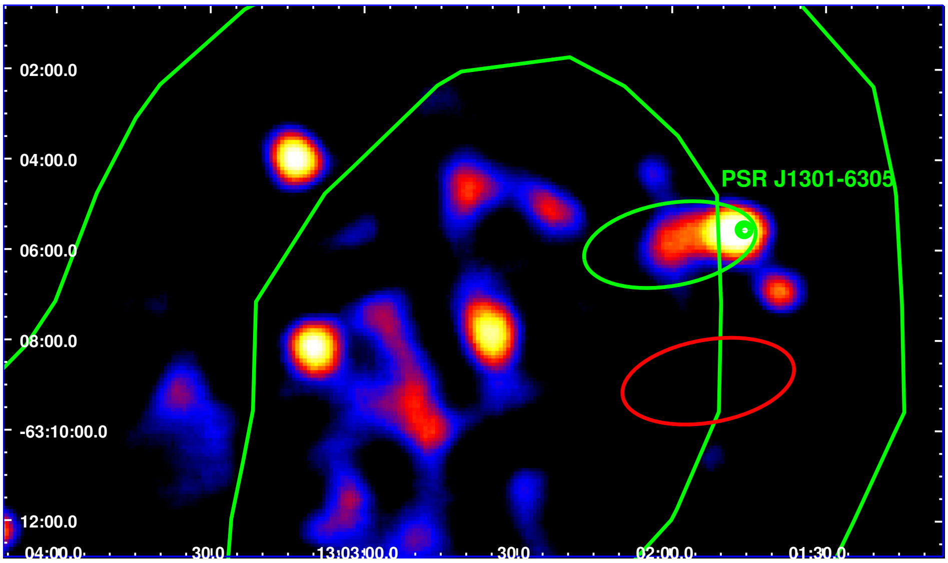

Figure 5.21: The regions used for X-ray spectral extraction. The green ellipse shows the region used for signal extraction and the red ellipse shows the region used for background extraction. The regions were chosen to avoid other known sources and have roughly equal distance from the center of the field of view.

of the photons especially at lower energies.

Fixing the column density to this value in the spectral fit decreased the errors on the fit and yielded the following fit parameters: $\Gamma = 2.7 \pm 0.2$, norm $= (1.3 \pm 0.7) \times 10^{-4}$ keV^{-1}cm^{-2}s^{-1}. This has, however, negligible effect on the integrated unabsorbed flux which is found to be

$$F_{2\text{-}10\text{ keV}} = 1.2 \times 10^{-13} \text{ erg cm}^{-2}\text{s}^{-1}.$$

5.3.4 PMN Radio Observation

The region of HESS J1303−631 was covered by a survey of the southern sky by the Parkes, MIT and NRAO (PMN) radio telescopes at 4.85 GHz [Condon et al., 1993]. Calibrated maps were obtained from the NASA SkyView online tool, shown in Figure 5.22. There appears to be a radio source just East of the X-ray nebula and near the peak of the VHE source. The feature is found to have a peak flux of 0.030 Jy/beam, where one beam defines the resolution of the radio observation, in this case, 7′ FWHM. This flux is at the detection limit of the survey, so this feature is not significant (and thus not reported in the catalog) and the flux is taken as an upper limit. This feature is consistent with the size of the PSF of the survey in the North-East to South-West direction, but may be slightly elongated in the North-West to South-East direction. Since the feature is not significant, no definitive conclusions can be made.

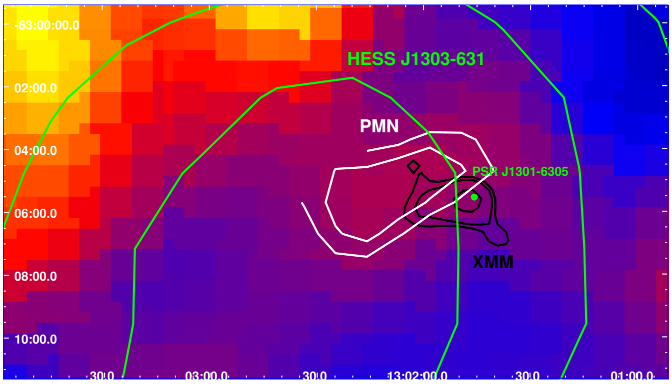

Figure 5.22: 4.85 GHz radio image from the PMN Survey in the HESS J1303−631 region. H.E.S.S. contours are shown in green, XMM Newton X-ray contours are shown in black and the radio contours are shown in white. A radio source peaks about 3’ East of the pulsar position, just beyond the extended XMM X-ray source and near the center of the H.E.S.S. Gamma-ray source at a peak value of 0.03 Jy/beam.

Although it is unclear whether this radio feature does indeed represent a counterpart to the Gamma-ray and X-ray sources, since this lies in a rather complicated region of the radio sky, the location is promising due to its similarities with other known pulsar wind nebulae having a radio peak just beyond the X-ray nebula, as in, for example, PSR B1929+10 [Becker et al., 2006] and the much smaller scale example of the “Mouse” pulsar wind nebula [Gaensler et al., 2004b]. It is, however, difficult to determine an association with confidence, because the observed feature is roughly the size of the PSF, though there may be a slight elongation. The radio feature seen here is not resolved, as shown in Figure 5.22. Further observations at radio wavelengths may be able to determine more precise morphology and polarization in order to strengthen the association.

5.4 Discussion of Multi-Wavelength Results

Having analysed the morphology and spectra in Gamma-ray, X-ray and radio data available for the region, it is now possible to consider this source in a full multi-wavelength scenario. First, an energy mosaic, or color image of the source, was created using three smoothed excess maps with threshold energies $E_\gamma < 2$ TeV, $2\,\mathrm{TeV} < E_\gamma < 10$ TeV and $E_\gamma > 10$ TeV (Figure 5.7). These three maps were then overlaid, as shown in Figure 5.23, along with the contours of the extended X-ray PWN and the contours from the radio feature, to produce an energy mosiac image of the source. This mosaic is rather reminiscent of the known *off-set PWN* association HESS J1825−137 [Aharonian et al., 2006f] where the low energy Gamma-ray emission region is quite extended with the pulsar laying towards the edge of emission and with the higher energy emission more compact and found centered closer to the pulsar.

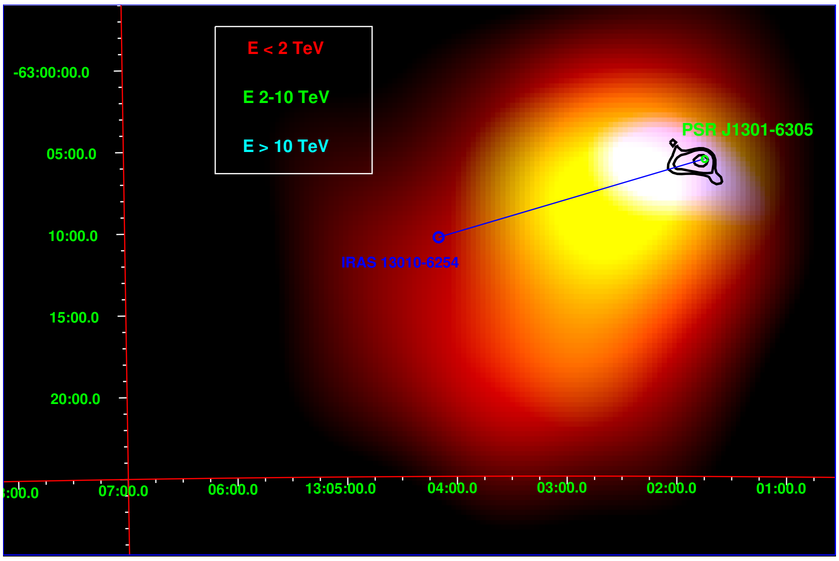

Figure 5.23: Energy mosaic of HESS J1303-631. Red: $E_\gamma < 2$ TeV, Green: 2 TeV $< E_\gamma < 10$ TeV, Blue: $E_\gamma > 10$ TeV. The highest energy photons originate nearest the pulsar, PSR J1301−6305. XMM X-ray contours are shown in white.

5.4.1 Spectral Energy Distribution

Taking the spectra and fluxes obtained in previous sections, it is now possible to consider the SED of the source in a PWN scenario. In order to fit the Gamma-ray spectrum from H.E.S.S., the unabsorbed X-ray spectrum as obtained from XMM Newton and the single radio point at 4.85 GHz as obtained from the PMN survey, a simple stationary leptonic model was used (Figure 5.24).

The leptonic model assumes that the same electron population creates radio and X-ray emission via synchrotron and TeV Gamma-rays via inverse Compton scattering on the Cosmic Microwave Background photons [Blumenthal and Gould, 1970, Rybicki and Lightman, 1979]. An electron energy distribution of the form of a power law with exponential cut-off was used:

$$\frac{dN}{dE} = KE^{-\alpha}e^{-\frac{E}{E_{\mathrm{cut}}}}$$

The fit of the radio, X-ray and Gamma-ray data with this model yielded an electron spectral index of 1.9 and cut-off energy of 42 TeV and an average magnetic field of ~ 0.9 μG. Since the fluxes at the various energies used in this model are extracted from regions of differing size, the fitted magnetic field represents only an average, thus the errors on the parameters are not given, since the actual field strength and other parameters may vary significantly across the nebula. However, these average values still may provide a rough estimate of what is at work in this source, for example, the fitted average magnetic

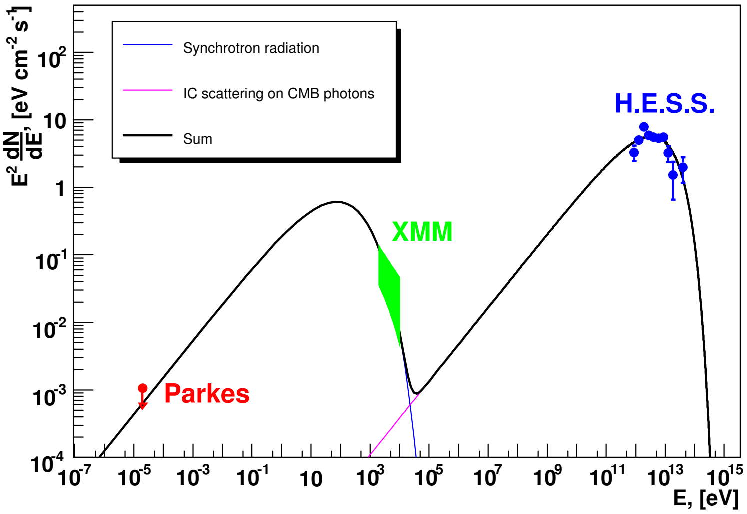

Figure 5.24: Spectral Energy Distribution of HESS J1303−631 fitted with a simple stationary leptonic model. The required magnetic field is $\sim 0.9\mu$G.

field for this source is the lowest of any PWN yet detected which may be expected given the abnormally low synchrotron levels detected. A more complete model, including the various electron populations and the variation of the magnetic field across the source, will become possible if increased multi-wavelength coverage becomes available, completing the broad band SED.

Integrating the electron spectrum above 511 keV, the obtained total energy in electrons is $\sim 3 \times 10^{48}$ erg. Dividing by the $1\,\sigma$ Gaussian volume of the H.E.S.S. source (assuming the distance of 6.6 kpc) gives a PWN particle pressure of $\sim 1,700$ K cm^{-3}. Typical values of the pressure of the ISM range from 10^3 to 10^4 K cm^{-3} [Jenkins, 2004], implying that the energetics of the electron population are sufficient for PWN expansion. This implies an energy density in particles 3 orders of magnitude higher than the energy density in the magnetic field, meaning that the expansion would have been mediated by particle-particle pressure and not by magnetic pressure.

5.4.2 Distance to the Source

As stated before, the distance of 6.6 kpc to PSR J1301−6305 is based on the dispersion measure using a model of electron distribution in the Galaxy from Cordes and Lazio [2002], a method which is often considered unreliable, especially at large distances, partly because the Galactic electron distributions are calibrated using the dispersion measures of pulsars with known distances (e.g. from parallax measures which are only possible for nearby pulsars). Furthermore, the very large absorption measured in the X-ray spectrum, consistent with the entire measured Galactic column density in that direction, implies a larger distance than 6.6 kpc. For example, the "Mouse" pulsar has been argued to be at a distance roughly twice that determined by its dispersion measure based on the ratio of its X-ray column density to dispersion measure [Gaensler et al., 2004b].

On the other hand, the star formation region, IRAS 13010−6254, provides an alternative estimation of the distance. As mentioned earlier, it is the only star formation region within more than a degree of the pulsar and there is yet no detected potentially associated supernova remnant. Since the X-ray trail is also found to point back in that direction, this provides the best candidate for the birthplace of the pulsar, and, as such, deserves special attention.

IRAS 13010−6254 has a kinematic velocity of $V_{\mathrm{SLR}} = 33.4$ km/s, which corresponds to a distance of $\sim$ 12.6 kpc [Brand and Blitz, 1993], roughly double the distance of 6.6 kpc based on dispersion measure, placing the source closer to the edge of the Galaxy. This kinematic distance is more consistent with the measure of the column density from X-rays, which is $1.1\,\sigma$ larger than the total integrated Galactic column density in that direction, augmenting the arguments for association, and agrees more with the original estimation of the pulsar distance of 15.8 kpc based on an older model of the Galactic electron distribution from Taylor and Cordes [1993].

5.4.3 Morphology of the X-ray Nebula

Furthermore, this would imply that the compact Gaussian X-ray source associated to the pulsar, with a Gaussian width of $14.7''$ would correspond to an extension of about 1 pc. This feature may represent the pulsar wind termination shock. To calculate the expected radius of the pulsar wind termination shock, r_{ts}, assume the wind is flowing relativistically at the velocity of light, c, and that the system is in a steady state. Then the total energy inside the shock region is given by $\dot{E}\frac{r_{ts}}{c}$. Dividing by the volume then gives the total pressure:

$$p = \frac{\dot{E}/c}{4/3\pi r^2} \tag{5.3}$$

Equating this pressure to the ISM pressure, with typical values ranging from 10^3 to 10^4 K cm^{-3} [Jenkins, 2004], gives r_{ts} ranging from 3 to 1 pc respectively. This is in good agreement with the size of the compact X-ray source assuming the kinematic distance of the star formation region. Assuming a pulsar distance of 6.6 kpc from dispersion measure, on the other hand, would require a rather high ISM pressure of 4.4×10^4 K cm^{-3} to bring the size of the wind termination shock down to the $1\,\sigma$ Gaussian size of the compact X-ray region. This implies that a distance of 6.6 kpc is unlikely.

If the pulsar is moving at a significant space velocity, the extended asymmetric X-ray emission may represent a turbulent flow of the interstellar medium past the pulsar termination shock (in the pulsar's reference frame). On the other hand, if the pulsar is moving at supersonic speeds relative to the ambient gas, a bow shock may form, confining some of the electrons accelerated at the termination shock and producing enhanced X-ray synchrotron radiation. In the case of a pulsar inside the supernova remnant of its progenitor, the extension could also reflect a collision of the expanding PWN with the reverse shock of the supernova remnant. The resolution of the data is unfortunately not sufficient to distiguish between these possibilities, however, the lack of a detected supernova remnant makes latter scenario of a crushed PWN unlikely. Instead, the extension is likely indicative of the motion of the pulsar.

5.4.4 Pulsar Velocity and Age

If this compact X-ray region is taken to be the termination shock, its large offset from the pulsar position would imply a high space velocity relative to the ISM. In fact, it is possible to calculate the velocity of the pulsar if the relative radii of the forward (r_{ts}^{F}) and backward (r_{ts}^{B}) shocks are known as

$$\frac{r_{ts}^{B}}{r_{ts}^{F}} = \gamma^{1/2} M \tag{5.4}$$

where M is the Mach number and γ is the adiabatic coefficient, equal to 5/3 for a monoatomic nonrelativistic gas assumed for the ISM [van der Swaluw et al., 2003, Bucciantini, 2002].

Unfortunately, the statistics in the X-rays do not make it entirely clear exactly where the forward and backward termination shocks lie. However, if the outer edges of the two King profiles in Figure 5.20 are taken, or conversely the forward and backward edges of the Gaussian using the first bins compatible with zero, a rough estimate of the forward and backward termination shocks may be obtained as $r_{ts}^{F} = 7''$ and $r_{ts}^{B} = -36''$. Applying Equation 5.4 gives a Mach number of 4.0, independent of the distance to the pulsar. If the pulsar is assumed to be traveling through the hot ionized medium, with $\rho = 10^{-4}$ to 10^{-2} atoms/cm^3, believed to make up 30-70% of the volume of the Galaxy [Ferrière, 2001], and typical pressures as given above, this would correspond to a space velocity in the range 150 - 4700 km/s.

If the pulsar was born in IRAS 13010−6254 then it would have travelled 0.28° or ~ 62 pc, implying a velocity of $\sim 5,000$ km/s if the characteristic age of 11 kyr is to be believed. This age, however, relies on two assumptions that have both been shown to be unreliable. First, the pulsar braking index is assumed to be $n = 3$ (as obtained from pure magnetic dipole radiation), however, true braking indices have only been measured reliably for 5 pulsars and all have been found to be less than 3 [Livingstone et al., 2007]. Secondly, the determination of the characteristic age relies on the assumption that the birth period is much smaller than the current pulsar period, $P_0 \ll P$, which has also been shown to not always be the case. Furthermore, the pulsar PSR B1757−24 (with very similar spin down parameters to PSR J1301−6305) has been shown to be likely a factor of at least 3 older than its characteristic age would imply [Zeiger et al., 2008]. If this is also true in the case of PSR J1301−6305, it would bring the pulsar velocity down to a much more reasonable value, i.e. $\sim 1,500$ km/s. In the case that the pulsar is much older than 11 kyr, IC cooling may play an important role for the oldest electrons, i.e.

those created nearest the place of birth.

Pulsar Wind Nebula Energetics

The kinematic distance obtained in Section 5.4.2 is nearly double the distance obtained from dispersion measure, which would quadruple the derived luminosity in Gamma-rays, so that the integrated Gamma-ray luminosity above 1 TeV would represent about 7.4% of the current spin-down luminosity of the pulsar. This larger distance and possibly older age of the pulsar may help explain not only the high absorption in the X-ray spectrum, but also the lack of a detected supernova remnant.

The Gamma-ray extension radius of $\sim 0.18^\circ$ is about a factor of 10 larger than the X-ray PWN with an extension of about $\sim 60''$. While this relative size difference is large, it is not as severe as in the case of HESS J1825−137, considered a prototype of the class of so-called *offset Pulsar Wind Nebulae*, where the size difference in Gamma-ray and X-ray emission regions is 0.5° to $5''$ respectively, a factor of greater than 300 difference in size, so the size discrepancy in the case of HESS J1303−631 is not unreasonable.

5.5 Conclusions

The observations presented allow the identification of HESS J1303−631 as a pulsar wind nebula, where a large cloud of electrons accelerated by the pulsar at the wind termination shock emit Gamma-ray radiation through the inverse Compton mechanism. These electrons can have an inverse Compton emission lifetime of the order of the pulsar age, and can, therefore, reflect the total energy output of the pulsar since birth, while the X-ray part of the PWN, generated by higher energy synchrotron emitting electrons with a much shorter lifetime, is seen to decrease rapidly in time and reflects only the more recent spin-down power of the pulsar [Gaensler et al., 2004a].

While an association of the pulsar with the star formation region IRAS 13010−6254 is not conclusive, it is shown to be plausible and, currently, the only plausible birth place for the pulsar. Also, such an association provides a convenient explanation for the high absorption in X-rays and the lack of a detected associated supernova remnant.

PWNe now appear to constitute the largest class of VHE Gamma-ray emitters. The first dark source, and considered "prototypical" dark source, TeV 2032+4131 discovered by the HEGRA collaboration [Aharonian et al., 2002], was recently found to be spatially coincident with the Fermi discovered source, 0FGL J2032.2+4122, conclusively identified by the Fermi collaboration as a pulsar through detection of pulsed Gamma-ray emission [Abdo et al., 2009]. Also, there have been recent deeper X-ray and radio observations that have revealed this source may be "not-so-dark" [Butt et al., 2008] as previously thought, after deep observations revealed the existence of faint counterparts at lower frequencies. HESS J1303−631 appears now also to belong to the not-so-dark class of Gamma-ray emitters. Many other extended Galactic Gamma-ray sources which were previously unidentified are also finding associations with pulsars and PWNe as this class of sources continues to expand.

6 Summary

The development of the field of Gamma-ray astronomy has opened up a new window on high energy processes in the Universe. Highly energetic objects, such as supernova remnants and pulsar wind nebulae, can accelerate particles to high energies which in turn can produce VHE Gamma-ray radiation which can be detected on Earth. Generally, the detection of these objects at VHE energies can allow better constraints on the physical parameters of the objects, such as local magnetic fields and the energies of electron or positron populations which is not possible with the observation of synchrotron radiation alone. Pulsar Wind Nebulae have been observed by astronomers in all ranges of the frequency spectrum, yet observation of these sources in the TeV range unequivocally identifies them as sites of acceleration of very high energy particles.

The detection of a large number (> 20) of unidentified Galactic TeV Gamma-ray sources, first TeV J2032+4130 by HEGRA, then HESS J1303−631, discovered by H.E.S.S., followed by many more such discoveries by H.E.S.S., has presented a mystery with ramifications for astronomy, cosmic-ray science and astrophysics. The identification and classification of these sources could change our understanding of the populations and energetics of the sources of cosmic-rays.

The particular case of HESS J1303−631, originally classified as a "dark source", is examined in this work, employing multi-wavelength studies to identify this source as a "synchrotron underluminous" pulsar wind nebula. First, significant energy dependent morphology has been detected in VHE Gamma-rays and the morphology, with high energy Gamma-rays originating near the pulsar PSR J1301−6305 and lower energies spreading out farther away from the pulsar implies an association with this pulsar. Second, a weak but significantly extended X-ray nebula has been identified and indicates that this pulsar is producing a wind nebula. Third, an upper limit in radio has been obtained from PMN observations. Fourth, combining all of these multi-wavelength results has alowed the construction of a simple "one zone" model of the electron populations in the nebula allowing the estimation of the ambient magnetic field at the level of $\sim 0.9\,\mu$G, helping to explain the relatively low levels of synchrotron emission as predicted by de Jager et al. [2009]. Fifth, a potential birth place of the pulsar, the star formation region IRAS 13010−6254, has been identified within the 14 σ contour of the TeV emission region and is indicated by the direction of extension of the X-ray nebula. Arguments based on the morphology of the X-ray source presented here have shown that such an association is at least plausible and currently the only proposed potential birth place. If true, this allows a more reliable determination of the distance to the source based on the kinematic velocity of the star formation region, instead of the dispersion measure from the pulsar, resulting in a distance of 12.6 kpc. Identification of the birth place of the pulsar can be used to put constraints on the velocity and age of the pulsar, parameters which are otherwise difficult to determine acurately. It has furthermore been shown that the photodisintegration model cannot explain the properties of this source.

PWNe now appear to constitute the largest class of VHE Gamma-ray emitters. The first dark source, and considered “prototypical” dark source, TeV 2032+4131 discovered by the HEGRA collaboration [Aharonian et al., 2002], was recently found to be spatially coincident with the Fermi discovered source, 0FGL J2032.2+4122, conclusively identified by the Fermi collaboration as a pulsar through detection of pulsed Gamma-ray emission [Abdo et al., 2009]. Also, there have been recent deeper X-ray and radio observations that have revealed this source may be “not-so-dark” [Butt et al., 2008] as previously thought, after deep observations revealed the existence of faint counterparts at lower frequencies. HESS J1303−631 appears now also to belong to the not-so-dark class of Gamma-ray emitters. Many other extended Galactic Gamma-ray sources which were previously unidentified are also finding associations with pulsars and PWNe as this class of sources continues to expand.

Appendix A: The H.E.S.S. Point Spread Function

The H.E.S.S. nominal Point Spread Function (PSF) is ~ 0.1° including events from all detectable energies ($E \gtrsim 300$ GeV). This is a rather conservative estimate and the PSF is expected to improve at higher energies where larger and more elongated showers produce images in the Cherenkov telescope cameras which can be constructed with better accuracy than lower energy showers.

Since HESS J1303−631 has an intrinsic extension of about 0.18° it is well resolved as an extended source. However, in the high energy analysis presented here, showing an energy dependent morphology of a source shrinking with energy towards the pulsar, the question is naturally raised of whether at higher energies the source is indeed a point source and to what extent the decrease in image size is attributable to the improving PSF. In order to answer this question, studies were performed using Monte-Carlo (MC) data as well as real data from the Crab pulsar to obtain a detailed description of the evolution of the H.E.S.S. PSF with energy. The MC data consists of simulated showers from a point source produced with CORSIKA [Heck et al., 1998] and then fed through a realistic detector response simulator, sim_telarray [Bernlöhr, 2008]. MC data was produced at energies ranging from 100 GeV to 14 TeV and at zenith angles from $0° - 60°$. The scatter plot of reconstructed event energy and offset from source position for these events, as obtained from MC simulations, is shown in Figure A.0 for zenith angle 0°. The Crab data was found to be in good agreement with the MC data, though the MC data provides better statistics. Only the MC data is presented here for simplicity. Also, only the plots from zenith angle 0° are presented for simplicity, but results for other zenith angles will be summarized.

The H.E.S.S. PSF can be best described by the sum of two Gaussians, one with a typical width of around ~ 0.02° (depending on energy and zenith angle), referred to here as Gaussian A and a second with a typical width of around ~ 0.05°, referred to here as Gaussian B, as such:

$$\frac{dN}{d\theta^2} = N_0 \cdot \left(p \cdot e^{-\frac{\theta^2}{2A_\sigma^2}} + (1-p) \cdot e^{-\frac{\theta^2}{2B_\sigma^2}} \right) \tag{A.1}$$

The widths of the Gaussians (A_σ, B_σ) will, in general, vary depending on the zenith angle of the observations, and the energy range of the measured events, as does the relative scale factor, p, giving a total of three independent parameters describing the PSF, all of which are a function of energy and zenith. The “average” values of $A_\sigma \sim 0.02°$ and

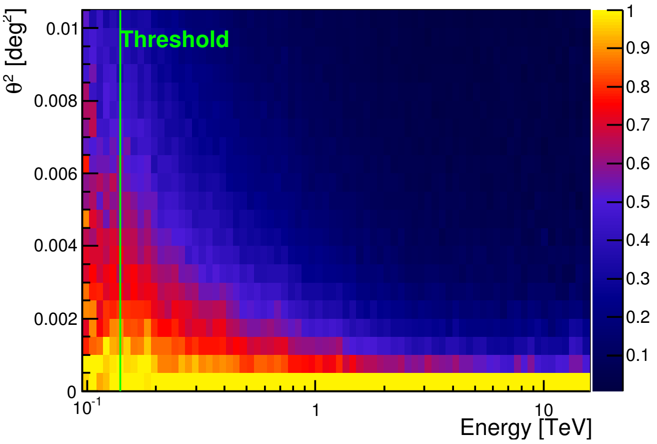

Figure A.0: Distribution of reconstructed MC $\gamma-$ray showers from a point source observed at zenith as a function of Energy and θ^2, the squared angular offset from the center of emission.

$B_\sigma \sim 0.05°$ were obtained by combining the simulated data at every simulated energy and all zenith angles using equal weights and then fit to the PSF equation (Eqn. A.1), with $p = 0.8$ the fraction of the peak position events attributable to the narrower Gaussian, A, see Fig. A.1. Since this distribution contains events from all energies it represents distributions with changing Gaussian widths and so is not well fit with a double Gaussian. Restricting the data to a single energy band produces fits of higher quiality.

In general, the PSF can be well described, producing high probability fits over the ranges investigated here, by two Gaussian widths which are weak functions of energy only and the relative scale parameter, p, which is found to be a much more sensitive function of both energy and zenith angle. To find the energy dependence, the simulated PSFs from all zenith angles were combined into energy bins, $0-1$, $1-2$, ..., $13-14$ TeV and the Gaussian widths obtained this way are shown in Fig. A.1.

The lowest energy bin, $0-1$ TeV, does not in fact include events extending to zero energy, but is limited by the sensitivity range of the instruments, giving a true lower energy limit of about 300 GeV for low values of zenith angle and increasing to arround 1 TeV at 60° zenith. In the end, the true detection threshold of a data set will depend not only on the zenith angles of the observations, but also on the spectrum and intensity of the particular source and the background conditions in the region of observation. At the lowest energies of reconstructed events, very close to the threshold, it was seen that the event distribution does not follow the PSF two Gaussian function as presented here. At the highest zenith angles ($\gtrsim 60°$) and low energies ($\sim 1-2$ TeV), the distribution was even found to have the peak shifted from the simulated source position, which cannot be attributed to a lack of statistics. This is assumed to be due to a bias introduced by the geometry, where, at high zenith angles, showers arriving below the telescope line of sight

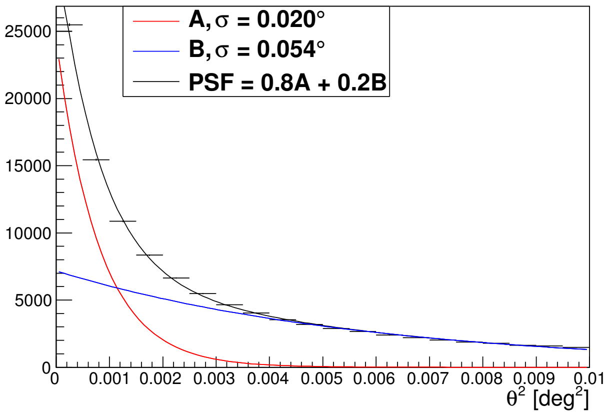

Figure A.1: Combined PSF distribution for all simulated energies and zenith angles with equal weights, fit with a double Gaussian giving the "average" Gaussian widths of $A_\sigma \sim .020°$ and $B_\sigma \sim .054°$ with relative scales of 0.8 and 0.2 respectively. The resulting χ^2/NDF is 247 / 16

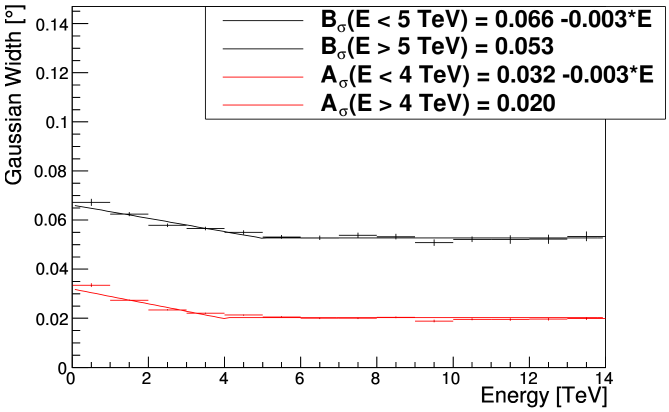

Figure A.1: Fitted widths of the two Gaussians components to the PSF as a function of energy fitted with a piece-wise linear function. The energy dependence is found to be weak, with B_σ and A_σ starting at 0.066° and 0.032° and linearly decreasing to 0.053° and 0.020° above 5 and 4 TeV respectively.

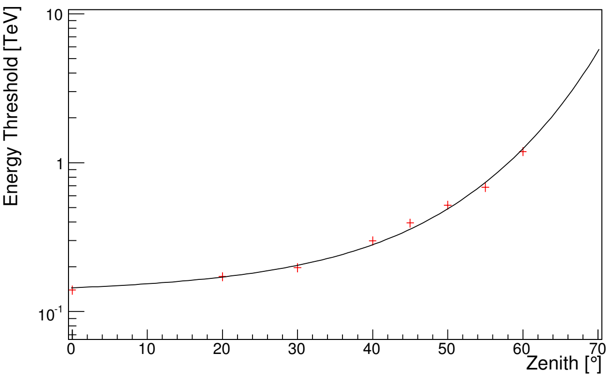

Figure A.1: The threshold applied in this analysis to avoid badly reconstructed events, due to atmospheric extinction, with non-standard PSF such as peaking away from the nominal source position.

are farther then parallel showers above the line of sight and therefore the light collected from these showers may be insufficient to pass cuts applied on the minimum number of photo electrons and image size. This bias in which events are recorded can lead to a bias in the overall reconstructed source position. For this analysis, a low energy threshold was introduced to avoid this effect. The low energy threshold was taken to be the last energy bin containing fewer events, integrated over θ^2, than the energy bin before it. The resulting threshold is shown for zenith angle 0° in Fig. A.0 and as a function of zenith angle in Fig. A.1 which is, however, not representative of the energy thresholds for typcal analysis.

The PSF widths were then fixed according to the values obtained in Fig. A.1 and the relative scale parameter for the two Gaussians, p, and the overal scale parameter N_0, were then fit at each energy and each zenith angle. This yielded high probability fits for nearly all zenith angles and energy bands covered. In the energy band $0 - 1$ TeV and zenith angle 0° is shown as an example in Fig. A.2. The relative scale parameter is then plotted as a function of energy at each zenith angle (Fig. A.2), and, for each zenith angle, p is fit as a function of energy with the form:

$$p(E_{\mathrm{TeV}}) = e^{\left(-C_0 E_{\mathrm{TeV}}^{-C_1} + C_2\right)} \tag{A.2}$$

which also yielded high probability fits. The fitted parameters are given in Table A.2. Using the appropriate fit parameters to determine the scale parameter, p, and the previous formulae for the two Gaussian widths, the full PSF is then determined.

Zenith	C_0	C_1	C_2
0°	0.126 ± 0.006	1.816 ± 0.058	-0.102 ± 0.002
20°	0.205 ± 0.006	1.439 ± 0.039	-0.102 ± 0.003
30°	0.288 ± 0.007	1.178 ± 0.031	-0.098 ± 0.004
40°	0.465 ± 0.011	0.836 ± 0.027	-0.067 ± 0.008
45°	0.676 ± 0.017	0.731 ± 0.031	-0.044 ± 0.014
50°	1.097 ± 0.026	0.757 ± 0.043	-0.063 ± 0.024
55°	2.59 ± 0.14	1.109 ± 0.088	-0.224 ± 0.038
60°	22 ± 14	1.83 ± 0.54	-0.68 ± 0.22

Table A.2: Results of the fitted C_0, C_1 and C_2 paramters to describe p, the relative scale factor as a function of energy for each zenith angle (Eqn. A.2).

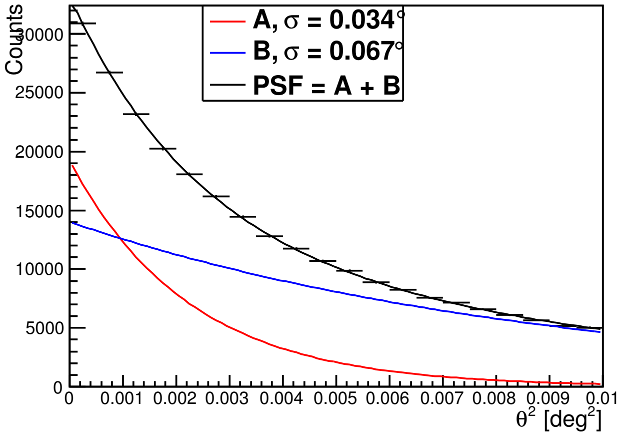

Figure A.2: Projection PSF of reconstructed MC events as taken from Figure A.0 in the energy band 0-1 TeV at zenith = 0°. This gives the widths: $A_\sigma(0-1\text{TeV}, 0°)$, $B_\sigma(0-1\text{TeV}, 0°)$. The distribution is well described by a double Gaussian. The individual guassian contributions are overlaid Red: A and Blue: B.

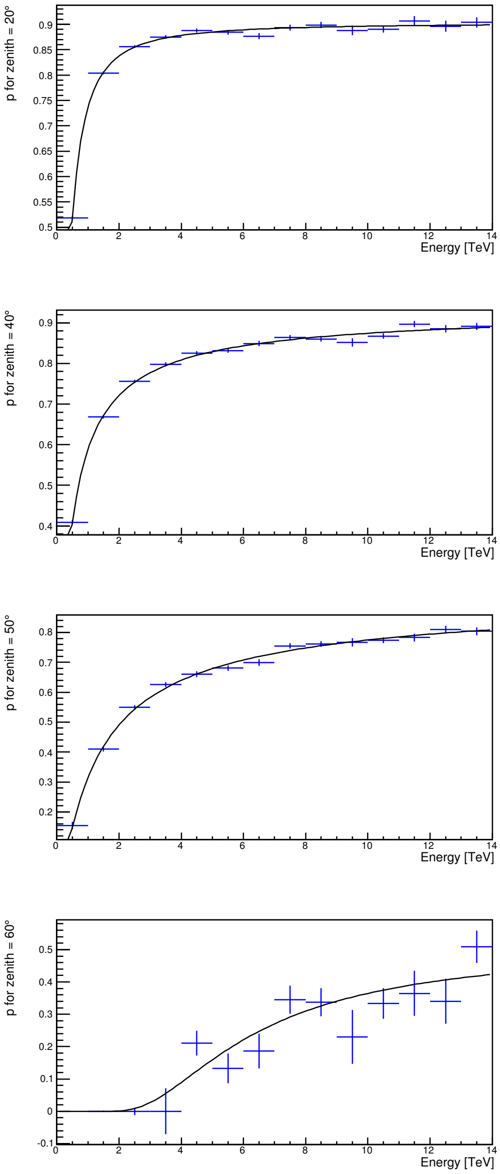

Figure A.2: The relative scale factor of the Gaussian A as a function of energy for various zenith angles. In general, at low energies the narrower Gaussian A plays a smaller role in the overal PSF, but becomes increasingly important at higher energies, typically aproaching 90% of the peak scale.

Appendix B: Astronomical Analysis Software

Over the years the field of Gamma-ray observation has advanced from being a part of cosmic ray physics to joining the ranks of astronomy. In cosmic ray physics one is generally involved with the study of individual particles, the showers they produce and methods of detection and reconstruction. These properties, when combined with large statistics and high acuracy angular reconstruction, form the basis of astronomical studies.

As the current generation of I.A.C.T.s has now reached the sensitivity requirements to detect individual sources and determine their spectra, it has become increasingly common to combine the results of these Gamma-ray observations with observations at other wavelengths, making it incumbent to incorporate standard astronomical methods and analysis tools to standardize the analysis, facilitate multi-wavelength studies and to open the science to the broader astronomical community. This includes the use of standard astronomical data and image files, such as FITS files, and the software needed to display and analyze them, such as fv, ds9, CFITSIO, etc. This appendix is an attempt to introduce the software and methods which were used in this thesis, to serve as a starting point for Gamma-ray astronomers wishing to get involved in multi-wavelength analysis.

B.2 FITS Files

Fleixible Image Transport System (FITS) is the most commonly used digital data format in astronomy. FITS file format are specifically designed for science applications and include provisions for descriptions of the data, instruments used to collect the data, calibration information, data types (such as integer or floating point) and more, within the header. The meta data in the header is stored in human readable ASCCI format at the beggining of the file, while the data and/or images are stored in binary format for efficient data storage and access. Each header consists of "card images" (80 character fixed length strings) that contain keyword/value pairs which describe the properties of the data.

B.2.1 Obtaining and Viewing Astronomical FITS Data Files

Most observatories, after observations have been completed, provide the data to the observer in the FITS file format. Typically, after a period of time the data becomes public and is placed in on-line archives which can be searched and downloaded by interested astronomers. The XMM Science Archive (`http://xmm.esac.esa.int/xsa/`), for example offers several search methods for observations that are made public after they are more than a year old. The data are offered in pre-processed pipeline format as well as raw data. Likewise, the NASA service SkyView (`http://skyview.gsfc.nasa.gov/`) offers interactive searching, display and download of pre-processed FITS image files from sky surveys in Gamma-rays (EGRET, COMPTEL), X-rays (BAT, RXTE, INTEGRAL), Infrared (2MASS, IRAS), Radio (VLA FIRST, SUMSS, VLSS, GB6, CO, nH) and more.

The free GUI program FV (FITS Viewer) can be used to inspect the contents of a FITS file including headers and data. It is provided by NASA as part of the HEASARC software package. If the FITS file contains an image, that image may be viewed with the program DS9 (`http://hea-www.harvard.edu/RD/ds9/`). DS9 allows for advanced plotting, slices, three color images, contour generation, drawing objects (using standard "region" files) and more. It has an advanced graphical user interface, but most functions can also be accessed from the command line. Below is an introduction to some of the features available, with focus on the ones used in this work.

To start ds9 with an image:

```
ds9 myimage.fits
```

Here is a list of useful command line options that can be used for added functionality:

```
-smooth radius 5 -smooth : Gaussian smoothing, 5 pixels radius
-regions myregions.reg   : display regions from file
-pan to RA DEC           : set the center of the FOV
-rgb -red red.fits -green green.fits -blue blue.fits : rgb img
-contours contoursfile.con : load a prvsly saved contours file.
```

A region file is an ASCCI text file which defines regions for display and analysis. The best way to demonstrate their use is by example (the lines which begin with # are comments):

```
# myregions.reg
# SET GLOBAL OPTIONS
global color=green font="helvetica 13 bold" edit=1

# DRAW A POINT WITH LABLE
FK5;circle 195.44 -63.093 .001  # color=green width=5
FK5;text 195.3 -63.08 {PSR J1301-6305} # color=green

# MAKE A SLICE
FK5;projection(195.66,-63.14,195.4,-63.096,.024)# color=green
```

IDL

IDL can be used to perform analysis on FITS files. This requires the purchase of IDL software license as well as installation of an additional free package, Astron (`http://idlastro.gsfc.nasa.gov/`), which has tools useful for astronomers. For example, to divide a count map by an exposure map to obtain a flux map, use the follwing:

```
;------------------------------
;Divide by an exposure map
;------------------------------
alpha=0.3
; read in 2 FITS files
count = READFITS('HESSJ1303_m1_ima_0.fits.gz',h)
exp = READFITS('HESSJ1303_m1_expv_0.fits.gz',h);
print, (size(countmap))[1]
print, size(countmap)
xsize=(size(countmap))[1];
ysize=(size(countmap))[2];
xsize=519
ysize=519
flux=fltarr(xsize,ysize);

m=alpha*max(exp)
good=where(exp gt m)
flux[good]=count[good]/exp[good]
writefits,'m1fluxmap.fits',flux,h
```

Save the above file as "exp.pro", start IDL and run it from the command line as such:

```
IDL> .run exp.pro
```

Another example of the useful analysis tools available in IDL is the kdist program, written by Chris Beaumont, which applies a Galactic rotation model to calculate the kinetic distance to a source and used in this work to find the distance to the star formation region IRAS 13010−6254:

```
;+
; NAME:
; KDIST
; ; PURPOSE:
; This function calculates the near and far kinematic distances
; for a given galactic longitude and radial velocity. The
; calculation uses the Galactic rotaion model of Brand and
; Blitz 1993, A&A, 275 : 67.
; ; CATEGORY: ; coordinate systems ;
; CALLING: ; result=KDIST( latitude, velocity, [/RADIANS])
```

```
; ; INPUTS:
; latitude: Galactic Latitude. Currently must be in the range
; [−180, ; 180] in degrees.
; ; velocity: Radial velocity in km/s
; ; KEYWORD PARAMETERS:
; RADIANS: If set, input Latitude is in radians
; DEBUG: If set, produce debugging plots / information ;
; OUTPUTS:
; The two element vector [near_distance, far_distance] in kpc.
; ; RESTRICTIONS:
; Currently only computes distances for objects in the inner
; galaxy.
; ; MODIFICATION HISTORY:
; Written by: Chris Beaumont, June 2008.
; June 23, 2008: Chng name from kinematic_distance to kdist.cnb
; June 23, 2008: Fixed bug in modding l with 2 pi. cnb
; July 17, 2008: Removed degrees keyword. Added radians. cnb
; July 17, 2008: Changed things so that, if l is a variable,
; it isn't modified
; March 18, 2009: Changed theta_0 and v_sol to reflect arxiv
; 0902.3913
; March 20, 2009: Changed minor typo in value of a1.
; Added /DEBUG keyword
;−

FUNCTION kdist, lat, velcty, radians=radians, debug = debug
compile_opt idl2
on_error, 2

if n_params() ne 2 then begin
        message,'Calling Sequence: dist=kdist(l,v,[/radians])'
endif

if ~keyword_set(radians) then l=latitude/!radeg else l=latitude
l=(l mod (2*!dpi))
if(l lt 0) then l += 2 * !dpi

if (l ge !pi/2) && (l lt 3*!pi/2) then begin
        message, 'Error −− Latitude must be acute'
endif


;− notation:
; v : rotation velocity
```

```
; vo: Solar rotation velocity
; vr: Radial velocity wrt LSR
; r : Galactocentric radius
; ro: Solar galactocentric radius
; rotation curve parameters from Brand and Blitz 1993
; v/vo = a1 * (R/Ro)^a2 + a3
; vr = sin(l) * vo * [ a1 * (r/ro)^(a2-1) + a3*(r/ro)^-1 - 1]

a1=1.0077D
a2=.0394D
a3=.0077D

;- the following are from arxiv 0902.3913 (VLBI parallax)
;- value taken from section 4, the best fit to this
;- particular roation curve
ro=8.8
vo=275.
;ro = 8.5 ; - Brand Blitz value
;vo = 225

;determine r
r = (findgen(2000) + 1) / 2000. * 2 * ro
root=sin(l)*vo*(a1*(r/ro)^(a2-1)+a3*(r/ro)^(-1)-1)-velocity
backup = root

;find the zero crossing
root*=shift(root,1)
root[0]=1

root[n_elements(root)-1]=1

hit=where(root lt 0, ct)
if keyword_set(debug) then begin
        plot, r, backup, xtitle = 'Gal center Dist (kpc)', $
        ytitle = 'Reltv radial velocity (galaxy - object)', $
        charsize = 1.8, yra = [-20, 20]
endif

if ct ne 1 then begin
        message, 'Cannot determine galactocentric distance'
endif
r=r[hit[0]]

warnmsg = 'Warning: The galactocentric distance
```

```
extrapolates the measured galactic roation curve'
if (r lt 2 || r gt 17) then $
        message, /continue, warnmsg

if keyword_set(debug) then begin
    oplot, r * [1,1], [-20, 20], color = fsc_color('crimson')
endif

rmin=ro*cos(l)
dr=sqrt(r^2-(ro*sin(l))^2)
if ~finite(dr) then $
        message, 'motion cannot be reporduced via gal rotation'

PRINT, [rmin-dr,rmin+dr]
PRINT, !dpi
PRINT, !radeg
return,[rmin-dr,rmin+dr]

end
```

This program was used in this thesis to calculate the distance to an IRAS star formation region.

B.2 XMM SAS

One year after XMM-Newton observations have been taken they become available to the public through the XMM Science Archive and can be downloaded here: `http://xmm.esac.esa.int/xsa/index.shtml`. The Science Analysis System (SAS) is a collection of tasks, scripts and libraries, designed to analyze data collected by the XMM-Newton observatory. The latest version can be downloaded here: `http://xmm.esa.int/sas/`. After installation, commands can be run from the command line to process the data. The complete official user's guide can be found here: `http://xmm.esa.int/external/xmm_user_support/documentation/sas_usg/USG.pdf`.

The "images" script can be used for standard analysis and performs filtering for periods of high background, removal of bad pixels and columns, spatial smoothing, exposure correction, merging of pn and MOS data, simplifying the analysis process, and can be downloaded here: `http://xmm.esa.int/external/xmm_science/gallery/utils/images.shtml`

Appendix C: Run lists

The run lists for the H.E.S.S. VHE Gamma-ray analysis.

```
19107 0 [_____] S PSR_B1259−63 195.7 −63.835833 0.139168145
19108 0 [_____] S PSR_B1259−63 195.7 −63.835833 1.137445580
19140 0 [_____] S PSR_B1259−63 195.7 −63.835833 0.139175878
19141 0 [_____] S PSR_B1259−63 195.7 −63.835833 1.137436088
19142 0 [_____] S PSR_B1259−63 195.7 −63.835833 0.139150541
19143 0 [_____] S PSR_B1259−63 195.7 −63.835833 1.137436612
19147 0 [_____] S PSR_B1259−63 195.7 −63.835833 0.139140922
19179 0 [_____] S PSR_B1259−63 195.7 −63.835833 0.139154934
19180 0 [_____] S PSR_B1259−63 195.7 −63.835833 1.137445135
19181 0 [_____] S PSR_B1259−63 195.7 −63.835833 0.139141280
19208 0 [_____] S PSR_B1259−63 195.7 −63.835833 1.137443872
19209 0 [_____] S PSR_B1259−63 195.7 −63.835833 0.139142713
19237 0 [_____] S PSR_B1259−63 195.7 −63.835833 0.139145245
19238 0 [_____] S PSR_B1259−63 195.7 −63.835833 1.137443071
19239 0 [_____] S PSR_B1259−63 195.7 −63.835833 0.139148019
19271 0 [_____] S PSR_B1259−63 195.7 −63.835833 0.139167669
19272 0 [_____] S PSR_B1259−63 195.7 −63.835833 1.137439457
19277 0 [_____] S PSR_B1259−63 195.7 −63.835833 0.139129427
19312 0 [_____] S PSR_B1259−63 195.7 −63.835833 1.137444477
19313 0 [_____] S PSR_B1259−63 195.7 −63.835833 0.139161805
19319 0 [_____] S PSR_B1259−63 195.7 −63.835833 0.509615058
19357 0 [_____] S PSR_B1259−63 195.7 −63.835833 0.139168165
19358 0 [_____] S PSR_B1259−63 195.7 −63.835833 1.137429641
19766 0 [_____] S PSR_B1259−63 195.7 −63.835833 1.137460957
19767 0 [_____] S PSR_B1259−63 195.7 −63.835833 0.139182202
19768 0 [_____] S PSR_B1259−63 195.7 −63.835833 1.137478129
19769 0 [_____] S PSR_B1259−63 195.7 −63.835833 0.139175647
19770 0 [_____] S PSR_B1259−63 195.7 −63.835833 1.137455224
19789 0 [_____] S PSR_B1259−63 195.7 −63.835833 1.137460957
19792 0 [_____] S PSR_B1259−63 195.7 −63.835833 1.137471109
19794 0 [_____] S PSR_B1259−63 195.7 −63.835833 0.139170038
19795 0 [_____] S PSR_B1259−63 195.7 −63.835833 1.137449842
19796 0 [_____] S PSR_B1259−63 195.7 −63.835833 0.138976096
19797 0 [_____] S PSR_B1259−63 195.7 −63.835833 1.137453930
19798 0 [_____] S PSR_B1259−63 195.7 −63.835833 0.139152241
```

19868	0	[_____]	S	PSR_B1259−63	195.7	−63.835833	1.137449151
19869	0	[_____]	S	PSR_B1259−63	195.7	−63.835833	0.139185645
19870	0	[_____]	S	PSR_B1259−63	195.7	−63.835833	1.137475099
19871	0	[_____]	S	PSR_B1259−63	195.7	−63.835833	0.139185392
19872	0	[_____]	S	PSR_B1259−63	195.7	−63.835833	1.137437316
19873	0	[_____]	S	PSR_B1259−63	195.7	−63.835833	0.139152771
19874	0	[_____]	S	PSR_B1259−63	195.7	−63.835833	1.137450990
19875	0	[_____]	S	PSR_B1259−63	195.7	−63.835833	0.139145708
19876	0	[_____]	S	PSR_B1259−63	195.7	−63.835833	1.137446546
19926	0	[_____]	S	PSR_B1259−63	195.7	−63.835833	1.137444905
19927	0	[_____]	S	PSR_B1259−63	195.7	−63.835833	0.139164160
19928	0	[_____]	S	PSR_B1259−63	195.7	−63.835833	1.137447268
19929	0	[_____]	S	PSR_B1259−63	195.7	−63.835833	0.139153489
19930	0	[_____]	S	PSR_B1259−63	195.7	−63.835833	1.137442262
19931	0	[_____]	S	PSR_B1259−63	195.7	−63.835833	0.139143783
19976	0	[_____]	S	PSR_B1259−63	195.7	−63.835833	0.139171277
19979	0	[_____]	S	PSR_B1259−63	195.7	−63.835833	1.137445406
20002	0	[_____]	S	PSR_B1259−63	195.7	−63.835833	0.139193585
20004	30	[1234]	S	PSR_B1259−63	195.7	−63.835833	1.13745646
20005	30	[1234]	S	PSR_B1259−63	195.7	−63.835833	0.13915476
20006	30	[1234]	S	PSR_B1259−63	195.7	−63.835833	1.13745757
20007	0	[_____]	S	PSR_B1259−63	195.7	−63.835833	0.139147458
20008	30	[1234]	S	PSR_B1259−63	195.7	−63.835833	1.13744322
20009	30	[1234]	S	PSR_B1259−63	195.7	−63.835833	0.13916301
20052	30	[1234]	S	PSR_B1259−63	195.7	−63.835833	0.13916480
20053	30	[1234]	S	PSR_B1259−63	195.7	−63.835833	1.13744377
20054	30	[1234]	S	PSR_B1259−63	195.7	−63.835833	0.13914187
20055	30	[1234]	S	PSR_B1259−63	195.7	−63.835833	1.13745527
20056	30	[1234]	S	PSR_B1259−63	195.7	−63.835833	0.13916194
20081	30	[1234]	S	PSR_B1259−63	195.7	−63.835833	0.13917277
20082	30	[1234]	S	PSR_B1259−63	195.7	−63.835833	1.13745320
20083	30	[1234]	S	PSR_B1259−63	195.7	−63.835833	0.13915042
20084	30	[1234]	S	PSR_B1259−63	195.7	−63.835833	1.13744431
20085	30	[1234]	S	PSR_B1259−63	195.7	−63.835833	0.13914846
20086	30	[1234]	S	PSR_B1259−63	195.7	−63.835833	1.13746994
20087	30	[1234]	S	PSR_B1259−63	195.7	−63.835833	0.13914972
20109	30	[1234]	S	PSR_B1259−63	195.7	−63.835833	0.13916614
20110	30	[1234]	S	PSR_B1259−63	195.7	−63.835833	1.13745425
20111	30	[1234]	S	PSR_B1259−63	195.7	−63.835833	0.13914591
20112	30	[1234]	S	PSR_B1259−63	195.7	−63.835833	1.13746499
20113	30	[1234]	S	PSR_B1259−63	195.7	−63.835833	0.13915466
20129	30	[1234]	S	PSR_B1259−63	195.7	−63.835833	0.13918394
20131	30	[1234]	S	PSR_B1259−63	195.7	−63.835833	1.13744520
20132	30	[1234]	S	PSR_B1259−63	195.7	−63.835833	0.13918607

```
20133 30 [1234] S PSR_B1259-63 195.7 -63.835833 1.13745058
20135 30 [1234] S PSR_B1259-63 195.7 -63.835833 0.13916361
20143 30 [1234] S PSR_B1259-63 195.7 -63.835833 0.13918698
20144 0 [_____] S PSR_B1259-63 195.7 -63.835833 1.137460957
20145 30 [1234] S PSR_B1259-63 195.7 -63.835833 0.13917671
20146 0 [_____] S PSR_B1259-63 195.7 -63.835833 1.137460957
20147 30 [1234] S PSR_B1259-63 195.7 -63.835833 0.13915120
20149 30 [1234] S PSR_B1259-63 195.7 -63.835833 1.13744759
20150 30 [1234] S PSR_B1259-63 195.7 -63.835833 0.13914948
20164 30 [1234] S PSR_B1259-63 195.7 -63.835833 0.13919543
20166 0 [_____] S PSR_B1259-63 195.7 -63.835833 1.137456453
20167 30 [1234] S PSR_B1259-63 195.7 -63.835833 0.13916986
20168 30 [1234] S PSR_B1259-63 195.7 -63.835833 1.13744798
20169 0 [_____] S PSR_B1259-63 195.7 -63.835833 0.139150903
20170 0 [_____] S PSR_B1259-63 195.7 -63.835833 1.137436630
20182 30 [1234] S PSR_B1259-63 195.7 -63.835833 0.13919962
20183 30 [1234] S PSR_B1259-63 195.7 -63.835833 1.13746571
20237 22 [12_4] S PSR_B1259-63 195.7 -63.835833 0.13919326
20239 22 [12_4] S PSR_B1259-63 195.7 -63.835833 1.13744806
20278 30 [1234] S PSR_B1259-63 195.7 -63.835833 0.13919078
20279 30 [1234] S PSR_B1259-63 195.7 -63.835833 1.13747056
20318 30 [1234] S PSR_B1259-63 195.7 -63.835833 1.13746944
20319 30 [1234] S PSR_B1259-63 195.7 -63.835833 0.13917398
20361 30 [1234] S PSR_B1259-63 195.7 -63.835833 0.13919309
20362 0 [_____] S PSR_B1259-63 195.7 -63.835833 1.137454371
20411 30 [1234] S PSR_B1259-63 195.7 -63.835833 1.13746765
20412 30 [1234] S PSR_B1259-63 195.7 -63.835833 0.13917613
20483 30 [1234] S PSR_B1259-63 195.7 -63.835833 0.13918247
20484 30 [1234] S PSR_B1259-63 195.7 -63.835833 1.13745098
20667 30 [1234] S PSR_B1259-63 195.7 -63.835833 0.13918847
20668 30 [1234] S PSR_B1259-63 195.7 -63.835833 1.13746887
20679 30 [1234] S PSR_B1259-63 195.7 -63.835833 0.68961939
20680 30 [1234] S PSR_B1259-63 195.7 -63.835833 0.70870634
20681 30 [1234] S PSR_B1259-63 195.7 -63.835833 0.13917113
20682 30 [1234] S PSR_B1259-63 195.7 -63.835833 1.13744192
20694 30 [1234] S PSR_B1259-63 195.7 -63.835833 0.13918531
20695 30 [1234] S PSR_B1259-63 195.7 -63.835833 1.13745157
20696 30 [1234] S PSR_B1259-63 195.7 -63.835833 0.80263509
20697 30 [1234] S PSR_B1259-63 195.7 -63.835833 0.83173371
20752 30 [1234] S PSR_B1259-63_North 195.70000000001 -63.3
20753 30 [1234] S PSR_B1259-63_North 195.70000000001 -63.3
20754 30 [1234] S PSR_B1259-63_North 195.70000000001 -63.3
20755 30 [1234] S PSR_B1259-63_North 195.70000000001 -63.3
20774 0 [_____] S PSR_B1259-63_North 195.70000000001 -63.33
```

```
20780 0 [____] S PSR_B1259−63_North 195.70000000001 −63.33
20799 30 [1234] S PSR_B1259−63_North 195.70000000001 −63.3
20800 30 [1234] S PSR_B1259−63_North 195.70000000001 −63.3
20805 30 [1234] S PSR_B1259−63_North 195.70000000001 −63.3
20806 14 [123_] S PSR_B1259−63_North 195.70000000001 −63.3
20809 0 [____] S PSR_B1259−63_North 195.70000000001 −63.33
20827 30 [1234] S PSR_B1259−63_North 195.70000000001 −63.3
20828 30 [1234] S PSR_B1259−63_North 195.70000000001 −63.3
20829 0 [____] S PSR_B1259−63_North 195.70000000001 −63.33
20830 30 [1234] S PSR_B1259−63_North 195.70000000001 −63.3
20851 0 [____] S PSR_B1259−63_North 195.70000000001 −63.33
20864 30 [1234] S PSR_B1259−63_North 195.70000000001 −63.3
20865 30 [1234] S PSR_B1259−63_North 195.70000000001 −63.3
20866 30 [1234] S PSR_B1259−63_North 195.70000000001 −63.3
20867 30 [1234] S PSR_B1259−63_North 195.70000000001 −63.3
20889 30 [1234] S PSR_B1259−63_North 195.70000000001 −63.3
20890 30 [1234] S PSR_B1259−63_North 195.70000000001 −63.3
21102 30 [1234] S PSR_B1259−63_North 195.70000000001 −63.3
21103 30 [1234] S PSR_B1259−63_North 195.70000000001 −63.3
21104 30 [1234] S PSR_B1259−63_North 195.70000000001 −63.3
21105 0 [____] S PSR_B1259−63_North 195.70000000001 −63.33
21106 30 [1234] S PSR_B1259−63_North 195.70000000001 −63.3
21115 30 [1234] S PSR_B1259−63_North 195.70000000001 −63.3
21117 30 [1234] S PSR_B1259−63_North 195.70000000001 −63.3
21118 0 [____] S PSR_B1259−63_North 195.70000000001 −63.33
21119 30 [1234] S PSR_B1259−63_North 195.70000000001 −63.3
21120 30 [1234] S PSR_B1259−63_North 195.70000000001 −63.3
21121 30 [1234] S PSR_B1259−63_North 195.70000000001 −63.3
21134 30 [1234] S PSR_B1259−63_North 195.70000000001 −63.3
21135 0 [____] S PSR_B1259−63_North 195.70000000001 −63.33
21136 30 [1234] S PSR_B1259−63_North 195.70000000001 −63.3
21137 30 [1234] S PSR_B1259−63_North 195.70000000001 −63.3
21138 30 [1234] S PSR_B1259−63_North 195.70000000001 −63.3
21139 30 [1234] S PSR_B1259−63_North 195.70000000001 −63.3
21155 30 [1234] S PSR_B1259−63_North 195.70000000001 −63.3
21156 30 [1234] S PSR_B1259−63_North 195.70000000001 −63.3
21157 30 [1234] S PSR_B1259−63_North 195.70000000001 −63.3
21158 30 [1234] S PSR_B1259−63_North 195.70000000001 −63.3
21177 30 [1234] S PSR_B1259−63_North 195.70000000001 −63.3
21178 30 [1234] S PSR_B1259−63_North 195.70000000001 −63.3
21179 30 [1234] S PSR_B1259−63_North 195.70000000001 −63.3
21180 0 [____] S PSR_B1259−63_North 195.70000000001 −63.33
21204 30 [1234] S PSR_B1259−63_North 195.70000000001 −63.3
21205 30 [1234] S PSR_B1259−63_North 195.70000000001 −63.3
```

```
24574 30 [1234] S PSR_B1259-63 195.7 -63.835833 0.97584402
24868 0 [_____] S PSR_B1259-63 195.7 -63.835833 0.821077088
24886 30 [1234] S G302.8+0.7 192.5766242213 -62.1713845266
24913 30 [1234] S G302.5-0.7 191.88888168392 -63.568425124
24914 30 [1234] S G305.5-0.7 198.61328724205 -63.456858299
24915 30 [1234] S G301.9-0.7 190.54185109463 -63.553102707
24927 30 [1234] S PSR_B1259-63 195.7 -63.835833 0.94109470
24929 30 [1234] S G302.2+0.7 191.29176574053 -62.162772384
24930 30 [1234] S G303.1-0.7 193.23680356608 -63.571196062
24931 30 [1234] S G303.4+0.7 193.86172293593 -62.168046752
24932 30 [1234] S G303.7-0.7 194.58435281801 -63.561396161
24933 30 [1234] S G304.0+0.7 195.14601668128 -62.152703304
24935 30 [1234] S G304.3-0.7 195.93042378024 -63.539039231
24950 30 [1234] S PSR_B1259-63 195.7 -63.835833 0.94109156
24951 30 [1234] S PSR_B1259-63 195.7 -63.835833 0.97585126
24954 30 [1234] S G304.6+0.7 196.42852615018 -62.125436528
24955 30 [1234] S G304.9-0.7 197.27377704697 -63.504193413
24956 30 [1234] S G305.2+0.7 197.70818118473 -62.086226866
24957 30 [1234] S G305.8+0.7 198.98405872322 -62.035168666
24958 30 [1234] S G306.7-0.7 201.27627564598 -63.325094647
24959 0 [_____] S G306.1-0.7 199.94786064455 -63.3971216142
24973 30 [1234] S PSR_B1259-63 195.7 -63.835833 0.97584205
24974 30 [1234] S PSR_B1259-63 195.7 -63.835833 0.94109533
24978 30 [1234] S G306.1-0.7 199.94783479111 -63.397145156
24979 30 [1234] S G306.4+0.7 200.25514253531 -61.972320440
25006 30 [1234] S G303.7-0.7 194.58439208614 -63.561393880
31378 30 [1234] S PSR_B1259-63 195.7 -63.835833 0.83175723
31379 30 [1234] S PSR_B1259-63 195.7 -63.835833 0.80260418
31419 30 [1234] S PSR_B1259-63 195.7 -63.835833 0.80260418
31420 0 [_____] S PSR_B1259-63 195.7 -63.835833 0.831727295
31461 30 [1234] S PSR_B1259-63 195.7 -63.835833 0.83175723
31462 0 [_____] S PSR_B1259-63 195.7 -63.835833 0.802604187
31502 0 [_____] S PSR_B1259-63 195.7 -63.835833 0.802604187
31503 30 [1234] S PSR_B1259-63 195.7 -63.835833 0.83175723
31574 0 [_____] S HESS_J1303-631_North 195.75166666667 -62.
31587 0 [_____] S PSR_B1259-63 195.7 -63.835833 0.831757237
31588 30 [1234] S PSR_B1259-63 195.7 -63.835833 0.80260418
31589 28 [_234] S HESS_J1303-631_North 195.75166666667 -62
31590 30 [1234] S HESS_J1303-631_North 195.75166666667 -62
31615 30 [1234] S PSR_B1259-63 195.7 -63.835833 0.80260418
31616 30 [1234] S PSR_B1259-63 195.7 -63.835833 0.83175723
31664 0 [_____] S PSR_B1259-63 195.7 -63.835833 0.831757237
31665 30 [1234] S PSR_B1259-63 195.7 -63.835833 0.80260418
31695 30 [1234] S PSR_B1259-63 195.7 -63.835833 0.80260418
```

```
31696 30 [1234] S PSR_B1259-63 195.7 -63.835833 0.83175723
31699 30 [1234] S HESS_J1303-631_North 195.75166666667 -62
31721 30 [1234] S PSR_B1259-63 195.7 -63.835833 0.83175723
31722 30 [1234] S PSR_B1259-63 195.7 -63.835833 0.80260418
31725 30 [1234] S HESS_J1303-631_North 195.75166666667 -62
38046 30 [1234] S PSR_B1259-63 195.7 -63.835833 0.97586972
38099 30 [1234] S PSR_B1259-63 195.7 -63.835833 0.94107107
38100 30 [1234] S PSR_B1259-63 195.7 -63.835833 0.97586972
38130 30 [1234] S PSR_B1259-63 195.7 -63.835833 0.94107107
38131 30 [1234] S PSR_B1259-63 195.7 -63.835833 0.97586972
38150 30 [1234] S PSR_B1259-63 195.7 -63.835833 0.94107107
38151 0 [____] S PSR_B1259-63 195.7 -63.835833 0.975869722
38170 30 [1234] S PSR_B1259-63 195.7 -63.835833 0.97586972
38171 30 [1234] S PSR_B1259-63 195.7 -63.835833 0.94107107
38216 30 [1234] S PSR_B1259-63 195.7 -63.835833 0.97586972
38217 30 [1234] S PSR_B1259-63 195.7 -63.835833 0.94107107
38252 30 [1234] S PSR_B1259-63 195.7 -63.835833 0.97586972
38253 30 [1234] S PSR_B1259-63 195.7 -63.835833 0.94107107
38679 30 [1234] S PSR_B1259-63 195.7 -63.835833 0.94107107
38680 30 [1234] S PSR_B1259-63 195.7 -63.835833 0.97586972
38706 30 [1234] S PSR_B1259-63 195.7 -63.835833 0.97586972
38707 30 [1234] S PSR_B1259-63 195.7 -63.835833 0.94107107
38741 30 [1234] S PSR_B1259-63 195.7 -63.835833 0.97586972
38742 30 [1234] S PSR_B1259-63 195.7 -63.835833 0.94107107
38743 30 [1234] S PSR_B1259-63 195.7 -63.835833 0.97586972
38769 30 [1234] S PSR_B1259-63 195.7 -63.835833 0.94107107
38770 30 [1234] S PSR_B1259-63 195.7 -63.835833 0.97586972
38771 30 [1234] S PSR_B1259-63 195.7 -63.835833 0.94107107
38772 30 [1234] S PSR_B1259-63 195.7 -63.835833 0.97586972
38818 0 [____] S PSR_B1259-63 195.7 -63.835833 0.941071073
38853 30 [1234] S PSR_B1259-63 195.7 -63.835833 0.94107107
38854 30 [1234] S PSR_B1259-63 195.7 -63.835833 0.97586972
38855 30 [1234] S PSR_B1259-63 195.7 -63.835833 0.94107107
38856 30 [1234] S PSR_B1259-63 195.7 -63.835833 0.97586972
38886 30 [1234] S PSR_B1259-63 195.7 -63.835833 0.94107107
38887 30 [1234] S PSR_B1259-63 195.7 -63.835833 0.97586972
38888 30 [1234] S PSR_B1259-63 195.7 -63.835833 0.94107107
38889 30 [1234] S PSR_B1259-63 195.7 -63.835833 0.97586972
38922 30 [1234] S PSR_B1259-63 195.7 -63.835833 0.94107107
38923 30 [1234] S PSR_B1259-63 195.7 -63.835833 0.97586972
38924 30 [1234] S PSR_B1259-63 195.7 -63.835833 0.94107107
38951 30 [1234] S PSR_B1259-63 195.7 -63.835833 0.97586972
38952 30 [1234] S PSR_B1259-63 195.7 -63.835833 0.94107107
38953 30 [1234] S PSR_B1259-63 195.7 -63.835833 0.97586972
```

```
38954 30 [1234] S PSR_B1259−63 195.7 −63.835833 0.94107107
38977 30 [1234] S PSR_B1259−63 195.7 −63.835833 0.97586972
38978 30 [1234] S PSR_B1259−63 195.7 −63.835833 0.94107107
38979 0 [____] S PSR_B1259−63 195.7 −63.835833 0.975869722
38980 0 [____] S PSR_B1259−63 195.7 −63.835833 0.941071073
39011 30 [1234] S PSR_B1259−63 195.7 −63.835833 0.97586972
39012 30 [1234] S PSR_B1259−63 195.7 −63.835833 0.94107107
39013 30 [1234] S PSR_B1259−63 195.7 −63.835833 0.97586972
39014 30 [1234] S PSR_B1259−63 195.7 −63.835833 0.94107107
39047 30 [1234] S PSR_B1259−63 195.7 −63.835833 0.97586972
39326 0 [____] S PSR_B1259−63 195.7 −63.835833 0.941071073
39342 30 [1234] S PSR_B1259−63 195.7 −63.835833 0.97586972
39369 10 [1_3_] S PSR_B1259−63 195.7 −63.835833 0.94107107
39398 30 [1234] S PSR_B1259−63 195.7 −63.835833 0.97586972
39423 30 [1234] S PSR_B1259−63 195.7 −63.835833 0.94107107
39466 30 [1234] S PSR_B1259−63 195.7 −63.835833 0.97586972
39470 30 [1234] S PSR_B1259−63 195.7 −63.835833 0.94107107
39490 30 [1234] S PSR_B1259−63 195.7 −63.835833 0.97586972
39491 30 [1234] S PSR_B1259−63 195.7 −63.835833 0.94107107
39492 22 [12_4] S PSR_B1259−63 195.7 −63.835833 0.97586972
39493 22 [12_4] S PSR_B1259−63 195.7 −63.835833 0.94107107
39494 22 [12_4] S PSR_B1259−63 195.7 −63.835833 0.97586972
39520 30 [1234] S PSR_B1259−63 195.7 −63.835833 0.94107107
39521 30 [1234] S PSR_B1259−63 195.7 −63.835833 0.97586972
39522 30 [1234] S PSR_B1259−63 195.7 −63.835833 0.94107107
39523 30 [1234] S PSR_B1259−63 195.7 −63.835833 0.97586972
39524 30 [1234] S PSR_B1259−63 195.7 −63.835833 0.94107107
39563 30 [1234] S PSR_B1259−63 195.7 −63.835833 0.97586972
39564 30 [1234] S PSR_B1259−63 195.7 −63.835833 0.94107107
39565 30 [1234] S PSR_B1259−63 195.7 −63.835833 0.97586972
39566 30 [1234] S PSR_B1259−63 195.7 −63.835833 0.94107107
39567 30 [1234] S PSR_B1259−63 195.7 −63.835833 0.97586972
39603 0 [____] S PSR_B1259−63 195.7 −63.835833 0.941071073
39604 30 [1234] S PSR_B1259−63 195.7 −63.835833 0.97586972
39605 30 [1234] S PSR_B1259−63 195.7 −63.835833 0.94107107
39606 30 [1234] S PSR_B1259−63 195.7 −63.835833 0.97586972
39607 30 [1234] S PSR_B1259−63 195.7 −63.835833 0.94107107
39650 30 [1234] S PSR_B1259−63 195.7 −63.835833 0.97586972
39651 30 [1234] S PSR_B1259−63 195.7 −63.835833 0.94107107
39652 30 [1234] S PSR_B1259−63 195.7 −63.835833 0.97586972
39653 30 [1234] S PSR_B1259−63 195.7 −63.835833 0.94107107
39675 0 [____] S PSR_B1259−63 195.7 −63.835833 0.975869722
39676 30 [1234] S PSR_B1259−63 195.7 −63.835833 0.94107107
39677 30 [1234] S PSR_B1259−63 195.7 −63.835833 0.97586972
```

39707	30	[1234]	S	PSR_B1259−63	195.7	−63.835833	0.94107107
39708	30	[1234]	S	PSR_B1259−63	195.7	−63.835833	0.97586972
39709	30	[1234]	S	PSR_B1259−63	195.7	−63.835833	0.94107107
39710	30	[1234]	S	PSR_B1259−63	195.7	−63.835833	0.97586972
39711	30	[1234]	S	PSR_B1259−63	195.7	−63.835833	0.94107107
39736	30	[1234]	S	PSR_B1259−63	195.7	−63.835833	0.97586972
39737	22	[12_4]	S	PSR_B1259−63	195.7	−63.835833	0.94107107
39774	30	[1234]	S	PSR_B1259−63	195.7	−63.835833	0.97586972
40003	30	[1234]	S	PSR_B1259−63	195.7	−63.835833	0.94107107
40004	22	[12_4]	S	PSR_B1259−63	195.7	−63.835833	0.97586972
40005	22	[12_4]	S	PSR_B1259−63	195.7	−63.835833	0.94107107
40053	30	[1234]	S	PSR_B1259−63	195.7	−63.835833	0.97586972
40054	30	[1234]	S	PSR_B1259−63	195.7	−63.835833	0.94107107
40055	30	[1234]	S	PSR_B1259−63	195.7	−63.835833	0.97586972
40073	30	[1234]	S	PSR_B1259−63	195.7	−63.835833	0.94107107
40074	30	[1234]	S	PSR_B1259−63	195.7	−63.835833	0.97586972
40075	30	[1234]	S	PSR_B1259−63	195.7	−63.835833	0.94107107
40089	30	[1234]	S	PSR_B1259−63	195.7	−63.835833	0.97586972
40110	30	[1234]	S	PSR_B1259−63	195.7	−63.835833	0.94107107
40112	30	[1234]	S	PSR_B1259−63	195.7	−63.835833	0.97586972
40113	30	[1234]	S	PSR_B1259−63	195.7	−63.835833	0.94107107
40114	30	[1234]	S	PSR_B1259−63	195.7	−63.835833	0.97586972
40115	30	[1234]	S	PSR_B1259−63	195.7	−63.835833	0.94107107
40116	30	[1234]	S	PSR_B1259−63	195.7	−63.835833	0.97586972
40117	30	[1234]	S	PSR_B1259−63	195.7	−63.835833	0.94107107
40156	30	[1234]	S	PSR_B1259−63	195.7	−63.835833	0.94107107
40157	30	[1234]	S	PSR_B1259−63	195.7	−63.835833	0.97586972
40158	30	[1234]	S	PSR_B1259−63	195.7	−63.835833	0.94107107
40159	30	[1234]	S	PSR_B1259−63	195.7	−63.835833	0.97586972
40162	30	[1234]	S	PSR_B1259−63	195.7	−63.835833	0.97586972
40163	0	[____]	S	PSR_B1259−63	195.7	−63.835833	0.975869722
40217	30	[1234]	S	PSR_B1259−63	195.7	−63.835833	0.97586972
40218	30	[1234]	S	PSR_B1259−63	195.7	−63.835833	0.94107107
40219	30	[1234]	S	PSR_B1259−63	195.7	−63.835833	0.97586972
40220	30	[1234]	S	PSR_B1259−63	195.7	−63.835833	0.94107107
40221	30	[1234]	S	PSR_B1259−63	195.7	−63.835833	0.97586972
40222	30	[1234]	S	PSR_B1259−63	195.7	−63.835833	0.94107107
40223	0	[____]	S	PSR_B1259−63	195.7	−63.835833	0.975869722
40284	0	[____]	S	PSR_B1259−63	195.7	−63.835833	0.941097242
40285	0	[____]	S	PSR_B1259−63	195.7	−63.835833	0.975869722
40286	30	[1234]	S	PSR_B1259−63	195.7	−63.835833	0.94107107
40287	30	[1234]	S	PSR_B1259−63	195.7	−63.835833	0.97586972
40288	30	[1234]	S	PSR_B1259−63	195.7	−63.835833	0.94107107
40289	30	[1234]	S	PSR_B1259−63	195.7	−63.835833	0.97586972

```
40291 0 [_____] S PSR_B1259-63 195.7 -63.835833 0.975869722
40438 30 [1234] S PSR_B1259-63 195.7 -63.835833 0.70107773
40439 30 [1234] S PSR_B1259-63 195.7 -63.835833 0.72175070
40663 30 [1234] S PSR_B1259-63 195.7 -63.835833 0.97586972
40664 30 [1234] S PSR_B1259-63 195.7 -63.835833 0.94107107
40665 0 [_____] S PSR_B1259-63 195.7 -63.835833 0.975869722
40675 0 [_____] S PSR_B1259-63 195.7 -63.835833 0.941071073
40677 0 [_____] S PSR_B1259-63 195.7 -63.835833 0.975869722
40798 30 [1234] S PSR_B1259-63 195.7 -63.835833 0.94107107
40799 0 [_____] S PSR_B1259-63 195.7 -63.835833 0.975869722
40800 30 [1234] S PSR_B1259-63 195.7 -63.835833 0.94107107
40822 30 [1234] S PSR_B1259-63 195.7 -63.835833 0.97586972
40823 30 [1234] S PSR_B1259-63 195.7 -63.835833 0.94107107
40824 30 [1234] S PSR_B1259-63 195.7 -63.835833 0.97586972
40847 0 [_____] S PSR_B1259-63 195.7 -63.835833 0.941071073
40848 0 [_____] S PSR_B1259-63 195.7 -63.835833 0.975869722
40849 0 [_____] S PSR_B1259-63 195.7 -63.835833 0.941071073
40876 0 [_____] S PSR_B1259-63 195.7 -63.835833 0.975869722
40877 0 [_____] S PSR_B1259-63 195.7 -63.835833 0.941071073
```

Bibliography

A. A. Abdo, M. Ackermann, M. Ajello, W. B. Atwood, M. Axelsson, L. Baldini, J. Ballet, D. L. Band, G. Barbiellini, D. Bastieri, and et al. Fermi/Large Area Telescope Bright Gamma-Ray Source List. *ApJS*, 183:46–66, July 2009. doi: 10.1088/0067-0049/183/1/46.

A. A. Abdo, M. Ackermann, M. Ajello, W. B. Atwood, M. Axelsson, L. Baldini, J. Ballet, G. Barbiellini, M. G. Baring, D. Bastieri, and et al. The First Fermi Large Area Telescope Catalog of Gamma-ray Pulsars. *ApJS*, 187:460–494, April 2010. doi: 10.1088/0067-0049/187/2/460.

F. Acero, F. Aharonian, A. G. Akhperjanian, G. Anton, U. Barres de Almeida, A. R. Bazer-Bachi, Y. Becherini, B. Behera, K. Bernlöhr, A. Bochow, C. Boisson, J. Bolmont, V. Borrel, J. Brucker, F. Brun, P. Brun, R. Bühler, T. Bulik, I. Büsching, T. Boutelier, P. M. Chadwick, A. Charbonnier, R. C. G. Chaves, A. Cheesebrough, L.-M. Chounet, A. C. Clapson, G. Coignet, M. Dalton, M. K. Daniel, I. D. Davids, B. Degrange, C. Deil, H. J. Dickinson, A. Djannati-Ataï, W. Domainko, L. O. ’. Drury, F. Dubois, G. Dubus, J. Dyks, M. Dyrda, K. Egberts, D. Emmanoulopoulos, P. Espigat, C. Farnier, S. Fegan, F. Feinstein, A. Fiasson, A. Förster, G. Fontaine, M. Füßling, S. Gabici, Y. A. Gallant, L. Gérard, D. Gerbig, B. Giebels, J. F. Glicenstein, B. Glück, P. Goret, D. Göring, D. Hauser, M. Hauser, S. Heinz, G. Heinzelmann, G. Henri, G. Hermann, J. A. Hinton, A. Hoffmann, W. Hofmann, P. Hofverberg, S. Hoppe, D. Horns, A. Jacholkowska, O. C. de Jager, C. Jahn, I. Jung, K. Katarzyński, U. Katz, S. Kaufmann, M. Kerschhaggl, D. Khangulyan, B. Khélifi, D. Keogh, D. Klochkov, W. Kluźniak, T. Kneiske, N. Komin, K. Kosack, R. Kossakowski, G. Lamanna, J.-P. Lenain, T. Lohse, V. Marandon, O. Martineau-Huynh, A. Marcowith, J. Masbou, D. Maurin, T. J. L. McComb, M. C. Medina, J. Méhault, R. Moderski, E. Moulin, M. Naumann-Godo, M. de Naurois, D. Nedbal, D. Nekrassov, B. Nicholas, J. Niemiec, S. J. Nolan, S. Ohm, J.-F. Olive, E. d. O. Wilhelmi, K. J. Orford, M. Ostrowski, M. Panter, M. P. Arribas, G. Pedaletti, G. Pelletier, P.-O. Petrucci, S. Pita, G. Pühlhofer, M. Punch, A. Quirrenbach, B. C. Raubenheimer, M. Raue, S. M. Rayner, O. Reimer, M. Renaud, F. Rieger, J. Ripken, L. Rob, S. Rosier-Lees, G. Rowell, B. Rudak, C. B. Rulten, J. Ruppel, V. Sahakian, A. Santangelo, R. Schlickeiser, F. M. Schöck, U. Schwanke, S. Schwarzburg, S. Schwemmer, A. Shalchi, M. Sikora, J. L. Skilton, H. Sol, Ł. Stawarz, R. Steenkamp, C. Stegmann, F. Stinzing, G. Superina, A. Szostek, P. H. Tam, J.-P. Tavernet, R. Terrier, O. Tibolla, M. Tluczykont, C. van Eldik, G. Vasileiadis, C. Venter, L. Venter, J. P. Vialle, P. Vincent, M. Vivier, H. J. Völk, F. Volpe, S. J. Wagner, M. Ward, A. A. Zdziarski, and A. Zech. Detection of Gamma Rays from a Starburst Galaxy. *Science*, 326:1080–, November 2009. doi: 10.1126/science.1178826.

F. Acero, F. Aharonian, A. G. Akhperjanian, G. Anton, U. Barres de Almeida, A. R. Bazer-Bachi, Y. Becherini, B. Behera, M. Beilicke, K. Bernlöhr, A. Bochow, C. Boisson, J. Bolmont, V. Borrel, J. Brucker, F. Brun, P. Brun, R. Bühler, T. Bulik, I. Büsching, T. Boutelier, P. M. Chadwick, A. Charbonnier, R. C. G. Chaves, A. Cheesebrough, J. Conrad, L.-M. Chounet, A. C. Clapson, G. Coignet, M. Dalton, M. K. Daniel, I. D. Davids, B. Degrange, C. Deil, H. J. Dickinson, A. Djannati-Ataï, W. Domainko, L. O'C. Drury, F. Dubois, G. Dubus, J. Dyks, M. Dyrda, K. Egberts, P. Eger, P. Espigat, L. Fallon, C. Farnier, S. Fegan, F. Feinstein, A. Fiasson, A. Förster, G. Fontaine, M. Füßling, S. Gabici, Y. A. Gallant, L. Gérard, D. Gerbig, B. Giebels, J. F. Glicenstein, B. Glück, P. Goret, D. Göring, D. Hauser, M. Hauser, S. Heinz, G. Heinzelmann, G. Henri, G. Hermann, J. A. Hinton, A. Hoffmann, W. Hofmann, P. Hofverberg, M. Holleran, S. Hoppe, D. Horns, A. Jacholkowska, O. C. de Jager, C. Jahn, I. Jung, K. Katarzyński, U. Katz, S. Kaufmann, M. Kerschhaggl, D. Khangulyan, B. Khélifi, D. Keogh, D. Klochkov, W. Kluźniak, T. Kneiske, N. Komin, K. Kosack, R. Kossakowski, G. Lamanna, M. Lemoine-Goumard, J.-P. Lenain, T. Lohse, V. Marandon, A. Marcowith, J. Masbou, D. Maurin, T. J. L. McComb, M. C. Medina, J. Méhault, R. Moderski, E. Moulin, M. Naumann-Godo, M. de Naurois, D. Nedbal, D. Nekrassov, B. Nicholas, J. Niemiec, S. J. Nolan, S. Ohm, J.-F. Olive, E. de Oña Wilhelmi, K. J. Orford, M. Ostrowski, M. Panter, M. Paz Arribas, G. Pedaletti, G. Pelletier, P.-O. Petrucci, S. Pita, G. Pühlhofer, M. Punch, A. Quirrenbach, B. C. Raubenheimer, M. Raue, S. M. Rayner, O. Reimer, M. Renaud, R. de Los Reyes, F. Rieger, J. Ripken, L. Rob, S. Rosier-Lees, G. Rowell, B. Rudak, C. B. Rulten, J. Ruppel, F. Ryde, V. Sahakian, A. Santangelo, R. Schlickeiser, F. M. Schöck, A. Schönwald, U. Schwanke, S. Schwarzburg, S. Schwemmer, A. Shalchi, I. Sushch, M. Sikora, J. L. Skilton, H. Sol, Ł. Stawarz, R. Steenkamp, C. Stegmann, F. Stinzing, G. Superina, A. Szostek, P. H. Tam, J.-P. Tavernet, R. Terrier, O. Tibolla, M. Tluczykont, C. van Eldik, G. Vasileiadis, C. Venter, L. Venter, J. P. Vialle, P. Vincent, J. Vink, M. Vivier, H. J. Völk, F. Volpe, S. Vorobiov, S. J. Wagner, M. Ward, A. A. Zdziarski, A. Zech, and HESS Collaboration. First detection of VHE γ-rays from SN 1006 by HESS. *A&A*, 516:A62+, June 2010. doi: 10.1051/0004-6361/200913916.

F. Acero, F. Aharonian, A. G. Akhperjanian, G. Anton, U. Barres de Almeida, A. R. Bazer-Bachi, Y. Becherini, B. Behera, K. Bernlöhr, A. Bochow, C. Boisson, J. Bolmont, V. Borrel, J. Brucker, F. Brun, P. Brun, R. Bühler, T. Bulik, I. Büsching, T. Boutelier, P. M. Chadwick, A. Charbonnier, R. C. G. Chaves, A. Cheesebrough, L.-M. Chounet, A. C. Clapson, G. Coignet, M. Dalton, M. K. Daniel, I. D. Davids, B. Degrange, C. Deil, H. J. Dickinson, A. Djannati-Ataï, W. Domainko, L. O. Drury, F. Dubois, G. Dubus, J. Dyks, M. Dyrda, K. Egberts, D. Emmanoulopoulos, P. Espigat, C. Farnier, F. Feinstein, A. Fiasson, A. Förster, G. Fontaine, M. Füßling, S. Gabici, Y. A. Gallant, L. Gérard, D. Gerbig, B. Giebels, J. F. Glicenstein, B. Glück,

P. Goret, D. Göring, D. Hauser, M. Hauser, S. Heinz, G. Heinzelmann, G. Henri, G. Hermann, J. A. Hinton, A. Hoffmann, W. Hofmann, M. Holleran, S. Hoppe, D. Horns, A. Jacholkowska, O. C. de Jager, C. Jahn, I. Jung, K. Katarzyński, U. Katz, S. Kaufmann, M. Kerschhaggl, D. Khangulyan, B. Khélifi, D. Keogh, D. Klochkov, W. Kluźniak, T. Kneiske, N. Komin, K. Kosack, R. Kossakowski, G. Lamanna, J.-P. Lenain, T. Lohse, V. Marandon, O. Martineau-Huynh, A. Marcowith, J. Masbou, D. Maurin, T. J. L. McComb, M. C. Medina, J. Méhault, R. Moderski, E. Moulin, M. Naumann-Godo, M. de Naurois, D. Nedbal, D. Nekrassov, B. Nicholas, J. Niemiec, S. J. Nolan, S. Ohm, J.-F. Olive, E. de Oña Wilhelmi, K. J. Orford, M. Ostrowski, M. Panter, M. Paz Arribas, G. Pedaletti, G. Pelletier, P.-O. Petrucci, S. Pita, G. Pühlhofer, M. Punch, A. Quirrenbach, B. C. Raubenheimer, M. Raue, S. M. Rayner, O. Reimer, M. Renaud, F. Rieger, J. Ripken, L. Rob, S. Rosier-Lees, G. Rowell, B. Rudak, C. B. Rulten, J. Ruppel, V. Sahakian, A. Santangelo, R. Schlickeiser, F. M. Schöck, U. Schwanke, S. Schwarzburg, S. Schwemmer, A. Shalchi, M. Sikora, J. L. Skilton, H. Sol, Ł. Stawarz, R. Steenkamp, C. Stegmann, F. Stinzing, G. Superina, A. Szostek, P. H. Tam, J.-P. Tavernet, R. Terrier, O. Tibolla, M. Tluczykont, C. van Eldik, G. Vasileiadis, C. Venter, L. Venter, J. P. Vialle, P. Vincent, M. Vivier, H. J. Völk, F. Volpe, S. J. Wagner, M. Ward, A. A. Zdziarski, A. Zech, and H.E.S.S. Collaboration. Discovery and follow-up studies of the extended, off-plane, VHE gamma-ray source HESS J1507-622. *A&A*, 525:A45+, January 2011. doi: 10.1051/0004-6361/201015187.

A. Achterberg, Y. A. Gallant, J. G. Kirk, and A. W. Guthmann. Particle acceleration by ultrarelativistic shocks: theory and simulations. *MNRAS*, 328:393–408, December 2001. doi: 10.1046/j.1365-8711.2001.04851.x.

O. Adriani, G. C. Barbarino, G. A. Bazilevskaya, R. Bellotti, M. Boezio, E. A. Bogomolov, L. Bonechi, M. Bongi, V. Bonvicini, S. Bottai, A. Bruno, F. Cafagna, D. Campana, P. Carlson, M. Casolino, G. Castellini, M. P. de Pascale, G. de Rosa, N. de Simone, V. di Felice, A. M. Galper, L. Grishantseva, P. Hofverberg, S. V. Koldashov, S. Y. Krutkov, A. N. Kvashnin, A. Leonov, V. Malvezzi, L. Marcelli, W. Menn, V. V. Mikhailov, E. Mocchiutti, S. Orsi, G. Osteria, P. Papini, M. Pearce, P. Picozza, M. Ricci, S. B. Ricciarini, M. Simon, R. Sparvoli, P. Spillantini, Y. I. Stozhkov, A. Vacchi, E. Vannuccini, G. Vasilyev, S. A. Voronov, Y. T. Yurkin, G. Zampa, N. Zampa, and V. G. Zverev. An anomalous positron abundance in cosmic rays with energies 1.5-100GeV. *Nature*, 458:607–609, April 2009. doi: 10.1038/nature07942.

F. Aharonian, A. Akhperjanian, M. Beilicke, K. Bernlöhr, H. Börst, H. Bojahr, O. Bolz, T. Coarasa, J. Contreras, J. Cortina, S. Denninghoff, V. Fonseca, M. Girma, N. Götting, G. Heinzelmann, G. Hermann, A. Heusler, W. Hofmann, D. Horns, I. Jung, R. Kankanyan, M. Kestel, J. Kettler, A. Kohnle, A. Konopelko, H. Kornmeyer, D. Kranich, H. Krawczynski, H. Lampeitl, M. Lopez, E. Lorenz, F. Lucarelli, N. Magnussen, O. Mang, H. Meyer, M. Milite, R. Mirzoyan, A. Moralejo, E. Ona, M. Panter, A. Plyasheshnikov, J. Prahl, G. Pühlhofer, G. Rauterberg, R. Reyes, W. Rhode, J. Ripken, A. Röhring, G. P. Rowell, V. Sahakian, M. Samorski, M. Schilling,

F. Schröder, M. Siems, D. Sobzynska, W. Stamm, M. Tluczykont, H. J. Völk, C. A. Wiedner, W. Wittek, Y. Uchiyama, T. Takahashi, and HEGRA Collaboration. An unidentified TeV source in the vicinity of Cygnus OB2. *A&A*, 393:L37–L40, October 2002. doi: 10.1051/0004-6361:20021171.

F. Aharonian, A. G. Akhperjanian, K.-M. Aye, A. R. Bazer-Bachi, M. Beilicke, W. Benbow, D. Berge, P. Berghaus, K. Bernlöhr, O. Bolz, C. Boisson, C. Borgmeier, F. Breitling, A. M. Brown, P. M. Chadwick, V. R. Chitnis, L.-M. Chounet, R. Cornils, L. Costamante, B. Degrange, O. C. de Jager, A. Djannati-Ataï, L. O. ’. Drury, T. Ergin, P. Espigat, F. Feinstein, P. Fleury, G. Fontaine, S. Funk, Y. A. Gallant, B. Giebels, S. Gillessen, P. Goret, J. Guy, C. Hadjichristidis, M. Hauser, G. Heinzelmann, G. Henri, G. Hermann, J. Hinton, W. Hofmann, M. Holleran, D. Horns, I. Jung, B. Khélifi, N. Komin, A. Konopelko, I. J. Latham, R. L. Gallou, M. Lemoine, A. Lemière, N. Leroy, T. Lohse, A. Marcowith, C. Masterson, T. J. L. McComb, M. de Naurois, S. J. Nolan, A. Noutsos, K. J. Orford, J. L. Osborne, M. Ouchrif, M. Panter, G. Pelletier, S. Pita, M. Pohl, G. Pühlhofer, M. Punch, B. C. Raubenheimer, M. Raue, J. Raux, S. M. Rayner, I. Redondo, A. Reimer, O. Reimer, J. Ripken, M. Rivoal, L. Rob, L. Rolland, G. Rowell, V. Sahakian, L. Sauge, S. Schlenker, R. Schlickeiser, C. Schuster, U. Schwanke, M. Siewert, H. Sol, R. Steenkamp, C. Stegmann, J.-P. Tavernet, C. G. Théoret, M. Tluczykont, D. J. van der Walt, G. Vasileiadis, P. Vincent, B. Visser, H. J. Volk, and S. J. Wagner. Calibration of cameras of the H.E.S.S. detector. *Astroparticle Physics*, 22:109–125, November 2004. doi: 10.1016/j.astropartphys.2004.06.006.

F. Aharonian, A. G. Akhperjanian, K.-M. Aye, A. R. Bazer-Bachi, M. Beilicke, W. Benbow, D. Berge, P. Berghaus, K. Bernlöhr, C. Boisson, O. Bolz, C. Borgmeier, F. Breitling, A. M. Brown, J. Bussons Gordo, P. M. Chadwick, L.-M. Chounet, R. Cornils, L. Costamante, B. Degrange, A. Djannati-Ataï, L. O’C. Drury, G. Dubus, T. Ergin, P. Espigat, F. Feinstein, P. Fleury, G. Fontaine, S. Funk, Y. A. Gallant, B. Giebels, S. Gillessen, P. Goret, C. Hadjichristidis, M. Hauser, G. Heinzelmann, G. Henri, G. Hermann, J. A. Hinton, W. Hofmann, M. Holleran, D. Horns, O. C. de Jager, I. Jung, B. Khélifi, N. Komin, A. Konopelko, I. J. Latham, R. Le Gallou, A. Lemière, M. Lemoine, N. Leroy, T. Lohse, A. Marcowith, C. Masterson, T. J. L. McComb, M. de Naurois, S. J. Nolan, A. Noutsos, K. J. Orford, J. L. Osborne, M. Ouchrif, M. Panter, G. Pelletier, S. Pita, G. Pühlhofer, M. Punch, B. C. Raubenheimer, M. Raue, J. Raux, S. M. Rayner, I. Redondo, A. Reimer, O. Reimer, J. Ripken, L. Rob, L. Rolland, G. P. Rowell, V. Sahakian, L. Saugé, S. Schlenker, R. Schlickeiser, C. Schuster, U. Schwanke, M. Siewert, H. Sol, R. Steenkamp, C. Stegmann, J.-P. Tavernet, C. G. Théoret, M. Tluczykont, D. J. van der Walt, G. Vasileiadis, P. Vincent, B. Visser, H. J. Völk, and S. J. Wagner. Upper limits to the SN1006 multi-TeV gamma-ray flux from HESS observations. *A&A*, 437:135–139, July 2005a. doi: 10.1051/0004-6361:20042522.

F. Aharonian, A. G. Akhperjanian, K.-M. Aye, A. R. Bazer-Bachi, M. Beilicke, W. Benbow, D. Berge, P. Berghaus, K. Bernlöhr, C. Boisson, O. Bolz, I. Braun, F. Breitling, A. M. Brown, J. Bussons Gordo, P. M. Chadwick, L.-M. Chounet, R. Cornils,

L. Costamante, B. Degrange, A. Djannati-Ataï, L. O'C. Drury, G. Dubus, D. Emmanoulopoulos, P. Espigat, F. Feinstein, P. Fleury, G. Fontaine, Y. Fuchs, S. Funk, Y. A. Gallant, B. Giebels, S. Gillessen, J. F. Glicenstein, P. Goret, C. Hadjichristidis, M. Hauser, G. Heinzelmann, G. Henri, G. Hermann, J. A. Hinton, W. Hofmann, M. Holleran, D. Horns, O. C. de Jager, B. Khélifi, N. Komin, A. Konopelko, I. J. Latham, R. Le Gallou, A. Lemière, M. Lemoine-Goumard, N. Leroy, T. Lohse, O. Martineau-Huynh, A. Marcowith, C. Masterson, T. J. L. McComb, M. de Naurois, S. J. Nolan, A. Noutsos, K. J. Orford, J. L. Osborne, M. Ouchrif, M. Panter, G. Pelletier, S. Pita, G. Pühlhofer, M. Punch, B. C. Raubenheimer, M. Raue, J. Raux, S. M. Rayner, I. Redondo, A. Reimer, O. Reimer, J. Ripken, L. Rob, L. Rolland, G. Rowell, V. Sahakian, L. Saugé, S. Schlenker, R. Schlickeiser, C. Schuster, U. Schwanke, M. Siewert, H. Sol, R. Steenkamp, C. Stegmann, J.-P. Tavernet, R. Terrier, C. G. Théoret, M. Tluczykont, G. Vasileiadis, C. Venter, P. Vincent, H. J. Völk, and S. J. Wagner. Discovery of extended VHE gamma-ray emission from the asymmetric pulsar wind nebula in MSH 15-52 with HESS. *A&A*, 435:L17–L20, May 2005b. doi: 10.1051/0004-6361:200500105.

F. Aharonian, A. G. Akhperjanian, K.-M. Aye, A. R. Bazer-Bachi, M. Beilicke, W. Benbow, D. Berge, P. Berghaus, K. Bernlöhr, C. Boisson, O. Bolz, I. Braun, F. Breitling, A. M. Brown, J. Bussons Gordo, P. M. Chadwick, L.-M. Chounet, R. Cornils, L. Costamante, B. Degrange, A. Djannati-Ataï, L. O'C. Drury, G. Dubus, D. Emmanoulopoulos, P. Espigat, F. Feinstein, P. Fleury, G. Fontaine, Y. Fuchs, S. Funk, Y. A. Gallant, B. Giebels, S. Gillessen, J. F. Glicenstein, P. Goret, C. Hadjichristidis, M. Hauser, G. Heinzelmann, G. Henri, G. Hermann, J. A. Hinton, W. Hofmann, M. Holleran, D. Horns, O. C. de Jager, B. Khélifi, N. Komin, A. Konopelko, I. J. Latham, R. Le Gallou, A. Lemière, M. Lemoine-Goumard, N. Leroy, T. Lohse, O. Martineau-Huynh, A. Marcowith, C. Masterson, T. J. L. McComb, M. de Naurois, S. J. Nolan, A. Noutsos, K. J. Orford, J. L. Osborne, M. Ouchrif, M. Panter, G. Pelletier, S. Pita, G. Pühlhofer, M. Punch, B. C. Raubenheimer, M. Raue, J. Raux, S. M. Rayner, I. Redondo, A. Reimer, O. Reimer, J. Ripken, L. Rob, L. Rolland, G. Rowell, V. Sahakian, L. Saugé, S. Schlenker, R. Schlickeiser, C. Schuster, U. Schwanke, M. Siewert, H. Sol, R. Steenkamp, C. Stegmann, J.-P. Tavernet, R. Terrier, C. G. Théoret, M. Tluczykont, D. J. van der Walt, G. Vasileiadis, C. Venter, P. Vincent, H. J. Völk, and S. J. Wagner. Serendipitous discovery of the unidentified extended TeV γ-ray source HESS J1303-631. *A&A*, 439:1013–1021, September 2005c. doi: 10.1051/0004-6361:20053195.

F. Aharonian, A. G. Akhperjanian, K.-M. Aye, A. R. Bazer-Bachi, M. Beilicke, W. Benbow, D. Berge, P. Berghaus, K. Bernlöhr, O. Bolz, C. Boisson, C. Borgmeier, F. Breitling, A. M. Brown, J. Bussons Gordo, P. M. Chadwick, V. R. Chitnis, L.-M. Chounet, R. Cornils, L. Costamante, B. Degrange, A. Djannati-Ataï, L. O. Drury, T. Ergin, P. Espigat, F. Feinstein, P. Fleury, G. Fontaine, S. Funk, Y. A. Gallant, B. Giebels, S. Gillessen, P. Goret, J. Guy, C. Hadjichristidis, M. Hauser, G. Heinzelmann, G. Henri, G. Hermann, J. A. Hinton, W. Hofmann, M. Holleran, D. Horns,

O. C. de Jager, Jung I., B. Khélifi, N. Komin, A. Konopelko, I. J. Latham, R. Le Gallou, M. Lemoine, A. Lemière, N. Leroy, T. Lohse, A. Marcowith, C. Masterson, T. J. L. McComb, M. de Naurois, S. J. Nolan, A. Noutsos, K. J. Orford, J. L. Osborne, M. Ouchrif, M. Panter, G. Pelletier, S. Pita, M. Pohl, G. Pühlhofer, M. Punch, B. C. Raubenheimer, M. Raue, J. Raux, S. M. Rayner, I. Redondo, A. Reimer, O. Reimer, J. Ripken, M. Rivoal, L. Rob, L. Rolland, G. Rowell, V. Sahakian, L. Saugé, S. Schlenker, R. Schlickeiser, C. Schuster, U. Schwanke, M. Siewert, H. Sol, R. Steenkamp, C. Stegmann, J.-P. Tavernet, C. G. Théoret, M. Tluczykont, D. J. van der Walt, G. Vasileiadis, P. Vincent, B. Visser, H. J. Völk, and S. J. Wagner. H.E.S.S. observations of PKS 2155-304. *A&A*, 430:865–875, February 2005d. doi: 10.1051/0004-6361:20041853.

F. Aharonian, A. G. Akhperjanian, A. R. Bazer-Bachi, M. Beilicke, W. Benbow, D. Berge, K. Bernlöhr, C. Boisson, O. Bolz, V. Borrel, I. Braun, F. Breitling, A. M. Brown, R. Bühler, I. Büsching, S. Carrigan, P. M. Chadwick, L.-M. Chounet, R. Cornils, L. Costamante, B. Degrange, H. J. Dickinson, A. Djannati-Ataï, L. O'C. Drury, G. Dubus, K. Egberts, D. Emmanoulopoulos, P. Espigat, F. Feinstein, E. Ferrero, A. Fiasson, G. Fontaine, S. Funk, S. Funk, Y. A. Gallant, B. Giebels, J. F. Glicenstein, P. Goret, C. Hadjichristidis, D. Hauser, M. Hauser, G. Heinzelmann, G. Henri, G. Hermann, J. A. Hinton, W. Hofmann, M. Holleran, D. Horns, A. Jacholkowska, O. C. de Jager, B. Khélifi, N. Komin, A. Konopelko, K. Kosack, I. J. Latham, R. Le Gallou, A. Lemière, M. Lemoine-Goumard, T. Lohse, J. M. Martin, O. Martineau-Huynh, A. Marcowith, C. Masterson, T. J. L. McComb, M. de Naurois, D. Nedbal, S. J. Nolan, A. Noutsos, K. J. Orford, J. L. Osborne, M. Ouchrif, M. Panter, G. Pelletier, S. Pita, G. Pühlhofer, M. Punch, B. C. Raubenheimer, M. Raue, S. M. Rayner, A. Reimer, O. Reimer, J. Ripken, L. Rob, L. Rolland, G. Rowell, V. Sahakian, L. Saugé, S. Schlenker, R. Schlickeiser, U. Schwanke, H. Sol, D. Spangler, F. Spanier, R. Steenkamp, C. Stegmann, G. Superina, J.-P. Tavernet, R. Terrier, C. G. Théoret, M. Tluczykont, C. van Eldik, G. Vasileiadis, C. Venter, P. Vincent, H. J. Völk, S. J. Wagner, and M. Ward. Observations of the Crab nebula with HESS. *A&A*, 457:899–915, October 2006a. doi: 10.1051/0004-6361:20065351.

F. Aharonian, A. G. Akhperjanian, A. R. Bazer-Bachi, M. Beilicke, W. Benbow, D. Berge, K. Bernlöhr, C. Boisson, O. Bolz, V. Borrel, I. Braun, F. Breitling, A. M. Brown, R. Bühler, I. Büsching, S. Carrigan, P. M. Chadwick, L.-M. Chounet, R. Cornils, L. Costamante, B. Degrange, H. J. Dickinson, A. Djannati-Ataï, L. O. ’. Drury, G. Dubus, K. Egberts, D. Emmanoulopoulos, P. Espigat, F. Feinstein, E. Ferrero, A. Fiasson, G. Fontaine, S. Funk, S. Funk, Y. A. Gallant, B. Giebels, J. F. Glicenstein, P. Goret, C. Hadjichristidis, D. Hauser, M. Hauser, G. Heinzelmann, G. Henri, G. Hermann, J. A. Hinton, W. Hofmann, M. Holleran, D. Horns, A. Jacholkowska, O. C. de Jager, B. Khélifi, N. Komin, A. Konopelko, K. Kosack, I. J. Latham, R. Le Gallou, A. Lemière, M. Lemoine-Goumard, T. Lohse, J. M. Martin, O. Martineau-Huynh, A. Marcowith, C. Masterson, T. J. L. McComb, M. de Naurois, D. Nedbal, S. J. Nolan, A. Noutsos, K. J. Orford, J. L. Osborne, M. Ouchrif, M. Panter, G. Pelletier, S. Pita, G. Pühlhofer, M. Punch, B. C. Raubenheimer, M. Raue, S. M. Rayner, A. Reimer, O. Reimer, J. Ripken, L. Rob, L. Rolland, G. Rowell, V. Sahakian, L. Saugé, S. Schlenker, R. Schlickeiser, U. Schwanke, H. Sol, D. Spangler, F. Spanier, R. Steenkamp, C. Stegmann, G. Superina, J.-P. Tavernet, R. Terrier, C. G. Théoret, M. Tluczykont, C. van Eldik, G. Vasileiadis, C. Venter, P. Vincent, H. J. Völk, S. J. Wagner, and M. Ward. HESS Observations of the Galactic Center Region and Their Possible Dark Matter Interpretation. *Physical Review Letters*, 97 (22):221102–+, December 2006b. doi: 10.1103/PhysRevLett.97.221102.

F. Aharonian, A. G. Akhperjanian, A. R. Bazer-Bachi, M. Beilicke, W. Benbow, D. Berge, K. Bernlöhr, C. Boisson, O. Bolz, V. Borrel, I. Braun, F. Breitling, A. M. Brown, R. Bühler, I. Büsching, S. Carrigan, P. M. Chadwick, L.-M. Chounet, R. Cornils, L. Costamante, B. Degrange, H. J. Dickinson, A. Djannati-Ataï, L. O'C. Drury, G. Dubus, K. Egberts, D. Emmanoulopoulos, B. Epinat, P. Espigat, F. Feinstein, E. Ferrero, G. Fontaine, S. Funk, S. Funk, Y. A. Gallant, B. Giebels, J. F. Glicenstein, P. Goret, C. Hadjichristidis, D. Hauser, M. Hauser, G. Heinzelmann, G. Henri, G. Hermann, J. A. Hinton, W. Hofmann, M. Holleran, D. Horns, A. Jacholkowska, O. C. de Jager, B. Khélifi, N. Komin, A. Konopelko, I. J. Latham, R. Le Gallou, A. Lemière, M. Lemoine-Goumard, T. Lohse, J. M. Martin, O. Martineau-Huynh, A. Marcowith, C. Masterson, T. J. L. McComb, M. de Naurois, D. Nedbal, S. J. Nolan, A. Noutsos, K. J. Orford, J. L. Osborne, M. Ouchrif, M. Panter, G. Pelletier, S. Pita, G. Pühlhofer, M. Punch, B. C. Raubenheimer, M. Raue, S. M. Rayner, A. Reimer, O. Reimer, J. Ripken, L. Rob, L. Rolland, G. Rowell, V. Sahakian, L. Saugé, S. Schlenker, R. Schlickeiser, U. Schwanke, H. Sol, D. Spangler, F. Spanier, R. Steenkamp, C. Stegmann, G. Superina, J.-P. Tavernet, R. Terrier, C. G. Théoret, M. Tluczykont, C. van Eldik, G. Vasileiadis, C. Venter, P. Vincent, H. J. Völk, S. J. Wagner, and M. Ward. First detection of a VHE gamma-ray spectral maximum from a cosmic source: HESS discovery of the Vela X nebula. *A&A*, 448:L43–L47, March 2006c. doi: 10.1051/0004-6361:200600014.

F. Aharonian, A. G. Akhperjanian, A. R. Bazer-Bachi, M. Beilicke, W. Benbow, D. Berge, K. Bernlöhr, C. Boisson, O. Bolz, V. Borrel, I. Braun, F. Breitling, A. M. Brown, R. Bühler, I. Büsching, S. Carrigan, P. M. Chadwick, L.-M. Chounet, R. Cornils, L. Costamante, B. Degrange, H. J. Dickinson, A. Djannati-Ataï, L. O'C. Drury, G. Dubus, K. Egberts, D. Emmanoulopoulos, P. Espigat, F. Feinstein, E. Ferrero, A. Fiasson, G. Fontaine, S. Funk, S. Funk, Y. A. Gallant, B. Giebels, J. F. Glicenstein, P. Goret, C. Hadjichristidis, D. Hauser, M. Hauser, G. Heinzelmann, G. Henri, G. Hermann, J. A. Hinton, W. Hofmann, M. Holleran, D. Horns, A. Jacholkowska, O. C. de Jager, B. Khélifi, N. Komin, A. Konopelko, K. Kosack, I. J. Latham, R. Le Gallou, A. Lemière, M. Lemoine-Goumard, T. Lohse, J. M. Martin, O. Martineau-Huynh, A. Marcowith, C. Masterson, T. J. L. McComb, M. de Naurois, D. Nedbal, S. J. Nolan, A. Noutsos, K. J. Orford, J. L. Osborne, M. Ouchrif, M. Panter, G. Pelletier, S. Pita, G. Pühlhofer, M. Punch, B. C. Raubenheimer, M. Raue, S. M. Rayner, A. Reimer, O. Reimer, J. Ripken, L. Rob, L. Rolland, G. Rowell,

V. Sahakian, L. Saugé, S. Schlenker, R. Schlickeiser, U. Schwanke, H. Sol, D. Spangler, F. Spanier, R. Steenkamp, C. Stegmann, G. Superina, J.-P. Tavernet, R. Terrier, C. G. Théoret, M. Tluczykont, C. van Eldik, G. Vasileiadis, C. Venter, P. Vincent, H. J. Völk, S. J. Wagner, and M. Ward. Observations of the Crab nebula with HESS. *A&A*, 457:899–915, October 2006d. doi: 10.1051/0004-6361:20065351.

F. Aharonian, A. G. Akhperjanian, A. R. Bazer-Bachi, M. Beilicke, W. Benbow, D. Berge, K. Bernlöhr, C. Boisson, O. Bolz, V. Borrel, I. Braun, F. Breitling, A. M. Brown, P. M. Chadwick, L.-M. Chounet, R. Cornils, L. Costamante, B. Degrange, H. J. Dickinson, A. Djannati-Ataï, L. O. Drury, G. Dubus, D. Emmanoulopoulos, P. Espigat, F. Feinstein, G. Fontaine, Y. Fuchs, S. Funk, Y. A. Gallant, B. Giebels, S. Gillessen, J. F. Glicenstein, P. Goret, C. Hadjichristidis, M. Hauser, G. Heinzelmann, G. Henri, G. Hermann, J. A. Hinton, W. Hofmann, M. Holleran, D. Horns, A. Jacholkowska, O. C. de Jager, B. Khélifi, N. Komin, A. Konopelko, I. J. Latham, R. Le Gallou, A. Lemière, M. Lemoine-Goumard, N. Leroy, T. Lohse, J. M. Martin, O. Martineau-Huynh, A. Marcowith, C. Masterson, T. J. L. McComb, M. de Naurois, S. J. Nolan, A. Noutsos, K. J. Orford, J. L. Osborne, M. Ouchrif, M. Panter, G. Pelletier, S. Pita, G. Pühlhofer, M. Punch, B. C. Raubenheimer, M. Raue, J. Raux, S. M. Rayner, A. Reimer, O. Reimer, J. Ripken, L. Rob, L. Rolland, G. Rowell, V. Sahakian, L. Saugé, S. Schlenker, R. Schlickeiser, C. Schuster, U. Schwanke, M. Siewert, H. Sol, D. Spangler, R. Steenkamp, C. Stegmann, J.-P. Tavernet, R. Terrier, C. G. Théoret, M. Tluczykont, G. Vasileiadis, C. Venter, P. Vincent, H. J. Völk, and S. J. Wagner. The H.E.S.S. Survey of the Inner Galaxy in Very High Energy Gamma Rays. *ApJ*, 636:777–797, January 2006e. doi: 10.1086/498013.

F. Aharonian, A. G. Akhperjanian, A. R. Bazer-Bachi, M. Beilicke, W. Benbow, D. Berge, K. Bernlöhr, C. Boisson, O. Bolz, V. Borrel, I. Braun, A. M. Brown, R. Bühler, I. Büsching, S. Carrigan, P. M. Chadwick, L.-M. Chounet, R. Cornils, L. Costamante, B. Degrange, H. J. Dickinson, A. Djannati-Ataï, L. O'C. Drury, G. Dubus, K. Egberts, D. Emmanoulopoulos, P. Espigat, F. Feinstein, E. Ferrero, A. Fiasson, G. Fontaine, S. Funk, S. Funk, M. Füßling, Y. A. Gallant, B. Giebels, J. F. Glicenstein, P. Goret, C. Hadjichristidis, D. Hauser, M. Hauser, G. Heinzelmann, G. Henri, G. Hermann, J. A. Hinton, A. Hoffmann, W. Hofmann, M. Holleran, D. Horns, A. Jacholkowska, O. C. de Jager, E. Kendziorra, B. Khélifi, N. Komin, A. Konopelko, K. Kosack, I. J. Latham, R. Le Gallou, A. Lemière, M. Lemoine-Goumard, T. Lohse, J. M. Martin, O. Martineau-Huynh, A. Marcowith, C. Masterson, G. Maurin, T. J. L. McComb, E. Moulin, M. de Naurois, D. Nedbal, S. J. Nolan, A. Noutsos, K. J. Orford, J. L. Osborne, M. Ouchrif, M. Panter, G. Pelletier, S. Pita, G. Pühlhofer, M. Punch, B. C. Raubenheimer, M. Raue, S. M. Rayner, A. Reimer, O. Reimer, J. Ripken, L. Rob, L. Rolland, G. Rowell, V. Sahakian, A. Santangelo, L. Saugé, S. Schlenker, R. Schlickeiser, R. Schröder, U. Schwanke, S. Schwarzburg, A. Shalchi, H. Sol, D. Spangler, F. Spanier, R. Steenkamp, C. Stegmann, G. Superina, J.-P. Tavernet, R. Terrier, C. G. Théoret, M. Tluczykont, C. van Eldik, G. Vasileiadis, C. Venter, P. Vincent, H. J. Völk, S. J. Wagner, and M. Ward. Energy dependent γ-ray morphology in the pulsar wind nebula HESS J1825-137. *A&A*, 460:365–374, December 2006f. doi: 10.1051/0004-6361:20065546.

F. Aharonian, A. G. Akhperjanian, A. R. Bazer-Bachi, M. Beilicke, W. Benbow, D. Berge, K. Bernlöhr, C. Boisson, O. Bolz, V. Borrel, I. Braun, A. M. Brown, R. Bühler, I. Büsching, S. Carrigan, P. M. Chadwick, L.-M. Chounet, R. Cornils, L. Costamante, B. Degrange, H. J. Dickinson, A. Djannati-Ataï, L. O'C. Drury, G. Dubus, K. Egberts, D. Emmanoulopoulos, P. Espigat, F. Feinstein, E. Ferrero, A. Fiasson, G. Fontaine, S. Funk, S. Funk, M. Füßling, Y. A. Gallant, B. Giebels, J. F. Glicenstein, P. Goret, C. Hadjichristidis, D. Hauser, M. Hauser, G. Heinzelmann, G. Henri, G. Hermann, J. A. Hinton, A. Hoffmann, W. Hofmann, M. Holleran, D. Horns, A. Jacholkowska, O. C. de Jager, E. Kendziorra, B. Khélifi, N. Komin, A. Konopelko, K. Kosack, I. J. Latham, R. Le Gallou, A. Lemière, M. Lemoine-Goumard, T. Lohse, J. M. Martin, O. Martineau-Huynh, A. Marcowith, C. Masterson, G. Maurin, T. J. L. McComb, M. de Naurois, D. Nedbal, S. J. Nolan, A. Noutsos, K. J. Orford, J. L. Osborne, M. Ouchrif, M. Panter, G. Pelletier, S. Pita, G. Pühlhofer, M. Punch, B. C. Raubenheimer, M. Raue, S. M. Rayner, A. Reimer, O. Reimer, J. Ripken, L. Rob, L. Rolland, G. Rowell, V. Sahakian, A. Santangelo, L. Saugé, S. Schlenker, R. Schlickeiser, R. Schröder, U. Schwanke, S. Schwarzburg, A. Shalchi, H. Sol, D. Spangler, F. Spanier, R. Steenkamp, C. Stegmann, G. Superina, J.-P. Tavernet, R. Terrier, C. G. Théoret, M. Tluczykont, C. van Eldik, G. Vasileiadis, C. Venter, P. Vincent, H. J. Völk, S. J. Wagner, and M. Ward. Discovery of the two "wings" of the Kookaburra complex in VHE γ-rays with HESS. *A&A*, 456:245–251, September 2006g. doi: 10.1051/0004-6361:20065511.

F. Aharonian, A. G. Akhperjanian, U. Barres de Almeida, A. R. Bazer-Bachi, B. Behera, M. Beilicke, W. Benbow, K. Bernlöhr, C. Boisson, O. Bolz, V. Borrel, I. Braun, E. Brion, A. M. Brown, R. Bühler, T. Bulik, I. Büsching, T. Boutelier, S. Carrigan, P. M. Chadwick, L.-M. Chounet, A. C. Clapson, G. Coignet, R. Cornils, L. Costamante, M. Dalton, B. Degrange, H. J. Dickinson, A. Djannati-Ataï, W. Domainko, L. O'C. Drury, F. Dubois, G. Dubus, J. Dyks, K. Egberts, D. Emmanoulopoulos, P. Espigat, C. Farnier, F. Feinstein, A. Fiasson, A. Förster, G. Fontaine, S. Funk, M. Füßling, Y. A. Gallant, B. Giebels, J. F. Glicenstein, B. Glück, P. Goret, C. Hadjichristidis, D. Hauser, M. Hauser, G. Heinzelmann, G. Henri, G. Hermann, J. A. Hinton, A. Hoffmann, W. Hofmann, M. Holleran, S. Hoppe, D. Horns, A. Jacholkowska, O. C. de Jager, I. Jung, K. Katarzyński, E. Kendziorra, M. Kerschhaggl, B. Khélifi, D. Keogh, N. Komin, K. Kosack, G. Lamanna, I. J. Latham, A. Lemière, M. Lemoine-Goumard, J.-P. Lenain, T. Lohse, J. M. Martin, O. Martineau-Huynh, A. Marcowith, C. Masterson, D. Maurin, G. Maurin, T. J. L. McComb, R. Moderski, E. Moulin, M. de Naurois, D. Nedbal, S. J. Nolan, S. Ohm, J.-P. Olive, E. de Oña Wilhelmi, K. J. Orford, J. L. Osborne, M. Ostrowski, M. Panter, G. Pedaletti, G. Pelletier, P.-O. Petrucci, S. Pita, G. Pühlhofer, M. Punch, S. Ranchon, B. C. Raubenheimer, M. Raue, S. M. Rayner, M. Renaud, J. Ripken, L. Rob, L. Rolland, S. Rosier-Lees, G. Rowell, B. Rudak, J. Ruppel, V. Sahakian, A. Santangelo, R. Schlickeiser, F. Schöck,

R. Schröder, U. Schwanke, S. Schwarzburg, S. Schwemmer, A. Shalchi, H. Sol, D. Spangler, Ł. Stawarz, R. Steenkamp, C. Stegmann, G. Superina, P. H. Tam, J.-P. Tavernet, R. Terrier, C. van Eldik, G. Vasileiadis, C. Venter, J. P. Vialle, P. Vincent, M. Vivier, H. J. Völk, F. Volpe, S. J. Wagner, M. Ward, A. A. Zdziarski, and A. Zech. New constraints on the mid-IR EBL from the HESS discovery of VHE γ-rays from 1ES 0229+200. *A&A*, 475:L9–L13, November 2007. doi: 10.1051/0004-6361:20078462.

F. Aharonian, A. G. Akhperjanian, U. Barres de Almeida, A. R. Bazer-Bachi, B. Behera, M. Beilicke, W. Benbow, K. Bernlöhr, C. Boisson, O. Bolz, V. Borrel, I. Braun, E. Brion, A. M. Brown, R. Bühler, T. Bulik, I. Büsching, T. Boutelier, S. Carrigan, P. M. Chadwick, L.-M. Chounet, A. C. Clapson, G. Coignet, R. Cornils, L. Costamante, M. Dalton, B. Degrange, H. J. Dickinson, A. Djannati-Ataï, W. Domainko, L. O. Drury, F. Dubois, G. Dubus, J. Dyks, K. Egberts, D. Emmanoulopoulos, P. Espigat, C. Farnier, F. Feinstein, A. Fiasson, A. Förster, G. Fontaine, S. Funk, M. Füßling, Y. A. Gallant, B. Giebels, J. F. Glicenstein, B. Glück, P. Goret, C. Hadjichristidis, D. Hauser, M. Hauser, G. Heinzelmann, G. Henri, G. Hermann, J. A. Hinton, A. Hoffmann, W. Hofmann, M. Holleran, S. Hoppe, D. Horns, A. Jacholkowska, O. C. de Jager, I. Jung, K. Katarzyński, E. Kendziorra, M. Kerschhaggl, B. Khélifi, D. Keogh, N. Komin, K. Kosack, G. Lamanna, I. J. Latham, A. Lemière, M. Lemoine-Goumard, J.-P. Lenain, T. Lohse, J. M. Martin, O. Martineau-Huynh, A. Marcowith, C. Masterson, D. Maurin, G. Maurin, T. J. L. McComb, R. Moderski, E. Moulin, M. de Naurois, D. Nedbal, S. J. Nolan, S. Ohm, J.-P. Olive, E. de Oña Wilhelmi, K. J. Orford, J. L. Osborne, M. Ostrowski, M. Panter, G. Pedaletti, G. Pelletier, P.-O. Petrucci, S. Pita, G. Pühlhofer, M. Punch, S. Ranchon, B. C. Raubenheimer, M. Raue, S. M. Rayner, M. Renaud, J. Ripken, L. Rob, L. Rolland, S. Rosier-Lees, G. Rowell, B. Rudak, J. Ruppel, V. Sahakian, A. Santangelo, R. Schlickeiser, F. Schöck, R. Schröder, U. Schwanke, S. Schwarzburg, S. Schwemmer, A. Shalchi, H. Sol, D. Spangler, Ł. Stawarz, R. Steenkamp, C. Stegmann, G. Superina, P. H. Tam, J.-P. Tavernet, R. Terrier, C. van Eldik, G. Vasileiadis, C. Venter, J. P. Vialle, P. Vincent, M. Vivier, H. J. Völk, F. Volpe, S. J. Wagner, M. Ward, A. A. Zdziarski, and A. Zech. HESS very-high-energy gamma-ray sources without identified counterparts. *A&A*, 477:353–363, January 2008. doi: 10.1051/0004-6361:20078516.

F. Aharonian, A. G. Akhperjanian, G. Anton, U. Barres de Almeida, A. R. Bazer-Bachi, Y. Becherini, B. Behera, K. Bernlöhr, A. Bochow, C. Boisson, J. Bolmont, V. Borrel, J. Brucker, F. Brun, P. Brun, R. Bühler, T. Bulik, I. Büsching, T. Boutelier, P. M. Chadwick, A. Charbonnier, R. C. G. Chaves, A. Cheesebrough, L.-M. Chounet, A. C. Clapson, G. Coignet, M. Dalton, M. K. Daniel, I. D. Davids, B. Degrange, C. Deil, H. J. Dickinson, A. Djannati-Ataï, W. Domainko, L. O'C. Drury, F. Dubois, G. Dubus, J. Dyks, M. Dyrda, K. Egberts, D. Emmanoulopoulos, P. Espigat, C. Farnier, F. Feinstein, A. Fiasson, A. Förster, G. Fontaine, M. Füßling, S. Gabici, Y. A. Gallant, L. Gérard, D. Gerbig, B. Giebels, J. F. Glicenstein, B. Glück, P. Goret, D. Göring, D. Hauser, M. Hauser, S. Heinz, G. Heinzelmann, G. Henri, G. Hermann, J. A. Hinton, A. Hoffmann, W. Hofmann, M. Holleran, S. Hoppe, D. Horns, A. Jacholkowska,

O. C. de Jager, C. Jahn, I. Jung, K. Katarzyński, U. Katz, S. Kaufmann, M. Kerschhaggl, D. Khangulyan, B. Khélifi, D. Keogh, D. Klochkov, W. Kluźniak, T. Kneiske, N. Komin, K. Kosack, R. Kossakowski, G. Lamanna, J.-P. Lenain, T. Lohse, V. Marandon, O. Martineau-Huynh, A. Marcowith, J. Masbou, D. Maurin, T. J. L. McComb, M. C. Medina, R. Moderski, E. Moulin, M. Naumann-Godo, M. de Naurois, D. Nedbal, D. Nekrassov, B. Nicholas, J. Niemiec, S. J. Nolan, S. Ohm, J.-F. Olive, E. de Oña Wilhelmi, K. J. Orford, M. Ostrowski, M. Panter, M. Paz Arribas, G. Pedaletti, G. Pelletier, P.-O. Petrucci, S. Pita, G. Pühlhofer, M. Punch, A. Quirrenbach, B. C. Raubenheimer, M. Raue, S. M. Rayner, M. Renaud, F. Rieger, J. Ripken, L. Rob, S. Rosier-Lees, G. Rowell, B. Rudak, C. B. Rulten, J. Ruppel, V. Sahakian, A. Santangelo, R. Schlickeiser, F. M. Schöck, U. Schwanke, S. Schwarzburg, S. Schwemmer, A. Shalchi, M. Sikora, J. L. Skilton, H. Sol, D. Spangler, Ł. Stawarz, R. Steenkamp, C. Stegmann, F. Stinzing, G. Superina, A. Szostek, P. H. Tam, J.-P. Tavernet, R. Terrier, O. Tibolla, M. Tluczykont, C. van Eldik, G. Vasileiadis, C. Venter, L. Venter, J. P. Vialle, P. Vincent, M. Vivier, H. J. Völk, F. Volpe, S. J. Wagner, M. Ward, A. A. Zdziarski, and A. Zech. Very high energy γ-ray observations of the binary PSR B1259-63/SS2883 around the 2007 Periastron . *A&A*, 507:389–396, November 2009. doi: 10.1051/0004-6361/200912339.

F. A. Aharonian and S. V. Bogovalov. Exploring physics of rotation powered pulsars with sub-10 GeV imaging atmospheric Cherenkov telescopes. *New A*, 8:85–103, February 2003. doi: 10.1016/S1384-1076(02)00200-2.

R. Aloisio, V. Berezinsky, P. Blasi, and S. Ostapchenko. Signatures of the transition from galactic to extragalactic cosmic rays. *Phys. Rev. D*, 77(2):025007–+, January 2008. doi: 10.1103/PhysRevD.77.025007.

L. A. Anchordoqui, J. F. Beacom, H. Goldberg, S. Palomares-Ruiz, and T. J. Weiler. TeV γ rays and neutrinos from photodisintegration of nuclei in Cygnus OB2. *Phys. Rev. D*, 75(6):063001–+, March 2007a. doi: 10.1103/PhysRevD.75.063001.

L. A. Anchordoqui, J. F. Beacom, H. Goldberg, S. Palomares-Ruiz, and T. J. Weiler. TeV γ Rays from Photodisintegration and Daughter Deexcitation of Cosmic-Ray Nuclei. *Physical Review Letters*, 98(12):121101–+, March 2007b. doi: 10.1103/PhysRevLett.98.121101.

R. Atkins, W. Benbow, D. Berley, E. Blaufuss, J. Bussons, D. G. Coyne, T. De Young, B. L. Dingus, D. E. Dorfan, R. W. Ellsworth, L. Fleysher, R. Fleysher, G. Gisler, M. M. Gonzalez, J. A. Goodman, T. J. Haines, E. Hays, C. M. Hoffman, L. A. Kelley, C. P. Lansdell, J. T. Linnemann, J. E. McEnery, R. S. Miller, A. I. Mincer, M. F. Morales, P. Nemethy, D. Noyes, J. M. Ryan, F. W. Samuelson, A. Shoup, G. Sinnis, A. J. Smith, G. W. Sullivan, D. A. Williams, S. Westerhoff, M. E. Wilson, X. W. Xu, and G. B. Yodh. TeV Gamma-Ray Survey of the Northern Hemisphere Sky Using the Milagro Observatory. *ApJ*, 608:680–685, June 2004. doi: 10.1086/420880.

A. Atoyan, J. Buckley, and H. Krawczynski. A Gamma-Ray Burst Remnant in Our Galaxy: HESS J1303-631. *ApJ*, 642:L153–L156, May 2006. doi: 10.1086/504712.

C. Baixeras, D. Bastieri, C. Bigongiari, O. Blanch, G. Blanchot, R. Bock, T. Bretz, A. Chilingarian, J. A. Coarasa, E. Colombo, J. C. Contreras, D. Corti, J. Cortina, C. Domingo, E. Domingo, D. Ferenc, E. Fernández, J. Flix, V. Fonseca, L. Font, N. Galante, M. Gaug, M. Garczarczyk, J. Gebauer, M. Giller, F. Goebel, T. Hengstebeck, P. Jacone, O. C. de Jager, O. Kalekin, M. Kestel, T. Kneiske, A. Laille, M. López, J. López, E. Lorenz, K. Mannheim, M. Mariotti, M. Martínez, K. Mase, M. Merck, M. Meucci, L. Miralles, R. Mirzoyan, A. Moralejo, E. O. Wilhelmi, R. Orduña, D. Paneque, R. Paoletti, D. Pascoli, N. Pavel, R. Pegna, L. Peruzzo, A. Piccioli, A. Roberts, R. Reyes, A. Saggion, A. Sánchez, P. Sartori, V. Scalzotto, T. Schweizer, A. Sillanpaa, D. Sobczynska, A. Stamerra, A. Stepanian, R. Stiehler, L. Takalo, M. Teshima, N. Tonello, A. Torres, N. Turini, V. Vitale, S. Volkov, R. M. Wagner, T. Wibig, and W. Wittek. Commissioning and first tests of the MAGIC telescope. *Nuclear Instruments and Methods in Physics Research A*, 518:188–192, February 2004. doi: 10.1016/j.nima.2003.10.057.

A. Bamba, Y. Fukazawa, J. S. Hiraga, J. P. Hughes, H. Katagiri, M. Kokubun, K. Koyama, E. Miyata, T. Mizuno, K. Mori, H. Nakajima, M. Ozaki, R. Petre, H. Takahashi, T. Takahashi, T. Tanaka, Y. Terada, Y. Uchiyama, S. Watanabe, and H. Yamaguchi. Suzaku Wide-Band Observations of SN1006. *PASJ*, 60:153–+, January 2008.

K. Beck. *Extreme Programming Explained: Embrace Change.* Addison-Wesley, 1st edition, 1999a.

K. Beck. *Extreme Programming Explained: Embrace Change.* Addison-Wesley, Anschrift des Verlages, 1st edition, 1999b. ISBN 3-540-21059-8. URL `http://www.springeronline.com/sgw/cda/frontpage/0,11855,4-186-72-35393%865-0,00.html`. Eigene Anmerkungen.

W. Becker, M. Kramer, A. Jessner, R. E. Taam, J. J. Jia, K. S. Cheng, R. Mignani, A. Pellizzoni, A. de Luca, A. Słowikowska, and P. A. Caraveo. A Multiwavelength Study of the Pulsar PSR B1929+10 and Its X-Ray Trail. *ApJ*, 645:1421–1435, July 2006. doi: 10.1086/504458.

M. Beilicke. *Entdeckung einer unidentifizierten, ausgedehnten TeV-Quelle HESS J1303−631 und Bestätigung der Radiogalaxie M87 als TeV-Quelle mit den H.E.S.S.-Cherenkov-Teleskopen.* PhD thesis, Universität Hamburg, 2005. erschienen in der DISKI-Reihe mit der Nummer 216.

D. Berge, S. Funk, and J. Hinton. Background modelling in very-high-energy γ-ray astronomy. *A&A*, 466:1219–1229, May 2007. doi: 10.1051/0004-6361:20066674.

K. Bernlöhr. Simulation of imaging atmospheric Cherenkov telescopes with CORSIKA and sim_telarray. *Astroparticle Physics*, 30:149–158, October 2008. doi: 10.1016/j.astropartphys.2008.07.009.

K. Bernlöhr, O. Carrol, R. Cornils, S. Elfahem, P. Espigat, S. Gillessen, G. Heinzelmann, G. Hermann, W. Hofmann, D. Horns, I. Jung, R. Kankanyan, A. Katona, B. Khelifi, H. Krawczynski, M. Panter, M. Punch, S. Rayner, G. Rowell, M. Tluczykont, and R. van Staa. The optical system of the H.E.S.S. imaging atmospheric Cherenkov telescopes. Part I: layout and components of the system. *Astroparticle Physics*, 20: 111–128, November 2003. doi: 10.1016/S0927-6505(03)00171-3.

G. Bertone, D. Hooper, and J. Silk. Particle dark matter: evidence, candidates and constraints. *Phys. Rep.*, 405:279–390, January 2005. doi: 10.1016/j.physrep.2004.08.031.

M. F. Bietenholz and N. Bartel. The expansion and radio spectral index of G21.5-0.9: is PSR J1833-1034 the youngest pulsar? *MNRAS*, 386:1411–1416, May 2008. doi: 10.1111/j.1365-2966.2008.13058.x.

Emrah Birsin. Studies for a Dark Matter Search in the Galactic Halo with H.E.S.S. Master's thesis, Humboldt University at Berlin, Germany, 2011.

P. Blasi. Origin of the Positron Excess in Cosmic Rays. *Physical Review Letters*, 103 (5):051104–+, July 2009. doi: 10.1103/PhysRevLett.103.051104.

G. R. Blumenthal and R. J. Gould. Bremsstrahlung, Synchrotron Radiation, and Compton Scattering of High-Energy Electrons Traversing Dilute Gases. *Reviews of Modern Physics*, 42:237–271, 1970. doi: 10.1103/RevModPhys.42.237.

C. Borgmeier, N. Komin, M. de Naurois, S. Schlenker, U. Schwanke, C. Stegmann, and H.E.S.S. collaboration. The Central Data Acquisition System of the H.E.S.S. Telescope System. In *International Cosmic Ray Conference*, volume 5 of *International Cosmic Ray Conference*, pages 2891–+, July 2003.

J. Brand and L. Blitz. The Velocity Field of the Outer Galaxy. *A&A*, 275:67–+, August 1993.

M. Broy. *Object-oriented Programming and Software Development – A Critical Assessment*, chapter 4, pages 211–222. Springer, Rudower Chaussee, 1st edition, 2002. ISBN 3-540-21835-1. Hier stehen die Anmerkungen.

N. Bucciantini. Pulsar bow-shock nebulae. II. Hydrodynamical simulation. *A&A*, 387: 1066–1073, June 2002. doi: 10.1051/0004-6361:20020495.

F. Buschmann, R. Meunier, and H. Rohnert. *Pattern-Oriented Software Architecture: A System of Patterns.* John Wiley & Sons Ltd., 1996.

Y. M. Butt, J. A. Combi, J. Drake, J. P. Finley, A. Konopelko, M. Lister, J. Rodriguez, and D. Shepherd. TeV J2032+4130: a not-so-dark accelerator? *MNRAS*, 385:1764–1770, April 2008. doi: 10.1111/j.1365-2966.2008.12959.x.

S. Carrigan, J. A. Hinton, W. Hofmann, and et al. Establishing a connection between high-power pulsars and very-high-energy gamma-ray sources. In *International Cosmic Ray Conference*, volume 2 of *International Cosmic Ray Conference*, pages 659–662, 2008.

G. Cassam-Chenaï, J. P. Hughes, E. M. Reynoso, C. Badenes, and D. Moffett. Morphological Evidence for Azimuthal Variations of the Cosmic-Ray Ion Acceleration at the Blast Wave of SN 1006. *ApJ*, 680:1180–1197, June 2008. doi: 10.1086/588015.

CELESTE Collaboration. Gamma-ray astronomy above 30 GeV with the CELESTE experiment (1996-2004). In F. A. Aharonian, H. J. Völk, & D. Horns, editor, *High Energy Gamma-Ray Astronomy*, volume 745 of *American Institute of Physics Conference Series*, pages 645–650, February 2005. doi: 10.1063/1.1878477.

O. Celik. The Status of the Veritas Gamma-Ray Telescope Array. *APS Meeting Abstracts*, pages 11001–+, April 2007.

J. J. Condon, M. R. Griffith, and A. E. Wright. The Parkes-MIT-NRAO surveys. IV - Maps for the Southern Survey covering delta in the range -88 to -37 deg. *AJ*, 106: 1095–1100, September 1993. doi: 10.1086/116707.

J. M. Cordes and T. J. W. Lazio. NE2001.I. A New Model for the Galactic Distribution of Free Electrons and its Fluctuations. *ArXiv Astrophysics e-prints*, July 2002.

R. Cornils, S. Gillessen, I. Jung, W. Hofmann, M. Beilicke, K. Bernlöhr, O. Carrol, S. Elfahem, G. Heinzelmann, G. Hermann, D. Horns, R. Kankanyan, A. Katona, H. Krawczynski, M. Panter, S. Rayner, G. Rowell, M. Tluczykont, and R. van Staa. The optical system of the H.E.S.S. imaging atmospheric Cherenkov telescopes. Part II: mirror alignment and point spread function. *Astroparticle Physics*, 20:129–143, November 2003a. doi: 10.1016/S0927-6505(03)00172-5.

R. Cornils, S. Gillessen, I. Jung, W. Hofmann, G. Heinzelmann, and H.E.S.S. collaboration. Mirror Alignment and Performance of the Optical System of the H.E.S.S. Imaging Atmospheric Cherenkov Telescopes. In *International Cosmic Ray Conference*, volume 5 of *International Cosmic Ray Conference*, pages 2875–+, July 2003b.

Vlad Coroama and Felix Röthenbacher. The chatty environment. In *Demo at the Second Conference on Pervasive Computing and Communications (PerCom 2004)*, Orlando, Florida, March 2004.

F. V. Coroniti. Magnetically striped relativistic magnetohydrodynamic winds - The Crab Nebula revisited. *ApJ*, 349:538–545, February 1990. doi: 10.1086/168340.

F. Crawford and C. L. Tiffany. Flux Densities and Radio Polarization Characteristics of Two Vela-like Pulsars. *AJ*, 134:1231–1236, September 2007. doi: 10.1086/521020.

J. K. Daugherty and A. K. Harding. Gamma ray pulsars: Extended polar CAP cascades from nearly aligned rotators. *A&AS*, 120:C107+, November 1996.

A. Daum, G. Hermann, M. Hess, W. Hofmann, H. Lampeitl, G. Pühlhofer, F. Aharonian, A. G. Akhperjanian, J. A. Barrio, A. S. Beglarian, K. Bernlöhr, J. J. G. Beteta, S. M. Bradbury, J. L. Contreras, J. Cortina, T. Deckers, E. Feigl, J. Fernandez, V. Fonseca, A. Frass, B. Funk, J. C. Gonzalez, G. Heinzelmann, M. Hemberger, A. Heusler, I. Holl, D. Horns, R. Kankanyan, O. Kirstein, C. Köhler, A. Konopelko, D. Kranich, H. Krawczynski, H. Kornmayer, A. Lindner, E. Lorenz, N. Magnussen, H. Meyer, R. Mirzoyan, H. Möller, A. Moralejo, L. Padilla, M. Panter, D. Petry, R. Plaga, J. Prahl, C. Prosch, G. Rauterberg, W. Rhode, A. Röhring, V. Sahakian, M. Samorski, J. A. Sanchez, D. Schmele, W. Stamm, M. Ulrich, H. J. Völk, S. Westerhoff, B. Wiebel-Sooth, C. A. Wiedner, M. Willmer, and H. Wirth. First results on the performance of the HEGRA IACT array. *Astroparticle Physics*, 8:1–11, December 1997. doi: 10.1016/S0927-6505(97)00031-5.

O. C. de Jager, S. E. S. Ferreira, A. Djannati-Ataï, M. Dalton, C. Deil, K. Kosack, M. Renaud, U. Schwanke, and O. Tibolla. Unidentified Gamma-Ray Sources as Ancient Pulsar Wind Nebulae. *ArXiv e-prints*, June 2009.

J. M. Dickey and F. J. Lockman. H I in the Galaxy. *ARA&A*, 28:215–261, 1990. doi: 10.1146/annurev.aa.28.090190.001243.

J. Ellis, J. Hisano, M. Raidal, and Y. Shimizu. New parametrization of the seesaw mechanism and applications in supersymmetric models. *Phys. Rev. D*, 66(11):115013–+, December 2002. doi: 10.1103/PhysRevD.66.115013.

G. G. Fazio, H. F. Helmken, E. O'Mongain, and T. C. Weekes. Detection of High-Energy Gamma Rays from the Crab Nebula. *ApJ*, 175:L117+, August 1972. doi: 10.1086/180998.

K. M. Ferrière. The interstellar environment of our galaxy. *Reviews of Modern Physics*, 73:1031–1066, October 2001. doi: 10.1103/RevModPhys.73.1031.

Alois Ferscha and Friedemann Mattern, editors. *Pervasive Computing (Proceedings of PERVASIVE 2004, Second International Conference on Pervasive Computing)*, number 3001 in LNCS, Lienz/Vienna, Austria, April 2004. Springer-Verlag. ISBN 3-540-21835-1. Online version of the proceedings at www.springerlink.com.

S. Funk, G. Hermann, J. Hinton, D. Berge, K. Bernlöhr, W. Hofmann, P. Nayman, F. Toussenel, and P. Vincent. The trigger system of the H.E.S.S. telescope array. *Astroparticle Physics*, 22:285–296, November 2004. doi: 10.1016/j.astropartphys.2004.08.001.

B. M. Gaensler, E. van der Swaluw, F. Camilo, V. M. Kaspi, F. K. Baganoff, F. Yusef-Zadeh, and R. N. Manchester. The Mouse that Soared: High-Resolution X-Ray Imaging of the Pulsar-powered Bow Shock G359.23-0.82. *ApJ*, 616:383–402, November 2004a. doi: 10.1086/424906.

B. M. Gaensler, E. van der Swaluw, F. Camilo, V. M. Kaspi, F. K. Baganoff, F. Yusef-Zadeh, and R. N. Manchester. The Mouse that Soared: High-Resolution X-Ray Imaging of the Pulsar-powered Bow Shock G359.23-0.82. *ApJ*, 616:383–402, November 2004b. doi: 10.1086/424906.

B. M. Gaensler, S. Chatterjee, P. O. Slane, E. van der Swaluw, F. Camilo, and J. P. Hughes. The X-Ray Structure of the Pulsar Bow Shock G189.22+2.90 in the Supernova Remnant IC 443. *ApJ*, 648:1037–1042, September 2006. doi: 10.1086/506246.

T. K. Gaisser. *Cosmic Rays and Particle Physics.* Cambridge University Press, January 1991.

Y. A. Gallant and R. J. Tuffs. Infrared Observations of Plerions With ISO. In J. Paul, T. Montmerle, & E. Aubourg, editor, *19th Texas Symposium on Relativistic Astrophysics and Cosmology*, December 1998.

J. D. Gelfand, P. O. Slane, and W. Zhang. A Dynamical Model for the Evolution of a Pulsar Wind Nebula Inside a Nonradiative Supernova Remnant. *ApJ*, 703:2051–2067, October 2009. doi: 10.1088/0004-637X/703/2/2051.

Lars Gemeinhardt. Diplomarbeit – webis: Ein web-orientiertes informationssystem (webis). Nicht veröffentlicht, 2001.

P. Goldreich and W. H. Julian. Pulsar Electrodynamics. *ApJ*, 157:869–+, August 1969. doi: 10.1086/150119.

Martin Grabmüller. *Sizzle Embedding Manual.* HU Berlin, Rudower Chaussee, 0.0.30 edition, December 2000. This manual documents how to embed the Sizzle library into programs written in the C programming language. Programs which embed Sizzle can make use of Scheme as an extension language.

G.E. Hagerud, editor. *A new nonlinear GARCH model.* EFI, Stockholm School of Economics, 1997.

D. Heck, J. Knapp, J. N. Capdevielle, G. Schatz, and T. Thouw. *CORSIKA: a Monte Carlo code to simulate extensive air showers.* http://adsabs.harvard.edu/abs/1998cmcc.book.....H, February 1998.

W. Heitler. *Quantum theory of radiation.* Dover Publication, 1954.

Th. Hermes. *Texturen: Analyse, Beschreibung und Synthese.* PhD thesis, Universität Bremen, FB 3, 1999. erschienen in der DISKI-Reihe mit der Nummer 216.

HESS Collaboration, A. Abramowski, F. Acero, F. Aharonian, A. G. Akhperjanian, G. Anton, A. Barnacka, U. Barres de Almeida, A. R. Bazer-Bachi, Y. Becherini, J. Becker, B. Behera, K. Bernlöhr, A. Bochow, C. Boisson, J. Bolmont, P. Bordas, V. Borrel, J. Brucker, F. Brun, P. Brun, T. Bulik, I. Büsching, S. Carrigan, S. Casanova, M. Cerruti, P. M. Chadwick, A. Charbonnier, R. C. G. Chaves, A. Cheesebrough, L. -. Chounet, A. C. Clapson, G. Coignet, J. Conrad, M. Dalton, M. K. Daniel, I. D. Davids, B. Degrange, C. Deil, H. J. Dickinson, A. Djannati-Ataï, W. Domainko, L. O'C. Drury, F. Dubois, G. Dubus, J. Dyks, M. Dyrda, K. Egberts, P. Eger, P. Espigat, L. Fallon, C. Farnier, S. Fegan, F. Feinstein, M. V. Fernandes, A. Fiasson, A. Frster, G. Fontaine, M. Füßling, Y. A. Gallant, H. Gast, L. Gérard, D. Gerbig, B. Giebels, J. F. Glicenstein, B. Glück, P. Goret, D. Göring, J. D. Hague, D. Hampf, M. Hauser, S. Heinz, G. Heinzelmann, G. Henri, G. Hermann, J. A. Hinton, A. Hoffmann, W. Hofmann, P. Hofverberg, D. Horns, A. Jacholkowska, O. C. de Jager, C. Jahn, M. Jamrozy, I. Jung, M. A. Kastendieck, K. Katarzyński, U. Katz, S. Kaufmann, D. Keogh, M. Kerschhaggl, D. Khangulyan, B. Khélifi, D. Klochkov, W. Kluźniak, T. Kneiske, N. Komin, K. Kosack, R. Kossakowski, H. Laffon, G. Lamanna, D. Lennarz, T. Lohse, A. Lopatin, C. -. Lu, V. Marandon, A. Marcowith, J. Masbou, D. Maurin, N. Maxted, T. J. L. McComb, M. C. Medina, J. Méhault, R. Moderski, E. Moulin, C. L. Naumann, M. Naumann-Godo, M. de Naurois, D. Nedbal, D. Nekrassov, N. Nguyen, B. Nicholas, J. Niemiec, S. J. Nolan, S. Ohm, J. Olive, E. de Oña Wilhelmi, B. Opitz, M. Ostrowski, M. Panter, M. Paz Arribas, G. Pedaletti1, G. Pelletier, P. -. Petrucci, S. Pita, G. Pühlhofer, M. Punch, A. Quirrenbach, M. Raue, S. M. Rayner, A. Reimer, O. Reimer, M. Renaud, R. de los Reyes, F. Rieger, J. Ripken, L. Rob, S. Rosier-Lees, G. Rowell, B. Rudak, C. B. Rulten, J. Ruppel, F. Ryde, V. Sahakian, A. Santangelo, R. Schlickeiser, F. M. Schöck, A. Schönwald, U. Schwanke, S. Schwarzburg, S. Schwemmer, A. Shalchi, M. Sikora, J. L. Skilton, H. Sol, G. Spengler, Ł. Stawarz, R. Steenkamp, C. Stegmann, F. Stinzing, I. Sushch, A. Szostek, J. -. Tavernet, R. Terrier, O. Tibolla, M. Tluczykont, K. Valerius, C. van Eldik, G. Vasileiadis, C. Venter, J. P. Vialle, A. Viana, P. Vincent, M. Vivier, H. J. Völk, F. Volpe, S. Vorobiov, M. Vorster, S. J. Wagner, M. Ward, A. Wierzcholska, A. Zajczyk, A. A. Zdziarski, A. Zech, and H. -. Zechlin. H.E.S.S. constraints on Dark Matter annihilations towards the Sculptor and Carina Dwarf Galaxies. *ArXiv e-prints*, December 2010.

J. J. Hester. The Crab Nebula: An Astrophysical Chimera. *ARA&A*, 46:127–155, September 2008. doi: 10.1146/annurev.astro.45.051806.110608.

D. A. Hill. Photography of Čerenkov Light from Extensive Air Showers in the Atmosphere. *Nature*, 191:690–+, August 1961. doi: 10.1038/191690a0.

A. M. Hillas. Cerenkov light images of EAS produced by primary gamma. In F. C. Jones, editor, *International Cosmic Ray Conference*, volume 3 of *International Cosmic Ray Conference*, pages 445–448, August 1985.

J. A. Hinton. The status of the HESS project. *New A Rev.*, 48:331–337, April 2004. doi: 10.1016/j.newar.2003.12.004.

G. Hobbs, A. Faulkner, I. H. Stairs, F. Camilo, R. N. Manchester, A. G. Lyne, M. Kramer, N. D'Amico, V. M. Kaspi, A. Possenti, M. A. McLaughlin, D. R. Lorimer, M. Burgay, B. C. Joshi, and F. Crawford. The Parkes multibeam pulsar survey - IV. Discovery of 180 pulsars and parameters for 281 previously known pulsars. *MNRAS*, 352:1439–1472, August 2004. doi: 10.1111/j.1365-2966.2004.08042.x.

W. Hofmann, I. Jung, A. Konopelko, H. Krawczynski, H. Lampeitl, and G. Pühlhofer. Comparison of techniques to reconstruct VHE gamma-ray showers from multiple stereoscopic Cherenkov images. *Astroparticle Physics*, 12:135–143, November 1999. doi: 10.1016/S0927-6505(99)00084-5.

R. V. Hogg and A. T. Craig. *Introduction to Mathematical Statistics.* Macmillan, New York, 4 edition, 1978.

D. Horns and F. A. Aharonian. The Crab Nebula: Linking MeV Synchrotron and 50 TeV Inverse Compton Photons. In V. Schoenfelder, G. Lichti, & C. Winkler, editor, *5th INTEGRAL Workshop on the INTEGRAL Universe*, volume 552 of *ESA Special Publication*, pages 439–+, October 2004.

A. Horvath. `http://commons.wikimedia.org/w/thumb.php?f=Cherenkov.svg&width=2000px`, 2006.

E. B. Jenkins. Evidence and Implications of Pressure Fluctuations in the ISM. *Ap&SS*, 289:215–223, February 2004. doi: 10.1023/B:ASTR.0000014946.85573.4a.

Fichter Josef. Harmonisierung in den versch. bereichen des patentwesens. In Rafeiner Otmar, editor, *Patente und Schutzrechte*, chapter 4, pages 18–26. Manz Wien, Rudower Chaussee, 2. edition, 1993. Hier stehen die Anmerkungen.

C. F. Kennel and F. V. Coroniti. Magnetohydrodynamic model of Crab nebula radiation. *ApJ*, 283:710–730, August 1984. doi: 10.1086/162357.

T. Klähn, D. Blaschke, F. Sandin, C. Fuchs, A. Faessler, H. Grigorian, G. Röpke, and J. Trümper. Modern compact star observations and the quark matter equation of state. *Physics Letters B*, 654:170–176, October 2007. doi: 10.1016/j.physletb.2007.08.048.

L. T. Ksenofontov, E. G. Berezhko, and H. J. Völk. Dependence of the gamma-ray emission from SN 1006 on the astronomical parameters. *A&A*, 443:973–980, December 2005. doi: 10.1051/0004-6361:20053056.

L. Landau. *Electrodynamics of Continuous Media.* Pergamon, Amsterdam, 1984. ISBN 0080302750.

Kurt Lautenbach. Logical Reasoning and Petri Nets. Fachberichte Informatik 12–2002, Universität Koblenz-Landau, Universität Koblenz-Landau, Institut für Informatik, Rheinau 1, D-56075 Koblenz, 2002. URL `http://www.uni-koblenz.de/fb4/publikationen/gelbereihe/RR-12-2002.pdf`. The main result of the paper states that a set F of propositional-logic formulas is contradictory iff in all net representations of F the empty marking is reproducible.

T.-P. Li and Y.-Q. Ma. Analysis methods for results in gamma-ray astronomy. *ApJ*, 272:317–324, September 1983. doi: 10.1086/161295.

M. A. Livingstone, V. M. Kaspi, F. P. Gavriil, R. N. Manchester, E. V. G. Gotthelf, and L. Kuiper. New phase-coherent measurements of pulsar braking indices. *Ap&SS*, 308: 317–323, April 2007. doi: 10.1007/s10509-007-9320-3.

H. Lütkepohl and M. Krätzig, editors. *Applied Time Series Econometrics.* Cambridge University Press, Cambridge, 2004.

A. G. Lyne and D. R. Lorimer. High birth velocities of radio pulsars. *Nature*, 369: 127–129, May 1994. doi: 10.1038/369127a0.

R. N. Manchester, G. B. Hobbs, A. Teoh, and M. Hobbs. ATNF Pulsar Catalog (Manchester+, 2005). *VizieR Online Data Catalog*, 7245:0–+, August 2005.

F. Mattana, M. Falanga, D. Götz, R. Terrier, P. Esposito, A. Pellizzoni, A. De Luca, V. Marandon, A. Goldwurm, and P. A. Caraveo. The Evolution of the γ- and X-Ray Luminosities of Pulsar Wind Nebulae. *ApJ*, 694:12–17, March 2009. doi: 10.1088/0004-637X/694/1/12.

P. Meade, M. Papucci, A. Strumia, and T. Volansky. Dark Matter interpretations of the $e^{\pm}$ excesses after FERMI. *Nuclear Physics B*, 831:178–203, May 2010. doi: 10.1016/j.nuclphysb.2010.01.012.

M. Meyer, D. Horns, and H.-S. Zechlin. The Crab Nebula as a standard candle in very high-energy astrophysics. *A&A*, 523:A2+, November 2010. doi: 10.1051/0004-6361/201014108.

R. Mukherjee and J. P. Halpern. Chandra Observation of the Unidentified TeV Gamma-Ray Source HESS J1303-631 in the Galactic Plane. *ApJ*, 629:1017–1020, August 2005. doi: 10.1086/431581.

S. Ohm, C. van Eldik, and K. Egberts. γ/hadron separation in very-high-energy γ-ray astronomy using a multivariate analysis method. *Astroparticle Physics*, 31:383–391, June 2009. doi: 10.1016/j.astropartphys.2009.04.001.

Otto 2004. Grundsätze, 2004. URL `http://www.otto.com/umwelt/umwelt_grundindex.html`. Einstiegsseite zum Unternehmensleitbild.

S. Park, M. P. Muno, F. K. Baganoff, Y. Maeda, M. Morris, G. Chartas, D. Sanwal, D. N. Burrows, and G. P. Garmire. A Candidate Neutron Star Associated with Galactic Center Supernova Remnant Sagittarius A East. *ApJ*, 631:964–975, October 2005. doi: 10.1086/432639.

S. Profumo and P. Ullio. The role of antimatter searches in the hunt for supersymmetric dark matter. *J. Cosmology Astropart. Phys.*, 7:6–+, July 2004. doi: 10.1088/1475-7516/2004/07/006.

G. Puehlhofer and HEGRA Collaboration. Scans of the TeV Gamma-Ray Sky with the HEGRA System of Cherenkov Telescopes. In *International Cosmic Ray Conference*, volume 4 of *International Cosmic Ray Conference*, pages 2319–+, July 2003.

M. J. Rees and J. E. Gunn. The origin of the magnetic field and relativistic particles in the Crab Nebula. *MNRAS*, 167:1–12, April 1974.

M. Renaud, S. Hoppe, N. Komin, E. Moulin, V. Marandon, and A.-C. Clapson. Pulsar Wind Nebula candidates recently discovered by H.E.S.S. In F. A. Aharonian, W. Hofmann, & F. Rieger, editor, *American Institute of Physics Conference Series*, volume 1085 of *American Institute of Physics Conference Series*, pages 285–288, December 2008. doi: 10.1063/1.3076661.

S. P. Reynolds. Synchrotron Models for X-Rays from the Supernova Remnant SN 1006. *ApJ*, 459:L13+, March 1996. doi: 10.1086/309936.

J. Ripken, M. Beilicke, G. Heinzelmann, and et al. Is the unidentified TeV γ-ray source HESS J1303-631 a dark matter clump? In *International Cosmic Ray Conference*, volume 2 of *International Cosmic Ray Conference*, pages 795–798, 2008.

Philip Robinson, Harald Vogt, and Waleed Wagealla, editors. *Privacy, Security and Trust within the Context of Pervasive Computing.* The Kluwer International Series in Engineering and Computer Science. Springer Science+Business Media, Inc., 2005. ISBN 0-387-23461-6. URL `http://www.springeronline.com/sgw/cda/frontpage/0,11855,4-186-72-35393%865-0,00.html`.

R. W. Romani. Gamma-Ray Pulsars: Radiation Processes in the Outer Magnetosphere. *ApJ*, 470:469–+, October 1996. doi: 10.1086/177878.

Kay Römer. Programming paradigms and middleware for sensor networks. *GI/ITG Fachgespräch Sensornetze, Karlsruhe*, Jahrgang 3(3):33–35, Feb 2004.

Kay Römer and Friedemann Mattern. Scientific report on the esf exploratory workshop on wireless sensor networks. http://www.vs.inf.ethz.ch/publ/papers/esfreport.pdf, Jun 2004.

M. A. Ruderman and P. G. Sutherland. Theory of pulsars - Polar caps, sparks, and coherent microwave radiation. *ApJ*, 196:51–72, February 1975. doi: 10.1086/153393.

G. B. Rybicki and A. P. Lightman. *Radiative processes in astrophysics.* "Wiley-VCH", 1979.

Z. Salah, D. Bartz, F. Dammann, E. Schwaderer, M. Maassen, and W. Straßer. A Fast and Accurate Approach for the Segmentation of the Paranasal Sinus. In *Proc. of Workshop Bildverarbeitung in der Medizin*, Informatik Aktuell, page 3000, Rudower Chaussee, 2005. herausgebende Organisation. ISBN 3-540-21835-1.

F. Schmidt. Corsika shower images. `http://www.ast.leeds.ac.uk/~fs/showerimages.html`, Jun 2005.

G. Servant and T. M. P. Tait. Is the lightest Kaluza-Klein particle a viable dark matter candidate? *Nuclear Physics B*, 650:391–419, February 2003. doi: 10.1016/S0550-3213(02)01012-X.

S. L. Snowden, M. R. Collier, and K. D. Kuntz. XMM-Newton Observation of Solar Wind Charge Exchange Emission. *ApJ*, 610:1182–1190, August 2004. doi: 10.1086/421841.

F. W. Stecker, O. C. de Jager, and M. H. Salamon. TeV gamma rays from 3C 279 - A possible probe of origin and intergalactic infrared radiation fields. *ApJ*, 390:L49–L52, May 1992. doi: 10.1086/186369.

F. R. Stephenson and D. A. Green. Historical supernovae and their remnants. *Historical supernovae and their remnants, by F. Richard Stephenson and David A. Green. International series in astronomy and astrophysics, vol. 5. Oxford: Clarendon Press, 2002, ISBN 0198507666*, 5, 2002.

J. H. Taylor and J. M. Cordes. Pulsar distances and the galactic distribution of free electrons. *ApJ*, 411:674–684, July 1993. doi: 10.1086/172870.

The H. E. S. S Collaboration: S. Funk, J. A. Hinton, and O. C. deJager. Energy Dependent Morphology in the PWN candidate HESS J1825-137. *ArXiv e-prints*, September 2007.

O. Tibolla, R. C. G. Chaves, W. Domainko, O. de Jager, S. Kaufmann, S. Wagner, N. Komin, K. Kosack, A. Fiasson, M. Renaud, and for the H. E. S. S. Collaboration. New unidentified Galactic H.E.S.S. sources. *ArXiv e-prints*, December 2009.

C. M. Urry and P. Padovani. Unified Schemes for Radio-Loud Active Galactic Nuclei. *PASP*, 107:803–+, September 1995. doi: 10.1086/133630.

E. van der Swaluw. Interaction of a magnetized pulsar wind with its surroundings. MHD simulations of pulsar wind nebulae. *A&A*, 404:939–947, June 2003. doi: 10.1051/0004-6361:20030452.

E. van der Swaluw, A. Achterberg, Y. A. Gallant, and G. Tóth. Pulsar wind nebulae in supernova remnants. Spherically symmetric hydrodynamical simulations. *A&A*, 380:309–317, December 2001. doi: 10.1051/0004-6361:20011437.

E. van der Swaluw, A. Achterberg, Y. A. Gallant, T. P. Downes, and R. Keppens. Interaction of high-velocity pulsars with supernova remnant shells. *A&A*, 397:913–920, January 2003. doi: 10.1051/0004-6361:20021488.

P. Vincent, J.-P. Denanca, J.-F. Huppert, P. Manigot, M. de Naurois, P. Nayman, J.-P. Tavernet, F. Toussenel, L.-M. Chounet, B. Degrange, P. Espigat, G. Fontaine, J. Guy, G. Hermann, A. Kohnle, C. Masterson, M. Punch, M. Rivoal, L. Rolland, T. Saitoh, and H.E.S.S. collaboration. Performance of the H.E.S.S. Cameras. In *International Cosmic Ray Conference*, volume 5 of *International Cosmic Ray Conference*, pages 2887–+, July 2003.

S. J. Wagner, W. Benbow, D. Emmanoulopoulos, and et al. Constraints on Quantum Gravity from Fast TeV Gamma-Ray Flares of AGN. In *International Cosmic Ray Conference*, volume 4 of *International Cosmic Ray Conference*, pages 749–752, 2008.

M. G. Watson, A. C. Schröder, D. Fyfe, C. G. Page, G. Lamer, S. Mateos, J. Pye, M. Sakano, S. Rosen, J. Ballet, X. Barcons, D. Barret, T. Boller, H. Brunner, M. Brusa, A. Caccianiga, F. J. Carrera, M. Ceballos, R. Della Ceca, M. Denby, G. Denkinson, S. Dupuy, S. Farrell, F. Fraschetti, M. J. Freyberg, P. Guillout, V. Hambaryan, T. Maccacaro, B. Mathiesen, R. McMahon, L. Michel, C. Motch, J. P. Osborne, M. Page, M. W. Pakull, W. Pietsch, R. Saxton, A. Schwope, P. Severgnini, M. Simpson, G. Sironi, G. Stewart, I. M. Stewart, A.-M. Stobbart, J. Tedds, R. Warwick, N. Webb, R. West, D. Worrall, and W. Yuan. The XMM-Newton serendipitous survey. V. The Second XMM-Newton serendipitous source catalogue. *A&A*, 493:339–373, January 2009. doi: 10.1051/0004-6361:200810534.

T. C. Weekes, M. F. Cawley, D. J. Fegan, K. G. Gibbs, A. M. Hillas, P. W. Kowk, R. C. Lamb, D. A. Lewis, D. Macomb, N. A. Porter, P. T. Reynolds, and G. Vacanti. Observation of TeV gamma rays from the Crab nebula using the atmospheric Cerenkov imaging technique. *ApJ*, 342:379–395, July 1989. doi: 10.1086/167599.

Stephan Weibelzahl. Conception, implementation, and evaluation of a case based learnin system for sales support in the internet. Master's thesis, Universität Trier, 1999.

C. A. Wilson-Hodge, M. L. Cherry, W. H. Baumgartner, E. Beklen, P. Narayana Bhat, M. S. Briggs, A. Camero-Arranz, G. L. Case, V. Chaplin, V. Connaughton, M. H. Finger, N. Gehrels, J. Greiner, K. Jahoda, P. Jenke, R. M. Kippen, C. Kouveliotou, H. A. Krimm, E. Kuulkers, C. A. Meegan, L. Natalucci, W. S. Paciesas, R. Preece, J. C. Rodi, N. Shaposhnikov, G. K. Skinner, D. Swartz, and A. von Kienlin. When A Standard Candle Flickers. *ArXiv e-prints*, October 2010.

H. Yüksel, M. D. Kistler, and T. Stanev. TeV Gamma Rays from Geminga and the Origin of the GeV Positron Excess. *Physical Review Letters*, 103(5):051101–+, July 2009. doi: 10.1103/PhysRevLett.103.051101.

B. R. Zeiger, W. F. Brisken, S. Chatterjee, and W. M. Goss. Proper Motions of PSRs B1757-24 and B1951+32: Implications for Ages and Associations. *ApJ*, 674:271–277, February 2008. doi: 10.1086/525276.

List of Figures

List of Tables

Selbständigkeitserklärung

Ich erkläre, dass ich die vorliegende Arbeit selbständig und nur unter Verwendung der angegebenen Literatur und Hilfsmittel angefertigt habe.

Berlin, den 14. Februar, Matthew Lynn Dalton